Towards a Next-Generation Preclinical PET/MR Insert with Improved Timing and Count Rate Performance

by
Devin Van Elburg

A thesis submitted to the Faculty of Graduate Studies of
The University of Manitoba
in partial fulfilment of the requirements of the degree of

MASTER OF SCIENCE

Department of Physics and Astronomy
University of Manitoba
Winnipeg, Manitoba, Canada

Abstract

Our group has previously developed a PET insert for simultaneous PET/MRI imaging. The insert consists of silicon photomultipliers (SiPMs) with a resistor-based charge division multiplexing readout circuit. Some limitations include a 2.5 ns coincidence time resolution (CTR), a relatively long signal duration of $>$1.5 μs, and a 1.3 μs paralyzable dead time. This thesis focuses on characterizing these limitations and demonstrating a second-generation detector module for improved timing and count rate performance. First, optical coupling optimization using acrylic polymer tapes versus conventional silicone optical grease was investigated. Second, CTR and signal duration was reduced by using an enhanced readout board equipped with three new SiPM-type detectors. Last, dead time of the system was reduced by minimizing the sampling number of the OpenPET acquisition system. Future work includes design modification to accommodate the first-generation scintillator footprint and potentially to adapt the OpenPET acquisition system to read in SiPM 'fast' outputs.

Acknowledgements

There are many who have given me tremendous support through the work of this thesis, and to them I owe my most sincere gratitude. To my supervisor Dr. Andrew Goertzen, your wisdom and mentorship has been invaluable. You are an incredibly talented, kind person and it has been an absolute pleasure to work with you. To my past supervisors Dr. Alla Reznik and Dr. Peter McGhee, thank you for guidance and teaching, and for being my inspiration to pursue Medical Physics. To Research Manitoba (Research Manitoba Graduate Studentship award) and the Government of Manitoba (Manitoba Graduate Scholarship), I appreciate your financial support. To fellow graduate students in the PET research lab and in the Medical Physics, I consider myself lucky to have worked with such fine, brilliant people. I wish you all success. To Judy Patterson, I thoroughly enjoyed having you as a desk buddy over the last two years. I will miss your bright conversations and your kind heart. To Dr. Scott Noble and Simone Hagey, thank you for your help with the spectrophotometer measurements which contributed to my first scientific publication. To my family and friends here in Winnipeg (I see you Scotia boys) and back home in Thunder Bay, I'm truly blessed to have such incredible people in my life. To my parents Tammy and Gerald, and to my brother and sister Joe and Kathleen, I can't thank you enough for the unconditional love and support you have given me. I only hope you know how much you all mean to me. And finally to my Sovereign God, the Creator, the Great Scientist, You are deserving of all praise and thanksgiving. I follow Your leading, now and forever.

Contents

List of Figures

List of Tables

List of Acronyms

A100	Adhesive 100 (tape)
ADC	analog-to-digital converter
CLUT	crystal look-up table
CTR	coincidence time resolution
DB	detector board
DLO	dual-layer offset
DI	detector interface (board)
DOI	depth of interaction
ELUT	energy look-up table
ESR	Enhanced Specular Reflector
[^{18}F]-FDG	2-deoxy-2-[^{18}F]-fluoro-D-glucose, or '^{18}F-labelled fluorodeoxyglucose'
FOV	field of view
FPGA	field-programmable gate array
FWHM	full-width at half-maximum
GPA	General Purpose Acrylic (tape)
GS/s	giga-samples per second
I/O	input/output
kcps	kilo-counts per second
LED	leading edge discriminator
LOR	line of response
LYSO:Ce	cerium-doped lutetium-yttrium oxyorthosilicate
MPPC	multi-pixel photon counter

MRI	magnetic resonance imaging
NIM	Nuclear Instrumentation Module
PCB	printed circuit board
PDE	photon detection efficiency
PET	positron emission tomography
PS	Phillips Scientific
PMT	photomultiplier tube
s/e	samples per event
SB	support board
SiG	silicone optical grease
SiPM	silicon photomultiplier
TAC	time-to-amplitude converter
TDC	time-to-digital converter
TOF	time of flight
TTL	transistor-transistor logic

List of Copyright Materials

1. Chapter 4 of this thesis is reproduced (with minor modifications) from a manuscript published in *Physics in Medicine and Biology* © Institute of Physics and Engineering in Medicine. Reproduced with permission. All rights reserved. Source:

   D. J. Van Elburg, S. D. Noble, S. Hagey, and A. L. Goertzen. Comparison of acrylic polymer adhesive tapes and silicone optical grease in light sharing detectors for positron emission tomography. *Physics in Medicine and Biology*, 63(5):05NT02, 2018. doi.org/10.1088/1361-6560/aaa815.

2. Figures 2.6.2 is reprinted with permission © 2017 IEEE. Source:

   A. L. Goertzen, G. Stortz, J. D. Thiessen, D. Bishop, M. S. Khan, P. Kozlowski, F. Retiere, G. Schellenberg, E. Shams, V. Sossi, and C. J. Thompson. First Results From a High-Resolution Small Animal SiPM PET Insert for PET/MR Imaging at 7T. *IEEE Transactions on Nuclear Science*, 63(5):2424-2433, 2016.

3. Figure 3.2.5 is reprinted with permission © 2017 IEEE. Source:

   A. L. Goertzen, R. Shrestha, M. S. Khan, G. Stortz, D. Bishop, P. Kozlowski, F. Retiere, J. D. Thiessen, C. J. Thompson, and V. Sossi. Data Acquisition for a Preclinical MR Compatible PET Insert Using the OpenPET Platform. *IEEE Transactions on Radiation and*

Plasma Medical Sciences, 1(6):495-504, 2017.

Chapter 1

Introduction

Positron emission tomography (PET) is a powerful functional imaging technique that images the distribution of radiolabeled tracers. Tracer molecules are labelled with positron emitting (proton rich) nuclei, injected into the patient, and distributed throughout the body. PET scans reveal the tracer distribution which is related to tissue function. For example, 2-deoxy-2-[^{18}F]-fluoro-D-glucose ([^{18}F]-FDG) is commonly used clinically for cancer staging and post-treatment follow-up due to rapid glucose uptake in malignant tissues.

Typical PET detectors consist of a scintillating material coupled to a photodetector. Traditionally, the photodetectors used in PET detectors are photomultiplier tubes (PMTs). PMT-based whole body PET detectors with hybrid computed tomography (CT) scanners are widely used in medical clinics for staging tumours and monitoring therapy response [1]. More recently, PMTs are being replaced by solid state silicon photomultipliers (SiPMs), in part because SiPM technology is rapidly improving, with innovative designs driving performance enhancements [2, 3] (for example, [4, 5, 6, 7]). Perhaps the most intriguing characteristic of SiPMs over PMTs is they are compatible with magnetic resonance imaging (MRI). Hybrid PET/MRI detectors are of increasing interest because they can simultaneously combine anatomical imaging capability of MR, with its high soft-tissue contrast and no radiation

dose, together with the functional imaging capabilities of PET in order to produce enhanced fused functional and anatomical images.

SiPMs are useful for PET detectors with compact designs, particularly preclinical PET/MRI inserts. Fully integrated PET/MRI systems are more expensive than PET/CT systems due to the higher cost of MRI versus CT technology, the recent surge of research and development of PET/MRI, and the limited availability of PET/MRI compared to PET/CT [8]. The cost of a hybrid PET/MRI detector is drastically reduced when a PET detector is designed to fit inside an existing MRI bore. Several groups have recently designed PET/MRI inserts (for example, [9, 10, 11, 12]).

Our group has previously developed a prototype preclinical PET insert system for PET/MR imaging [12, 13, 14] that utilizes a detector design with an array of SiPMs read out with a resistor-based charge division multiplexing circuit and an array of dual-layer offset (DLO) scintillator crystals. This novel design possesses some limitations that have yet to be thoroughly characterized, including: a timing resolution of $\sim$2.0-2.5 ns, a signal duration of $>$ 1.5 μs, and a paralyzable dead time of 1.3 μs.

In Chapter 2, the basic physics of PET are discussed. In Chapter 3, the general methods for this work are explained, including the readout and acquisition hardware as well as data processing in software. Chapters 4-6 detail the work done in this thesis: optical coupling optimization with double-sided acrylic polymer tapes, single-pixel detector characterization, and detector module characterization with enhanced timing and count rate performance. Each of these chapters contains its' own materials, methods, results, and discussion sections focusing on how the performance of the first-generation PET insert can be improved.

Chapter 2

Background

2.1 Radioactive Decay

Radionuclides are unstable nuclei that decay (i.e. emit particles) in order to assume a stable configuration. Energy is released in the process, either as electromagnetic radiation (γ-rays) or as kinetic energy to the emitted particles. Natural radionuclides exist (for example, K, Ra), however radionuclides used in nuclear medicine are produced in cyclotrons or nuclear reactors. There are several modes of radioactive decay, including: beta (β^-) emission, positron (β^+) emission, alpha-particle (α) emission, electron capture, and internal conversion.

2.1.1 β^- Decay

Neutron-rich nuclei may assume a more stable configuration by converting a neutron into a proton, emitting an electron (β^-) in the process. An example of a β^- emitter is ^{137}Cs decay to ^{137}Ba:

$$^{137}_{55}\mathrm{Cs} \longrightarrow {}^{137}_{56}\mathrm{Ba} + {}^{0}_{-1}\beta + \bar{\nu} \tag{2.1}$$

β^- decay is always accompanied with an antineutrino ($\bar{\nu}$), which is a particle with negligible mass and no electrical charge. The difference in energy between ^{137}Cs and ^{137}Ba is imparted to the β^- particle and the antineutrino. Radionuclei often decay to a metastable configuration that will undergo a subsequent emission of a γ-ray. In the case of ^{137}Cs:

$$^{137}_{55}\mathrm{Cs} \longrightarrow {}^{137m}_{56}\mathrm{Ba} + {}^{0}_{-1}\beta + \bar{\nu} \tag{2.2}$$

$$^{137m}_{56}\mathrm{Ba} \longrightarrow {}^{137}_{56}\mathrm{Ba} + {}^{0}_{0}\gamma \tag{2.3}$$

The superscript ^{m} denotes a metastable nucleus. A significant portion of excess energy is given to the daugter $^{137\mathrm{m}}$Ba, giving it a metastable configuration. In a subsequent process, the $^{137\mathrm{m}}$Ba sheds the excess energy in the form of a 662 keV γ-ray.

2.1.2 Internal conversion

A competing process to γ-ray emission is internal conversion. The metastable nucleus emits a γ-ray that is absorbed by an orbital electron which is ejected from the atom. Internal conversion is most probable to occur in the K-shell, less likely for L-shell, and so on. For example, 89.9% of $^{137\mathrm{m}}$Ba $\longrightarrow$ ^{137}Ba decay results in emission of a 662 keV γ-ray, 8.2% results in internal conversion of a K-shell electron, and the remaining 1.9% results in conversion of lower energy orbital electrons [15]. Inner shell vacancies are filled by outer shell electrons, which emit characteristic x-rays equal to the difference in binding energies.

2.1.3 Electron capture

Proton-rich nuclei may undergo electron capture, a process which decreases the atomic number (Z) by one. In this process, an orbital electron (usually K-shell) is absorbed by the nucleus. Hence, a proton is effectively converted into a neutron. Inner shell vacancies

are filled by outer shell electrons accompanied by the emission of a characteristic x-ray. An example of a radionuclide that undergoes electron capture is ^{22}Na, which captures an orbital electron to become ^{22m}Ne:

$$^{22}_{11}\mathrm{Na} + {}^{0}_{-1}\beta \longrightarrow {}^{22m}_{10}\mathrm{Ne} + \nu \tag{2.4}$$

The daughter ^{22m}Ne $\longrightarrow$ ^{22}Ne decay will emit a 1.275 MeV γ-ray. However, a more probable mode of ^{22}Na decay is positron emission.

2.1.4 β^+ Decay

In contrast to β^+ decay, proton-rich nuclei may convert a proton into a neutron in order to assume a more stable configuration by emitting a positron (β^+). Positrons have the same mass but opposite charge (equal in magnitude, opposite polarity) of electrons. An example of β^+ emittion is ^{22}Na decay to ^{22}Ne:

$$^{22}_{11}\mathrm{Na} \longrightarrow {}^{22m}_{10}\mathrm{Ne} + {}^{0}_{+1}\beta + \nu \tag{2.5}$$

$$^{22m}_{10}\mathrm{Ne} \longrightarrow {}^{22}_{10}\mathrm{Ne} + {}^{0}_{0}\gamma \tag{2.6}$$

A 1.275 MeV γ-ray is emitted following the disintegration of metastable ^{22m}Ne. Decay of ^{22}Na results in 90.3% β^+ decay and 9.6% electron capture.

In PET, all radioactive tracers used must contain a positron emitter. PET relies on detecting anti-parallel photons emitted in a process called positron annihilation, which occurs after a positron is ejected from the tracer.

2.2 Positron Annihilation

Emitted positrons have a non-zero kinetic energy and will travel through the medium, losing kinetic energy through Coulomb interactions with other atoms in the medium. Once the positron's kinetic energy is sufficiently low, it will interact with an electron in the medium and momentarily combine to form a positronium. Positroniums are unstable "atoms" that consist of an electron and positron orbiting their centre of mass. The typical lifetime of a positronium is about 10^{-10}s. The positron and electron will combine and annihilate, converting their combined mass energy into two *annihilation photons*:

$$ {}^{0}_{+1}\beta + {}^{0}_{-1}\mathrm{e} \longrightarrow 2\,{}^{0}_{0}\gamma \tag{2.7} $$

By the conservation of energy, the total energy of the annihilation photons is equal to the rest mass of the positron and electron ($2m_e = 1.022$ MeV) plus any remaining kinetic energy at the point of annihilation. In general, annihilation photon pairs are two 511 keV γ-rays that propagate anti-parallel to each other.

2.2.1 Positron range

Immediately following positron decay, the ejected positron has too high a kinetic energy to stay in close proximity with an electron long enough to annihilate. Instead, the positron will follow an erratic path of Coulomb interactions that carry it away from the original site of decay until it eventually annihilates. The shortest distance from the parent radionuclide to an annihilation photon is the effective positron range. Positron range depends on the kinetic energy of the emitted positron. Table 2.2.1 lists positron kinetic energy and the corresponding positron range in water for several positron emitters.

Table 2.2.1: Positron modal kinetic energy at decay and root mean square (rms) positron range in water of various radionuclides used in PET [16].

Radionuclide	Kinetic energy (keV)	Positron rms range (mm)
^{22}Na	216	<0.6
^{18}F	250	0.6
^{11}C	386	1.1
^{13}N	492	1.5
^{15}O	735	2.5
^{68}Ga	836	2.9

2.2.2 Acollinearity

Annihilation photon travel perfectly anti-parallel only if the positronium momentum is zero at annihilation. The positron may have non-zero kinetic energy at the point of annihilation, and therefore there may be net momentum of the positronium. To conserve momentum, annihilation photons propogate at an angle $\theta = 180^\circ \pm 0.25^\circ$, where 0.25° is the mean acollinearity angle [17]. This phenomenon is referred to as *acollinearity*.

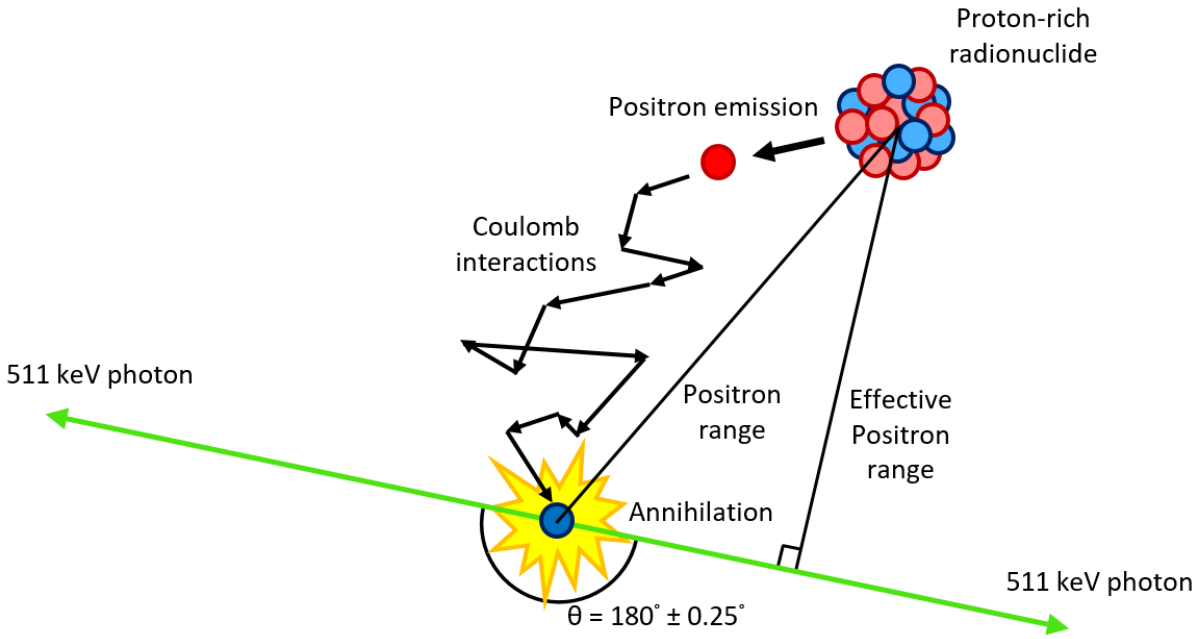

Figure 2.2.1: Diagram of positron emission to positrion annihilation.

Table 2.3.1: Dominating photon interaction in high and low Z materials for various photon energies.

	Photon energy range (MeV)				
	0.01 - 0.1	0.1 - 1.0	1.0 - 5.0	5 - 20	20 - 50
High Z	Photoelectric	Photoelectric	Compton	Pair Production	Pair Production
Low Z	Photoelectric	Compton	Compton	Compton	Pair Production

2.3 Photon Interactions

The probability of photon interaction within a medium can be quantified by the total mass attenuation coefficient μ/ρ. For a beam of N_o photons incident on a material with density ρ and thickness L, the number of photons N that transmit through the material without interacting is:

$$N = N_o \left(1 - e^{-\left(\frac{\mu}{\rho}\right)\rho L}\right) \tag{2.8}$$

The difference $N_o - N$ gives the number of photons that were attenuated in the medium. There are several types of photon interactions including the photoelectric effect, Compton scattering, and pair production. The probability of each interaction type varies with photon energy $h\nu$ and atomic number Z of the absorbing medium. Note this ν is photon frequency, not a neutrino as in Section 2.1. Table 2.3.1 is an approximation of which photon interaction dominates for 10 keV - 50 MeV photons in high and low Z materials (approximated from [15]).

2.3.1 Photoelectric effect

The *photoelectric effect* is the phenomenon in which a photon is absorbed by an orbital electron which is ejected from the atom (called a photoelectron). Photoelectrons, most probably ejected from the K-shell or L-shell orbitals, are released with a kinetic energy $E_{photoelectron}$:

$$E_{photoelectron} = h\nu - E_B \tag{2.9}$$

where $h\nu$ is the energy of the incident photon and E_B is the binding energy of the absorbing electron. Note the photoelectric effect cannot occur unless the energy of the incident photon exceeds the binding energy of the orbital electron (i.e. $h\nu > E_B$). The vacancy left by the ejected photoelectron is filled by an outer shell electron accompanied by emission of a characteristic x-ray equal to the difference in binding energies. The mass attenuation coefficient for photoelectric interaction τ/ρ has the following proportionality:

$$\frac{\tau}{\rho} \; \alpha \; \left(\frac{Z}{h\nu}\right)^3 \tag{2.10}$$

where $h\nu$ is the energy of the incident photon and Z is the atomic number of the absorbing material. The photoelectric effect is dominant for low $h\nu$ photons interacting with high Z media.

2.3.2 Compton (incoherent) scattering

Photons traversing a medium may be scattered by an orbital electron instead of absorbed. This photon interaction is called *Compton scattering* or *incoherent scattering*. The scattered photon has a trajectory at angle θ with respect to the incident photon trajectory, and has an energy E_S necessarily less than the initial energy $h\nu$:

$$E_S = h\nu \frac{1}{1 + \frac{h\nu}{m_e c^2}\,(1 - cos\theta)} \tag{2.11}$$

where $m_e c^2$ is the rest mass of an electron. The remaining energy is transferred to the orbital electron (called a recoil electron) which is ejected with a kinetic energy E_{recoil}:

$$\begin{aligned} E_{recoil} &= h\nu - E_S \\ &= h\nu \frac{\frac{h\nu}{m_e c^2}\,(1 - cos\theta)}{1 + \frac{h\nu}{m_e c^2}\,(1 - cos\theta)} \end{aligned} \tag{2.12}$$

Characteristic x-ray emission occurs when the inner shell vacancy left by the recoil electron is filled. In both Eq. 2.11 & 2.12, energy and momentum are conserved, and the relatively low binding energy of the orbital electron is ignored. The mass attenuation coefficient for Compton scattering σ/ρ is:

$$\frac{\sigma}{\rho} = \frac{N_A Z}{A}\sigma_e \tag{2.13}$$

where N_A is Avogadro's number, Z is the atomic number of the absorbing medium, A is the molecular mass of the absorbing medium, and σ_e is the Klein-Nishina cross section for Compton scattering [15]:

$$\sigma_e = 2\pi r_e^2 \left[\frac{1+\alpha}{\alpha}\left[\frac{2\,(1+\alpha)}{1+2\alpha} - \frac{ln\,(1+2\alpha)}{\alpha}\right] + \frac{ln\,(1+2\alpha)}{2\alpha} - \frac{1+3\alpha}{(1+2\alpha)^2}\right] \tag{2.14}$$

where r_e is the classical electron radius and $\alpha = h\nu/m_E c^2$.

2.3.3 Rayleigh (coherent) scattering

Unlike Compton scattering, *Rayleigh scattering* or *coherent scattering* is a nearly elastic event in which little-to-no energy is lost by the incident photon. No excitation or ionization occurs. The mass attenuation coefficient for Rayleigh scattering σ_R/ρ has the following proportionality:

$$\frac{\sigma_R}{\rho} \;\alpha\; \frac{Z}{(h\nu)^2} \tag{2.15}$$

The dependence of Rayleigh scattering on Z and $h\nu$ is similar to the photoelectric effect in that it is greater at high Z and low $h\nu$. However, the cross section of Rayleigh scattering is relatively small compared to other interaction types. In general, Rayleigh scattering contributes only a small percentage ($\sim$0-8%) of the total mass attenuation coefficient for $h\nu$ = 0.01 - 1.0 MeV [15].

2.3.4 Pair production

Photons with energy exceeding $2m_ec^2$ may be absorbed near an atomic nucleus to create an electron and a positron. This process is called *nuclear pair production*. Each created particle has a kinetic energy equal to the difference between the incident photon and the sum of the particle's mass energy $2m_ec^2$. The mass attenuation coefficient for nuclear pair-production κ/ρ is:

$$\frac{\kappa}{\rho} = \frac{N_A}{A}\kappa_a \tag{2.16}$$

$$= \frac{N_A}{A}\eta Z^2 P \tag{2.17}$$

where κ_a is the interaction cross of nuclear pair production per atom, $\eta = r_e^2/137 = 5.80 \times 10^{-28}$ cm^2/electron and P is a function of the initial photon energy $h\nu$ and the created positron's kinetic energy T^+ [15]). In general, nuclear pair production dominates in high $h\nu$ in high Z media.

High energy photons may also interact with the Coulomb force of an orbital electron to create a positron and electron. The orbital electron gains significant kinetic energy and is ejected, hence this process is called *triplet production* or *electronic pair production*. The minimum photon energy required for triplet production is $4m_ec^2$. The interaction cross section for triplet production per atom ${}_a\kappa_{electronic}$ is related to that of nuclear pair production ${}_a\kappa_{nuclear}$ by the following ratio:

$$\frac{{}_a\kappa_{electronic}}{{}_a\kappa_{nuclear}} \cong \frac{1}{CZ} \tag{2.18}$$

where C is a parameter that depends only on $h\nu$ (C $\cong$ 2 at 5 MeV, C $\cong$ 1 for $h\nu \longrightarrow \infty$).

2.3.5 Photon interactions and PET

Figure 2.3.1 is a plot generated by the National Institute of Standards and Technology (NIST) online cross section tool [18]. This plot shows the mass attenuation coefficients of the various photon interactions versus photon energy in cerium-doped lutetium-yttrium oxyorthosilicate (LYSO:Ce), a common scintillator used in PET. The composition of LYSO:Ce was assumed to be $Lu_{1.95}Y_{0.05}SiO_5$ with 0.2% Ce doping (for example, this composition

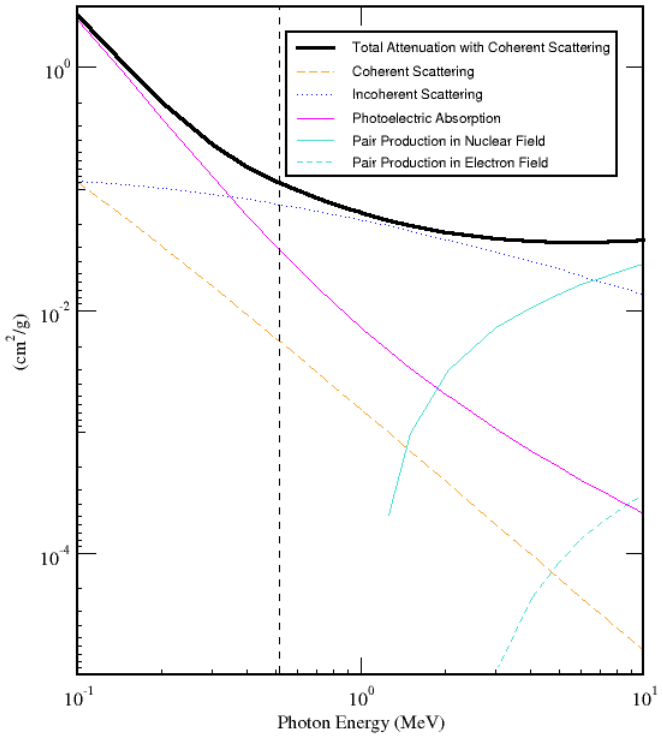

Figure 2.3.1: Mass attenuation coefficient versus photon energy in LYSO:Ce. The vertical dashed line represents 511 keV photons.

Table 2.3.2: Mass attenuation coefficients of ^{22}Na decay (2×511 keV, 1.275 MeV) in LYSO:Ce.

Interaction type	Mass attenuation coefficient for 0.511 MeV photons (cm^2/g)	Mass attenuation coefficient for 1.275 MeV photons (cm^2/g)
Photoelectric effect	3.24×10^{-2}	4.52×10^{-3}
Compton scattering	7.46×10^{-2}	4.91×10^{-2}
Rayleigh scattering	5.71×10^{-3}	9.56×10^{-4}
Pair production (nuclear)	0	2.62×10^{-4}
Pair production (electronic)	0	0
Total	1.13×10^{-1}	5.48×10^{-2}

was used here [19]). The majority of interactions at 511 keV are Compton scattering and the photoelectric effect. Mass attenuation coefficients for 511 keV annihilation photons in LYSO:Ce are given in Table 2.3.2.

The most desirable photon interaction in PET is the photoelectric effect. Unless Rayleigh scattering has occurred, photons absorbed in the scintillator via the photoelectric effect have reached the detector in the original annihilation photon trajectory. In practice, energy windows are applied to data which preferentially select photoelectric events over other events. This will be discussed in more in Section 3.3.3.

Compton events may have been scattered in the object being imaged (e.g. a patient, mouse, or phantom) or in the detector itself. The original trajectory of object-scattered annihilation photons cannot be precisely calculated for a single event. Compton imagers exist and are able to calculate cone trajectories based on energy and angular data to determine the position of annihilation (for environmental purposes [20] and medical imaging purposes [21, 22]). However, Compton-PET has not been demonstrated for preclinical scanners which demand very high spatial resolution.

Rayleigh scattering can be problematic in PET since photon trajectory is altered while photon energy change is negligible. These events cannot be discriminated against by setting energy windows. Unless forward-scattering occurs, Rayleigh scattering leads to event mispositioning. However, the relative probability of Rayleigh scattering versus the photoelectric effect for 511 keV in LYSO:Ce is nearly an order of magnitude lower (see Table 2.3.2).

Pair production never occurs when using pure β^+ emitters because annihilation photons are always ~511 keV. A minimum of $2m_oc^2$ and $4m_oc^2$ is required for nuclear and electronic pair production to occur, respectively. This condition is met for some positron emitters that also emit higher energy γ-rays. For example, ^{22}Na (which is not a clinically-used radionuclide due to its' very long half life) emits a 1.275 MeV γ-ray when it decays by β^+ emission. At

this energy, the relative cross section of pair production is quite small (see Table 2.3.2). Figure 2.3.1 shows that nuclear pair production only becomes significant as photon energy is increased beyond a few MeV. However, pair production is generally not a concern in PET since most clinically-used radionuclides do not have high energy γ-ray byproducts.

2.4 Photon Detection

PET detectors consist of a scintillating material optically coupled to a photodetector. The scintillating material stop incident photons and converts them into thousands of optical photons (visible light). Optical photons travel through the coupling medium to the photodetector, where they are absorbed and converted into electrical current for readout.

2.4.1 Scintillators

Scintillation is the emission of optical photons resulting from the passage of a charged particle. Photoelectrons and recoil electrons interact with the scintillating medium via Coulomb forces which produces electron-hole pairs and eventually optical photons. The number of interactions between photoelectrons/recoil electrons and the scintillating medium is proportional to its kinetic energy. Therefore, it is assumed that the number of optical photons produced is linear with incident photon energy.

The mechanism of scintillation differs between organic and inorganic scintillators. Organic scintillators are low cost and useful in photon counting devices. However, they are low Z materials which limits their practicality in PET (unless Compton imagers are used), and therefore will not be discussed.

The mechanism of scintillation for inorganic scintillators can be described by their crystal

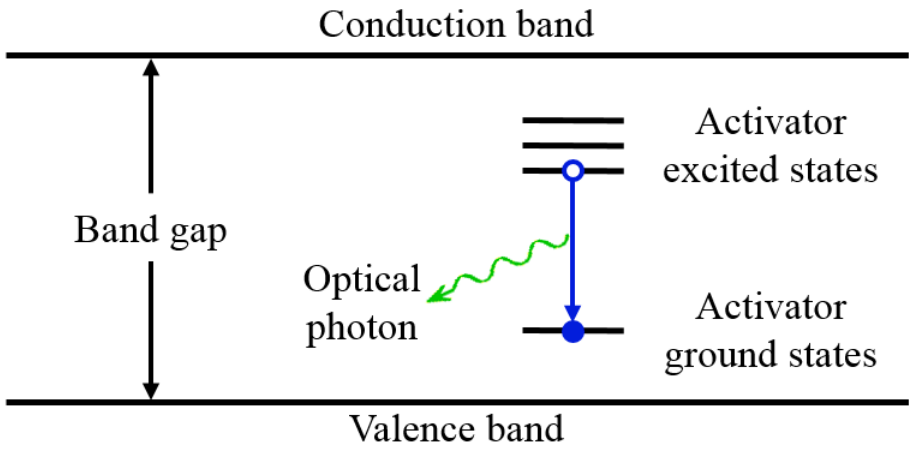

Figure 2.4.1: Scintillation from the deexcitation of activator sites within an inorganic crystal.

lattice structure illustrated in Figure 2.4.1. Two 'bands' exist in the crystal structure: the valence band and the conduction band. Electrons in the valence band are bound to the crystal, while electrons in the conduction band are free to migrate. The lower energy valence band and higher energy conduction band are separated by a band gap. Through Coulomb interactions with passing charged particles (i.e. photoelectrons or recoil electrons), many electron-hole pairs from the valence band are created. Valence band electrons are excited to the conduction band, while holes are free to drift. Eventually, electrons in the conduction band will return to the valence band accompanied by the emission of a photon with energy equal to the difference in energy states (i.e. equal to the band gap). In a pure crystal this process is inefficient, and the band gap is large such that the emitted photons are outside the visible spectrum.

In pure crystals, electron energy states within the band gap are forbidden. Impurities are introduced into the crystal lattice which create accessible energy states (called activator sites) within the band gap (Figure 2.4.1). Following the creation of an electron-hole pair, the hole can drift to an activator site and ionize it. Electrons in the conduction band can access these activator sites and momentarily hold an excited configuration. After a short period of time (typically $\sim 10^{-7}$s) the activator site will transition to ground state accompanied by the emission of an optical photon. Deexcitation through activator sites is more efficient in impurity-doped crystals than in pure crystal structures. Optical photons are within the

visible spectrum and have discrete energies equal to the energy difference in activator sites.

There are several factors to consider when choosing a scintillator for PET applications. Scintillators should be high Z materials in order to maximize the probability of photoelectric interactions. They must be transparent to the wavelength of optical photon emission to avoid significant self-absorption. The index of refraction should be matched to the photodetector as well as the coupling medium to minimize internal reflection at media boundaries. Optical photon emission should be in a spectral range that matches the photodetector's peak efficiency range. The light yield, or the number of optical photons emitted per MeV of the incident photon, should be high and linear with the incident photon energy.

Scintillation is not instantaneous but rather is characterized by a rise time and decay time. Rise time is (typically) defined as the time it takes for the scintillation output to reach from 10% to 90% its maximum intensity. Decay time is the time it takes for the scintillation output peak intensity to drop by a factor of $1/e$. The decay time can be further separated into two components, a fast (prompt) component τ_f and a slow (delayed) component τ_s. The fast component corresponds to the optical photons emitted from the deexcitation of activator sites as described previously. The slow component corresponds to optical photons emitted in competing processes. Some activator excited states may be forbidden to transfer directly to ground state. For example, thermal excitation of the excited activator site may be required before a transition to ground state. Additional steps in deexcitation causes delayed optical photon emission characterized by the slow component.

Scintillation output can be modelled with the following double-exponential [23]:

$$N(t) = Ae^{-t/\tau_f} + Be^{-t/\tau_s} \tag{2.19}$$

where $N(t)$ is the number of optical photons produced at time t and A and B are the output magnitudes of the fast and slow components, respectively.

Table 2.4.1: Common inorganic scintillators used in PET [24, 25, 26, 27, 28, 29, 30].

Scintillator	Density (g/cm^3)	Refractive index	Light yield (ph/MeV)	Decay time (ns)	Emission peak (nm)
NaI:Tl	3.67	1.85	41 000	230	410
CsI:Tl	4.5	1.79	66 000	800	550
BGO	7.13	2.15	8 200	300	480
LSO:Ce	7.4	1.83	26 000	40	420
LYSO:Ce	7.1	1.81	30 000	45	420
GSO:Ce	6.71	1.85	8 000	28	430
GAGG:Ce	6.63	1.87	46 000	90	520
LuAG:Pr	6.73	1.99	18 000	17	310
LaBr3:Ce	5.08	1.9	63 000	16	380

Compromises must often be made when choosing a scintillator for a PET detector. Consider Table 2.4.1 which is a short list of common scintillators used in PET. In the context of this work, LYSO:Ce stands out from this table because it has a relatively high light yield, short decay time, and wavelength of maximum emission matched with the photodetector peak detection efficiency ($\lambda = 420$ nm). LYSO:Ce also has widespread commercial availability.

One drawback to LYSO:Ce is that about 2.6% of lutetium is a naturally radioactive isotope ^{176}Lu. Figure 2.4.2 shows a simplified schematic of ^{176}Lu decay. The primary

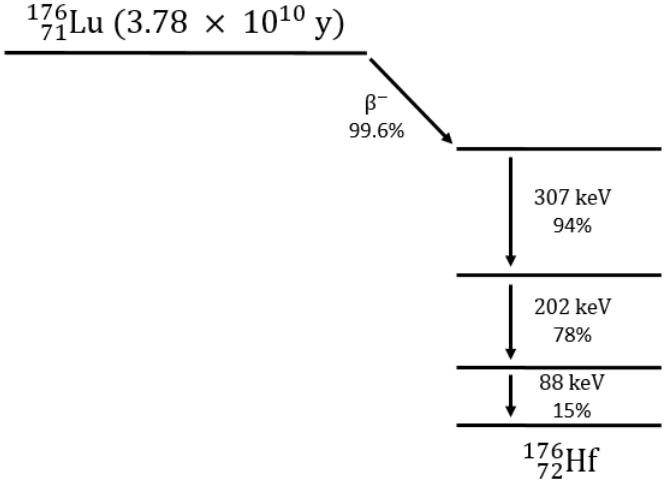

Figure 2.4.2: Simplified decay scheme of ^{176}Lu to ^{176}Hf. Intrinsic radioactivity from lutetium-containing scintillators contributes background noise to PET scans which can be problematic for acquisitions with low count rates.

mode of decay is by emission of a β^- accompanied by up to three γ-rays of 307, 202, and 88 keV. With a half-life of 3.78×10^{10} years, ^{176}Lu decay easily persists throughout the lifetime of a PET detector. Radioactivity that is generated by LYSO:Ce rather than by an external source is called *intrinsic radioactivity*. Intrinsic radioactivity can be problematic in situations with low count rates due to weak external sources. If both the 307 and 202 keV γ-rays are absorbed by the scintillator simultaneously, then the total energy of generated optical photons is equivalent to a scintillation event resulting from a 509 keV photon, which is nearly indistinguishable from 511 keV annihilation photons. Intrinsic radioactivity (as well as background radiation) can be corrected for by taking baseline measurements without the presence of external sources. In practice, intrinsic radioactivity represent a small fraction of all radiations absorbed in a PET scan.

2.4.2 Photomultiplier tubes

The next step in photon detection is to convert the generated optical photons into an electrical signal. The conventional photodetector in PET is the photomultiplier tube (PMT). PMTs are vacuum-sealed tubes that consist of a series of dynodes held at increasing voltages (see Figure 2.4.3). Optical photons travelling through the entrance window will strike the photocathode which emits a photolectron. With the help of a focusing grid for steering, the photoelectron is accelerated towards the first dynode, gaining sufficient kinetic energy to liberate secondary electrons. These electrons accelerate towards successive dynodes and liberate more electrons, resulting in an overall gain in the order of 10^6-10^7.

However, there is a fundamental problem with using PMTs in PET/MRI. The electron beam generated will experience a Lorentz force in the presence of a magnetic field, which causes the beam to bend. The PMT signal is compromised even in weak magnetic fields. Furthermore, PMTs are typically made with components that are metallic and not MR-safe. This is one reason why the current trend in PET detector development is to use solid-state

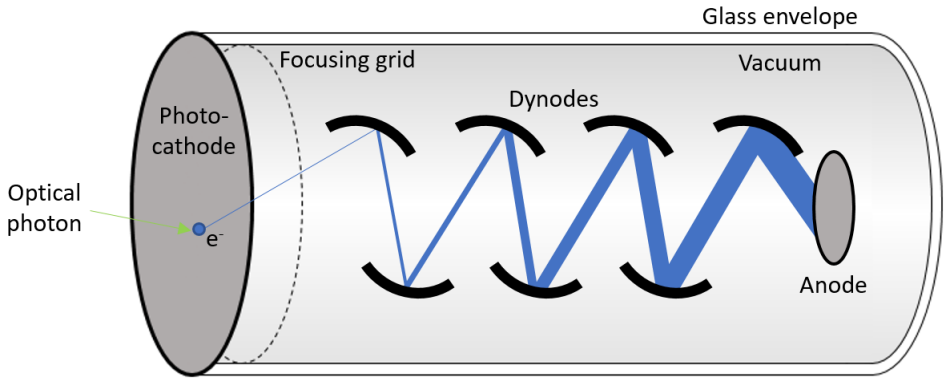

Figure 2.4.3: Schematic of a photomultiplier tube.

photodetectors rather than PMTs.

2.4.3 Silicon photomultipliers

Silicon photomultipliers (SiPMs) are solid-state photodetectors that are becoming increasingly common in PET. The schematic of a typical photodiode is shown in Figure 2.4.4. SiPMs consist of a parallel network of thousands of individual avalanche photodiodes. Each photodiode is a slab/wafer of doped silicon sandwiched between two contacts. Scintillation

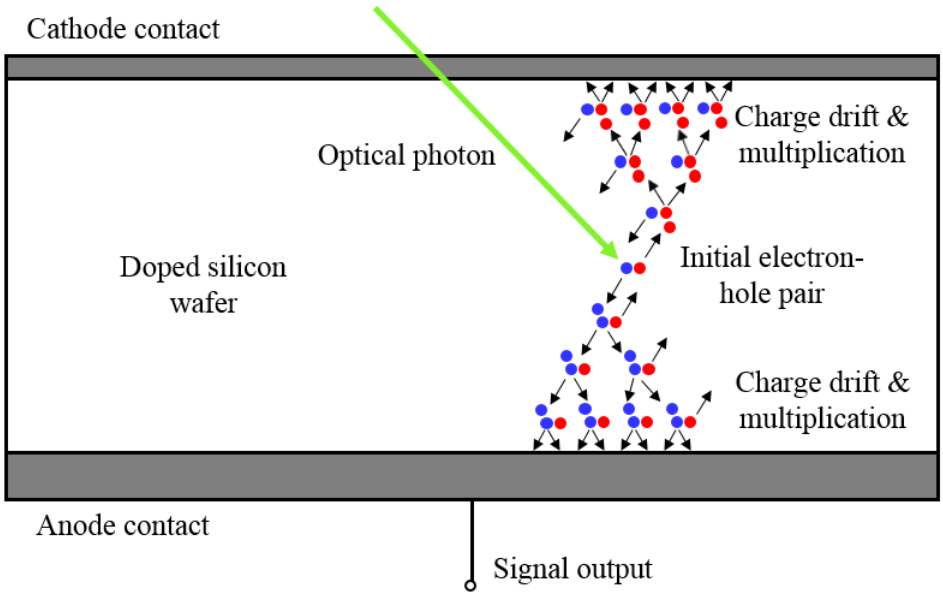

Figure 2.4.4: Diagram of an avalanche photodiode used in SiPMs, showing charge multiplication of electrons (blue) and holes (red) as they drift towards their respective contacts.

photons are absorbed via the photoelectric effect to create an electron-hole pair. The voltage bias between contacts is sufficiently high (i.e. beyond the photodiode breakdown voltage) such that electron-hole pairs accelerate towards their respective contacts and generate secondary electron-hole pairs (which will accelerate and generate tertiary electron-hole pairs, and so on). Photodiodes biased beyond their breakdown voltage are said to be operating in Geiger mode. Charge avalanche gain is on the order of 10^6. The avalanche continues indefinitely until the charge is quenched, supplied by a series resistor. An avalanche photodiode and quenching resistor pair (see Figure 2.4.5) is known as a microcell. Note that the photodiode represents the sensitive volume of the microcell, and the quenching resistor and any added microcell components constitutes dead space that cannot detect optical photons.

Figure 2.4.5 shows a simplified schematic of an 8-microcell sensor. Microcells are coupled together in parallel with a common cathode and a summed anode. Any given output signal at the anode is the sum of avalanche outputs of all microcells fired for a given scintillation event. The amplitude of each microcell avalanche is approximately the same regardless of how many optical photons are absorbed. One can think of individual microcell readout as binary; either "on" or "off" with no proportionality. Therefore, the amplitude of the summed anode output is linearly proportional to the number of microcells that fired for a

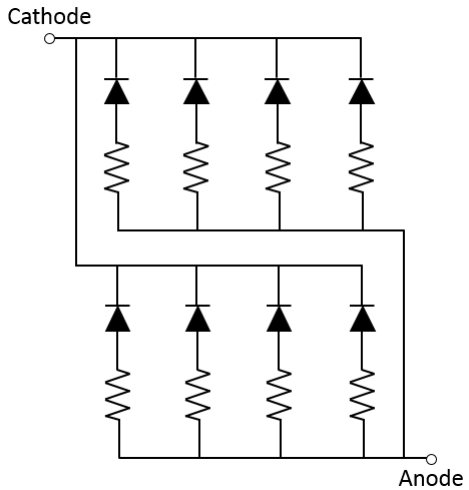

Figure 2.4.5: Schematic of a generic SiPM comprised of 8 microcells. Each microcell is an avalanche photodiode connected in series to a quenching resistor which halts the avalanche process. Outputs are summed into two terminals: the cathode (common) and the anode (standard output).

given scintillation event. Generally, it is assumed that every fired microcell is the result of one optical photon interaction (i.e. not multiple photons). SiPM output pulse height is then linearly proportional to the number of optical photons generated, and therefore is linearly proportional to the energy of the incident photon.

Saturation occurs when multiple optical photons interact with one microcell in avalanche before it is quenched. The resulting signal amplitude is not proportional to the number of optical photons reaching the SiPM in the scintillation event, since the summed charge excludes part or all of the signal otherwise generated by multi-photon events [31]. Consequently, the charge collected from the SiPM is non-linear with photon energy, energy resolution is artificially improved via energy histogram compression, and flood histograms are degraded [32]. Saturation may occur when scintillation events occur very close to the SiPM surface.

Three SiPM models from SensL were tested throughout this work: SensL's B-Series SPMArray4B (SiPM-B), C-Series ArrayC-30035-16P-PCB (SiPM-C), and J-Series ArrayJ-30035-16P-PCB (SiPM-J). Each of these SensL SiPMs are subsequent generations that improve on the previous design. SiPM-C has a significantly lower dark count rate, improving from 6.7 MHz to 0.3 MHz per pixel compared to SiPM-B. The SiPM-C also introduced a capacitively-coupled third terminal called the 'fast output' [33]. About 2% of the signal generated from a fired microcell is collected by the fast output, and the duration of the fast signal is approximately 100 times shorter than the standard output [33]. Furthermore, the terminal capacitance of the fast output is 12 pF versus the standard output terminal capacitance of 850 pF. The timing performance of SiPM-C fast output is significantly improved over the standard output of the SiPM-B. In their next generation, SensL released the J-Series SiPMs which retained the SiPM-C configuration with two major changes. First, microcell density was increased which consquently increased the photon detection efficiency (PDE). For SiPM-J and SiPM-C, the number of microcells per pixel is 5676 and 4774 microcells, respectively, while the PDE at 420 nm is 38% and 31%, respectively. Second, though not of

Table 2.4.2: Detector parameters according to manufacturer datasheets. Where applicable, data given at voltage bias of V_{br} + 2.5 V and V_{br} + 3.0 V and at temperatures of 21.0^{o}C and 25.0^{o}C for SensL and Hamamatsu photodetectors, respectively.

Detector	SiPM-B	SiPM-C	SiPM-J	MPPC
Array model	SPMArray4B	ArrayC-30035-16P-PCB	ArrayJ-30035-16P-PCB	S13361-3050AE-04
Active pixel area (mm^2)	3×3	3×3	3.07×3.07	3×3
Pixel array pitch (mm)	3.36	4.2	3.36	3.2
No. of microcells/pixel	4774	4774	5676	3584
Microcell fill factor (%)	64	64	75	74
Breakdown voltage (V)	24.0 - 25.0	24.2 - 24.7	24.25 - 24.75	48 - 58
Peak PDE λ_{peak} (nm)	420	420	420	450
PDE for λ_{peak} (%)	31	31	38	40
Gain (standard output)	3×10^6	3×10^6	2.9×10^6	1.7×10^6
Dark count rate (MHz)	6.7	0.300 (max 0.860)	0.405 (max 1.413)	0.5 (max 1.5)
Terminal capacitance (pF)	850	850	1000	320

concern for this work, the sensitivity of the SiPM-J was extended into the UV range.

Another type of SiPM used in this work was Hamamatsu's multi-pixel photon counter (MPPC) array S13361-3050AE-04 which have the standard cathode (common) and anode (summed output) terminals. MPPC specifications are similar to that of SensL's design except that it boasts a lower terminal capacitance of 320 pF, considerably lower than SiPM-C terminal capacitance of 850 pF. It is expected that a decrease in terminal capacitance will decrease the microcell recovery time and therefore facilitate higher event count rates. Various properties of Hamamatsu and SensL photosensors are listed in Table 2.4.2.

2.5 Lines of Response

PET imaging exploits positron annihilation and the fact that annihilation photons are emitted in opposite directions. PET requires an arrangement with opposing detectors, and typical PET detectors are set up as rings with in-plane 360° coverage of the target being imaged. When both 511 keV annihilation photons are absorbed, a *line of response* (LOR) is created which connects the detector elements that absorbed the annihilation photons. The width of the LOR is equal to the effective width of the detector elements (shown later in Figure 2.5.2). In theory, the event of positron annihilation must have occurred somewhere along the LOR. Millions of LORs are accumulated in order to obtain an image.

2.5.1 Limitations of spatial resolution

There are several fundamental limitations of spatial resolution that degrade PET images, some due to the underlying physics of PET and some due to the geometry of the detector. Three notable causes of spatial resolution degradation are positron range, acollinearity, and the parallax effect [17].

PET reconstruction algorithms attempt to estimate the distribution of tracers by measuring both anti-parallel annihilation photons. Technically, PET detectors are measuring the point of annihilation rather than the point of positron decay. There are two principle sources of uncertainty with position range that contributes to degradation of spatial resolution:

1) The positron's erratic and unpredictable path due to Coulombic interactions.

2) The positron's kinetic energy at the point of annihilation. Kinetic energy must drop until the positron can be in close proximity with an electron for a sufficient amout of time to allow for positronium formation.

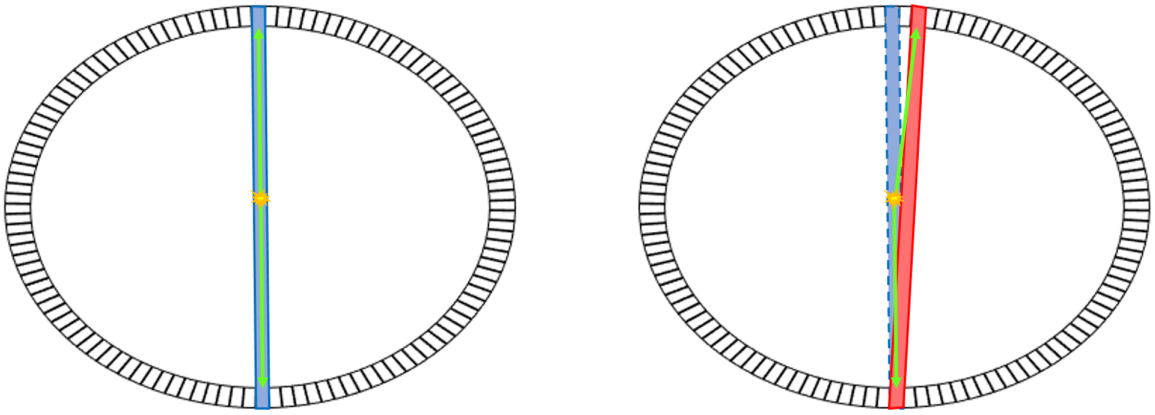

(a) (b)

Figure 2.5.1: Effect of acollinearity on LOR calculation for ring detectors. (a) If annihilation photons are collinear, then the calculated LOR contains the point of annihilation. (b) For acollinear events, the calculated LOR is shifted and may not coincide with the point of annihilation. The blue and red lines represent LORs generated from collinear and acollinear events, respectively.

The degree of spatial resolution degradation due to positron range depends on the direction of propogation of the annihilation photons. In Figure 2.2.1 in Section 2.2, a diagram of positron emission to annihilation was shown. In this figure, the *effective positron range* is defined as the distance from the parent radionucide to the nearest point of a positron annihilation photon path. Effective positron range depends on the angle of annihilation photon propogation with respect to the axis intersecting the parent radionuclide and the point of annihilation.

Figure 2.5.1 demonstrates how acollinearity causes positional discrepancy between the generated LOR and the point of annihilation. The effect of acollinearity on image reconstruction depends on the detector size (i.e. distance between opposing detectors) and scintillator pixel size. Since LOR width is defined by the effective width of scintillator pixels, reconstruction error occurs if acollinear events cause annihilation photons to be absorbed in neighbouring scintillator pixels versus collinear events (i.e. red vs blue LORs in Figure 2.5.1). Acollinear photons deviate more from collinear trajectories as distance from the annihilation point to the detector increases. Therefore, detectors with larger ring diameters are affected more by acollinearity than small detectors.

Unlike positron range and acollinearity, the parallax effect is a symptom of the detector geometry. In pixellated PET detectors, an event LOR is constructed by connecting the scintillator crystals the photons were absorbed in. In general, the interaction point of the annihilation photon inside the scintillator is not known. Therefore, spatial resolution is defined by the scintillator crystal size. The effective width of detector elements in coincidence varies spatially. In Figure 2.5.2, the green LORs are events that occur near the centre of the field of view (FOV) which approach scintillator crystals head-on. These LORs are as thin as the detector elements themselves. However, the blue LORs at oblique angles are wider because the effective scintllator crystal size is greater. LOR broadening in this manner is called *parallax error*. The magnitude of parallax error depends on the size of the scintillator elements and the radius of the PET detector ring.

2.5.2 Parallax error and depth of interaction

The parallax effect may be minimized if intra-crystal positioning information can be extracted. If the *depth of interaction* (DOI) within the scintillator crystal is known, the effective thickness of the crystal at the FOV edge can be reduced. Figure 2.5.2 demonstrates how LOR width at oblique angles can be reduced using DOI information.

Two common methods of DOI measurement are dual-ended readout and dual-layer offset (DLO) scintillators. Dual-ended readout detectors couple photosensors at both ends of the scintillator crystal. DOI can be calculated by:

$$DOI = \frac{E_{top} - E_{bottom}}{E_{top} + E_{bottom}} \tag{2.20}$$

where E_{top} and E_{bottom} are the energies (i.e. signal amplitudes) measured by the top and bottom photosensors, respectively. Dual-ended readout presents a continuous measure of

DOI, where the depth-positioning accuracy depends on the characteristics of the scintillator and photosensor used. There are two primary disadvantages of dual-ended readout. First, the number of signal output channels are doubled, which increases the volume and complexity of readout electronics. Second, the additional photosensor layer contributes thickness non-sensitive to annihilation photons which may present problems in size-restricted applications such as preclinical PET inserts.

DLO scintillator arrays contain two layers of pixels in which the top layer is positioned at a half-crystal pitch offset with respect to the bottom layer. The effective width of oblique LORs is reduced since the length of scintillator crystals is reduced. DOI accuracy with DLO arrays depends on the thickness of scintillator layers. Unlike dual-ended readout, DLO arrays allow for discrete measure of DOI.

2.5.3 Time of flight

PET detectors with fast timing characteristics can utilize photon arrival time to estimate positron annihilation position. Consider a PET detector with a field-of-view (FOV) of 30 cm. Annihilation photons that originate at the centre of the FOV, travelling at c_{air}=29.98 cm/ns in air, will each reach opposing detectors at ~500 ps following annihilation. However,

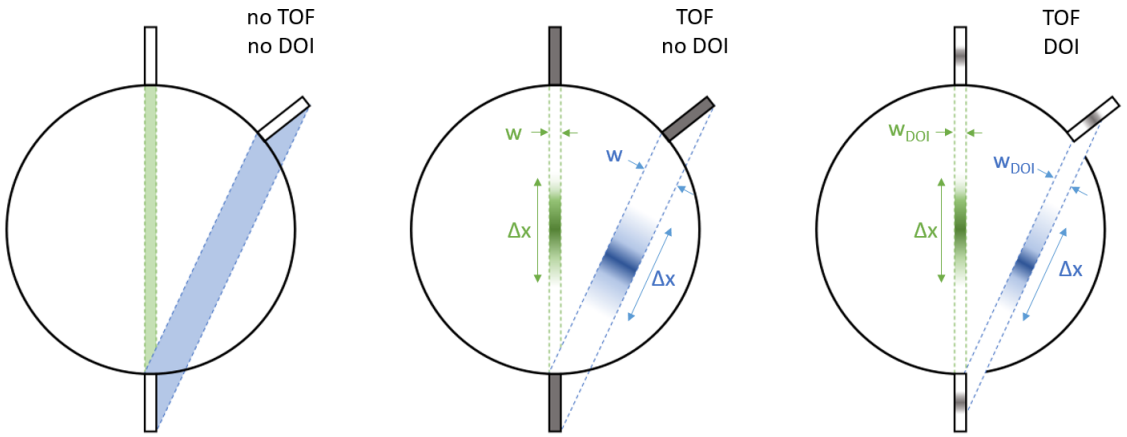

Figure 2.5.2: Demonstration of TOF and DOI. LOR is shortened to length Δx using TOF information, while LOR width is reduced to w_{DOI} using DOI information.

annihilation photons originating 5 cm off centre in the direction of propogation will reach opposing detectors at different times. The first photon travels 20 cm and arrives in ∼667 ps, while the second photon travels 10 cm and arrives in ∼333 ps. If photon arrival time were known exactly, the position of annihilation along the LOR offset from centre is d:

$$d = \frac{d_1 - d_2}{2} \tag{2.21}$$

$$= \frac{c(t_1 - t_2)}{2} \tag{2.22}$$

$$= \frac{30.0\frac{cm}{ns}(0.667ns - 0.333ns)}{2} \tag{2.23}$$

$$\approx 5cm \tag{2.24}$$

where d_n is the annihilation-to-detector distance and t_n is the flight time of photon n. In general, the off-centre displacement is:

$$d = \frac{c\Delta t_{arrival}}{2} \tag{2.25}$$

where $\Delta t_{arrival}$ is the difference in photon arrival times. The concept of utilizing photon arrival time to estimate event positioning is known as *time of flight* (TOF).

TOF-PET detectors are far from perfect, and several factors contribute to degradation of time performance. Photon arrival time depends on the depth of interaction and crystal thickness. The index of refraction of 420 nm (∼3 eV) optical photons in LYSO:Ce is $n_{3eV} \approx 1.81$, and therefore optical photons travel a factor of 1.81 slower towards the photosensor than 511 keV annihilation photons ($n_{511keV} \approx 1$) do. For annihilation photons originating at the centre of the FOV, a photon arrival time difference may arise because one annihilation photon is absorbed near the top of the scintillator while the other is absorbed near the

bottom. Second, photon arrival time ideally measures the detection of ballistic photons, i.e. the first few optical photons that reach the photosensor. Statistical fluctuations in ballistic photon arrival time are due to photosensor PDE as well as internal reflection/absorption in the scintillator/photodetector coupling interface. Third, there are timing uncertainties of the photosensor and processing electronics themselves.

The spatial uncertainty Δx that can be calculated using TOF information is related to the *coincidence timing resolution* (CTR) of the detector:

$$\Delta x = \frac{c \cdot CTR}{2} \tag{2.26}$$

Figure 2.5.2 demonstrates the difference in LOR length with and without TOF. Without TOF (left diagram), the point of annihilation between detector elements is not known. However, LOR length is reduced to Δx when using TOF information (centre diagram). With current technology, time resolution of several hundred ps has been reported, with a clinical TOF-PET target of 100 ps [34]. Setting CTR = 100 ps in Eq. 2.26, the spatial uncertainty is ∼1.5 cm. At a more reasonable time resolution of 500 ps, ∼7.5 cm can be resolved, which is not particularly useful when non-TOF spatial resolution has reached 3-4 mm. Absolute positioning with TOF is even less useful for preclinical PET detectors of ∼1 mm spatial resolution or better.

TOF information is beneficial because it constrains the event position along the LOR which increases the signal-to-noise ratio and reduces noise propogation along LORs when using iterative image reconstruction algorithms [35]. The relative gain in sensitivity (S_{gain}) of TOF-PET versus non-TOF-PET is:

$$S_{gain} = \frac{D}{1.6\ \Delta x} \tag{2.27}$$

where D is the size of the imaged object, and 1.6 is a factor accounting for filtering in image processing (derived in [36]).

2.6 PET Detector Designs

2.6.1 Monolithic versus pixelated scintillators

Scintillators may be monolithic or pixelated. *Monolithic* scintillators consist of a continuous block of scintillating material which require position-sensitive photodetectors in order to obtain positional information. When annihilation photons are absorbed, optical photons are emitted isotropically. Monolithic scintillators are typically wrapped with a light-absorbing material such as black paint or black tape. This way, only *ballistic* optical photons reach the photodetector (i.e. unreflected, unscattered photons that reach the photodetector in a straight line). Photons approaching the photodetector at oblique angles greater than the critical angle of the scintillator/photodetector interface (defined by Snell's law of refraction) are not transmitted. In Figure 2.6.1a, the green cone represents the optical photons that transmit from the scintillator to the photodetector. Position is calculated by taking the energy-weighted centroid of the transmitted optical photons.

Pixelated scintillators consist of arrays of individual scintillating crystals separated by some optical boundary such as air gaps or enhanced specular reflector (ESR, 3M^{TM}, Maplewood, MN). Optical photons reflect off inter-crystal boundaries until they are directed towards the photodetector. Readout of pixelated scintillators require coupling strategies such as one-to-one scintillator/photodetector coupling or light-sharing designs in order to obtain positional information of scintillation events. Some optical photons may transmit through inter-crystal boundaries; this is called *optical cross-talk*. Cross-talk is generally not a concern as long as it is uniform across the scintillator array, but may degrade detector performance

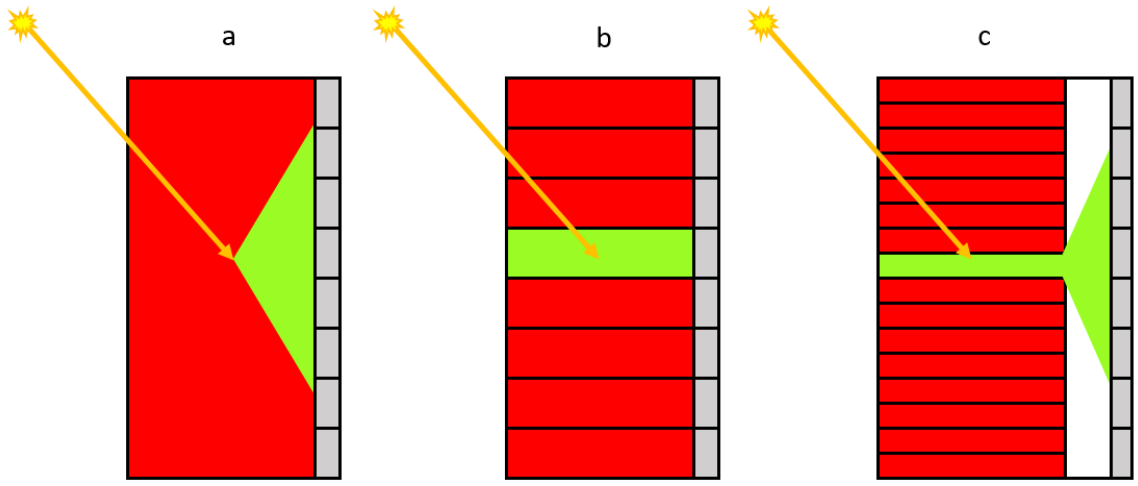

Figure 2.6.1: Scintillators (red) coupled to an 8-pixel SiPM array (gray) with the following designs: (a) monolithic scintillator, (b) pixelated scintillator and one-to-one coupling, (c) pixelated scintillator and light-sharing, with a light guide (white) coupled between the scintillator and SiPM arrays.

at edge or corner crystals that are not completely surrounded by neighbouring crystals.

2.6.2 One-to-one coupling versus light-sharing designs

All SiPM array measurements in this work are done with pixelated scintillators. There are two strategies for coupling scintillator arrays to SiPM arrays: *one-to-one coupling* and *light-sharing*. Figure 2.6.1b shows an example of one-to-one coupling where each scintillator crystal is directly coupled to a SiPM pixel with the same crystal/pixel pitch. In light-sharing designs (Figure 2.6.1c), the scintillator crystal density is greater than the SiPM pixel density. In order to obtain positional information from scintillation events, a light diffuser (or *light guide*) is inserted between the scintillator and SiPM arrays. Optical photons generated in one scintillator crystal are spread over several SiPM pixels, and the scintillation crystal is identified by taking the energy-weighted centroid of SiPM pixel outputs. Light guides are typically borosilicate glasses that are ideally refractive-index matched to the scintillator and SiPM optical window for optimum light transmission. Better spatial resolution of a PET system can be achieved by decreasing the scintillator crystal size. However, as scintillator

crystal size decreases, the relative volume of reflector/inter-crystal boundaries increases. In general, optical photons encounter reflector boundaries more often and the probability of being absorbed before reaching the photodetector increases. Therefore, very small crystal sizes lead to light loss and sensitivity loss. A compromise must be made between spatial resolution and crystal resolvability when choosing scintillator crystal size.

2.7 First-Generation PET Insert

The first-generation PET insert, shown in Figure 2.6.3, was built to fit within a Bruker 70/20 7T MRI. Inside the light-tight enclosure is a ring of 16 light-sharing detector modules (Figure 2.6.2). Each module consists of two through-hole 4×4 SensL SPMArray4B SiPMs coupled to a DLO LYSO:Ce array. The DLO array consists of a 9×21 array of 1.2×1.2×4 mm^3 crystal top layer and 10×22 array of 1.2×1.2×6 mm^3 crystal bottom layer; 409 total crystals with 1.27 mm pitch. A 1.0 mm borosilicate light guide is used as a light diffuser, and is coupled between the scintillator and SiPM arrays with optical grease. Each detector module output is connected via mini HDMI (Type C) and input into a detector interface board (DIB) via HDMI (Type A). Data acquisition is done using the OpenPET system, described later in Section 3.2.3. The first-generation PET insert is described in more detail here [37].

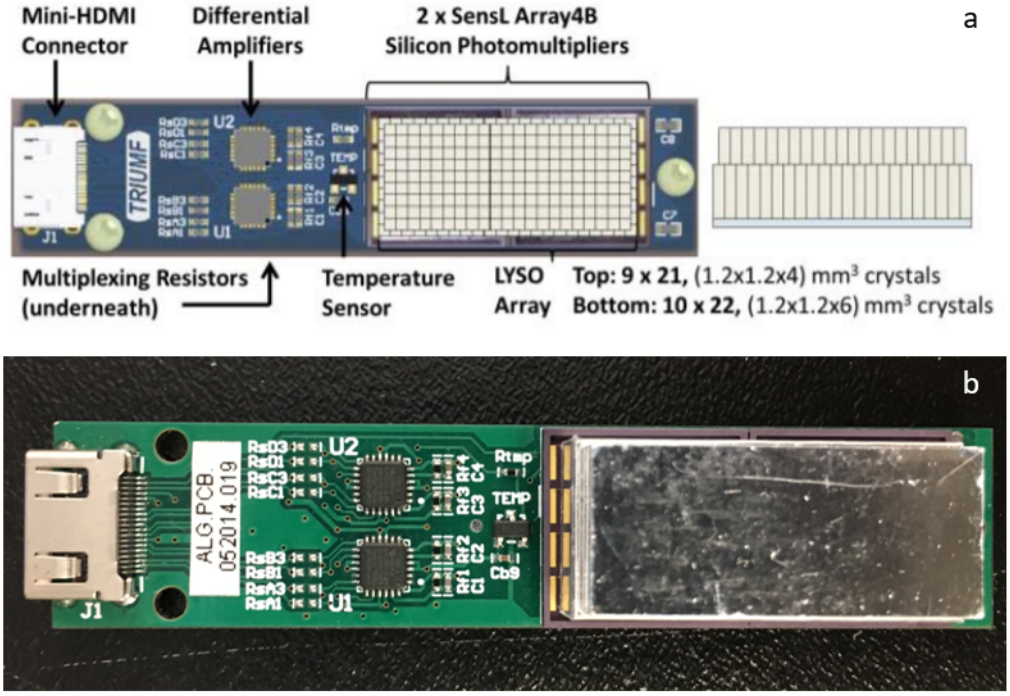

Figure 2.6.2: (a) Diagram and (b) image of a first-generation detector module. Reproduced with permission [37] ©2016 IEEE

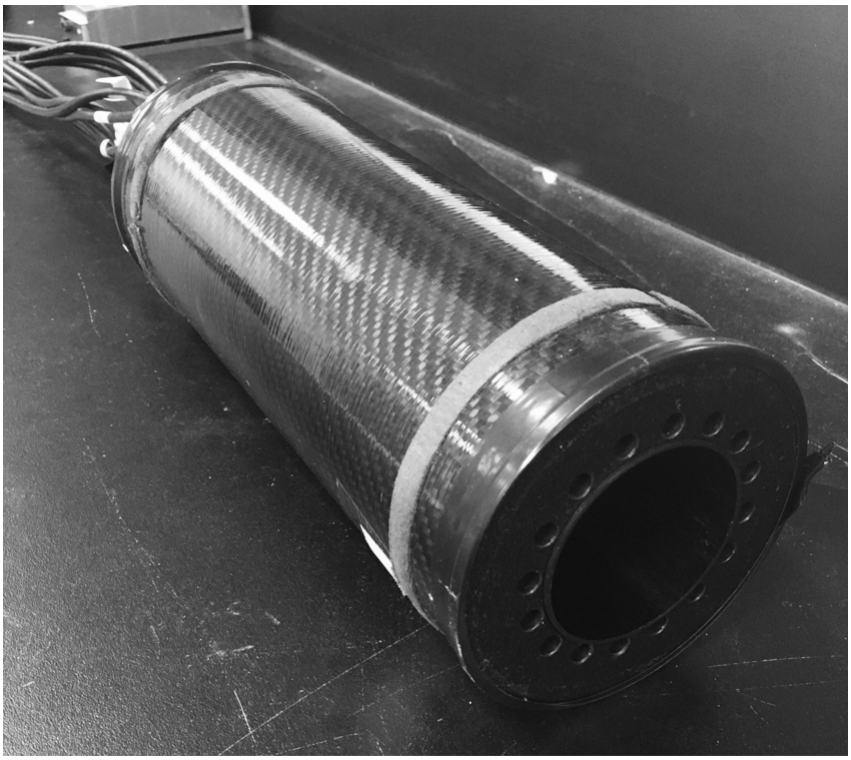

Figure 2.6.3: The first-generation PET insert, consisting of a ring of 16 detector modules mounted in a light-tight enclosure.

Chapter 3

General Methods

3.1 Detector Readout

3.1.1 Resistor-based charge division multiplexing

Pixellated photodetectors such as SiPMs require complementary circuitry that accept detector cathode/anode pins as input and manipulate the signals for subsequent acquisition hardware. Detector readout is done in this work by custom printed circuit boards (PCBs) that are designed to tie all SiPM cathode signals to common ground and to convert SiPM anode signals to a form that can be processed by acquisition hardware. The SensL and Hamamatsu photosensors described in Section 2.4.2 & 2.4.3 have a total of 16 anode signals per 4×4 array, one anode signal per pixel. Each signal can be read out individually, however this can be impractical and expensive in full PET systems with a large number of output channels. One way of minimizing output channel number is by *multiplexing* output signals. Multiplexing reduces the number of output signals by summing anode outputs in a strategic manner that preserves both amplitude and positional information. Figure 3.1.1

shows a resistor-based charge division multiplexing circuit that reads in 32 anode channels from two side-by-side 4×4 photosensor arrays and combines them into four output channels. Individual SiPM pixel outputs are spatially separated by a network of row/column resistors and summed into four corner outputs A-D. The energy of a measured scintillation event is simply the sum of the output amplitudes:

$$E = A + B + C + D \tag{3.1}$$

The x- and y- coordinates of the scintillation event can be calculated as the energy-weighted centroid of the signals:

$$x = \frac{(B + C) - (A + D)}{A + B + C + D} \tag{3.2}$$

$$y = \frac{(A + B) - (C + D)}{A + B + C + D} \tag{3.3}$$

Resistor values are chosen such that the position of a scintillation event is approximately linearly proportional to the A-D output signals based on Equations 3.2 & 3.3.

3.1.2 PCB readout boards

Two detector PCB boards were used in this work (Figure 3.1.2). Standard output readout is similar for both PCB boards. Signals are multiplexed as shown in Figure 3.1.1. The four corner outputs are each amplified with Analog Devices (Norwood, MA) ADA4932 operational amplifiers (op-amps) and transmitted out as 100Ω differential signals via standard HDMI cables. Op-amp bias and detector bias are also supplied via HDMI.

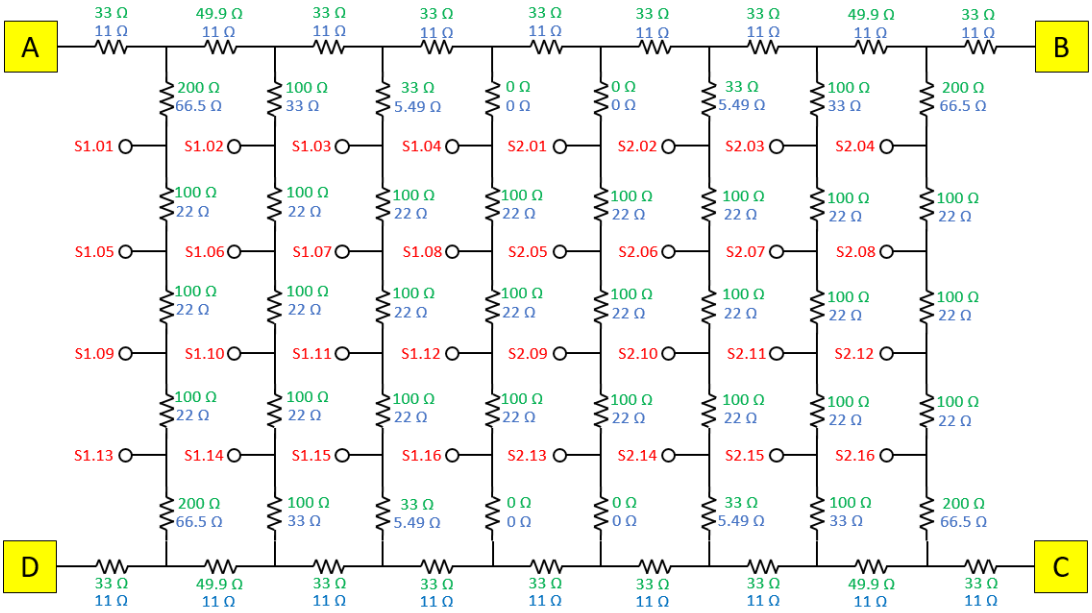

Figure 3.1.1: Charge-division multiplexing circuit schematic designed to read out two side-by-side 4×4 SiPM arrays. The 32 output channels are summed into four outputs (yellow, labelled A-D), which are later amplified and processed to provide event positioning. Labelled red are SiPM signal inputs, S1.01-S1.16 for the 16 outputs of the left SiPM and S2.01-S2.16 for the 16 outputs of the right SiPM. Each SiPM input is separated by a row and column resistor with values in green and blue for the first- and second-generation readout boards, respectively.

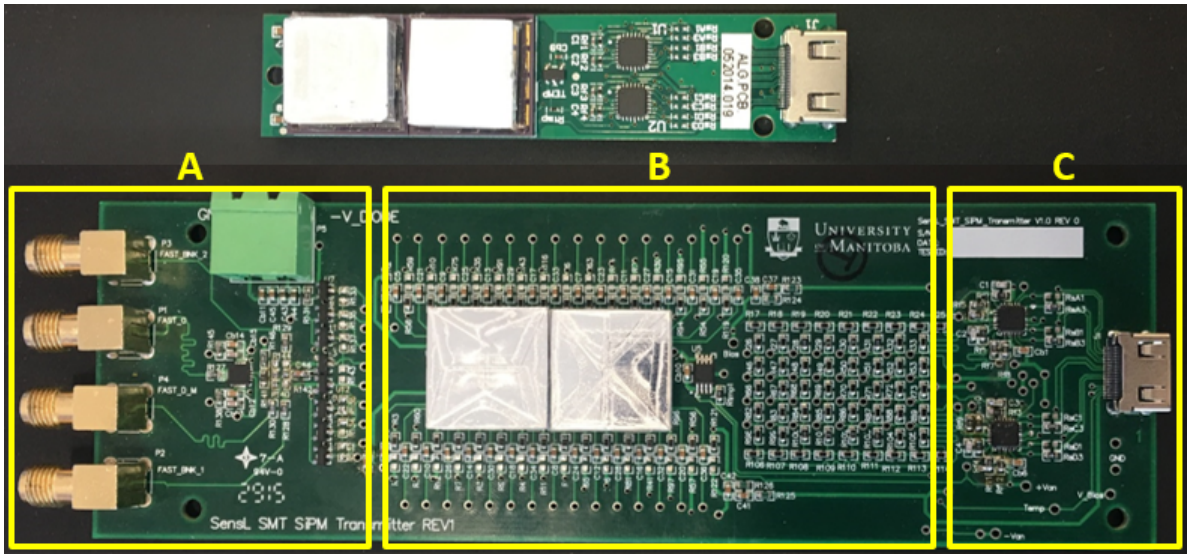

Figure 3.1.2: First-generation board (top) with two 4×4 SiPM-B arrays via through-hole attachment, and second-generation board (bottom) with two removable 4×4 SiPM-C arrays via header attachment. A) SensL-C fast output with four SMA outputs: two unamplified 16-channel-summed outputs, on-board amplified 32-channel-summed output, and Schottky diode output. B) Standard outputs with resistor-based charge division 32-to-4-signal multiplexing circuit. C) Multiplexed signal on-board amplification of standard outputs, conversion to 100Ω differential signals, and transmission to HDMI.

Several differences between the PCB readout boards exist. The first-generation board is much more compact since it was optimized for use in small-animal ring structures. Resistor values of the multiplexing circuit were decreased from the first-generation to the second-generation boards (green and blue values in Figure 3.1.1, respectively) which reduced the time constant of the circuit. The time constant and its consequence on performance will be discussed in Section 3.3.5.

The biggest modification to the second-generation readout board is that it can read out the 'fast' outputs of SiPM-C arrays. A schematic of how fast outputs are summed is shown in Figure 3.1.3. There are three timing readout options on these boards. Individual arrays may be read out through the bank SMA connections Fast_B1 and Fast_B2. The bank signals require external amplification for subsequent processing. Another readout option is the Fast_Out output which sums all 32 fast outputs and amplifies them with an on-board Texas Instruments (Dallas, TX) THS4303 op-amp. Left out of Figure 3.1.3 is the Schottky diode readout option, which was not investigated in this work.

3.1.3 Detector interface boards

The PCB readout boards are connected to a detector interface board (DIB) via HDMI (Figure 3.1.4). Energy signals A-D via HDMI output from the PCB readout boards are transmitted as 100Ω differential signals, which the DIB converts to 50Ω single-ended signals for compatibility with subsequent acquisition hardware. DIB output signals are transmitted via SMA connectors. The DIB also supplies the SiPM bias voltage and PCB readout board op-amp bias via HDMI.

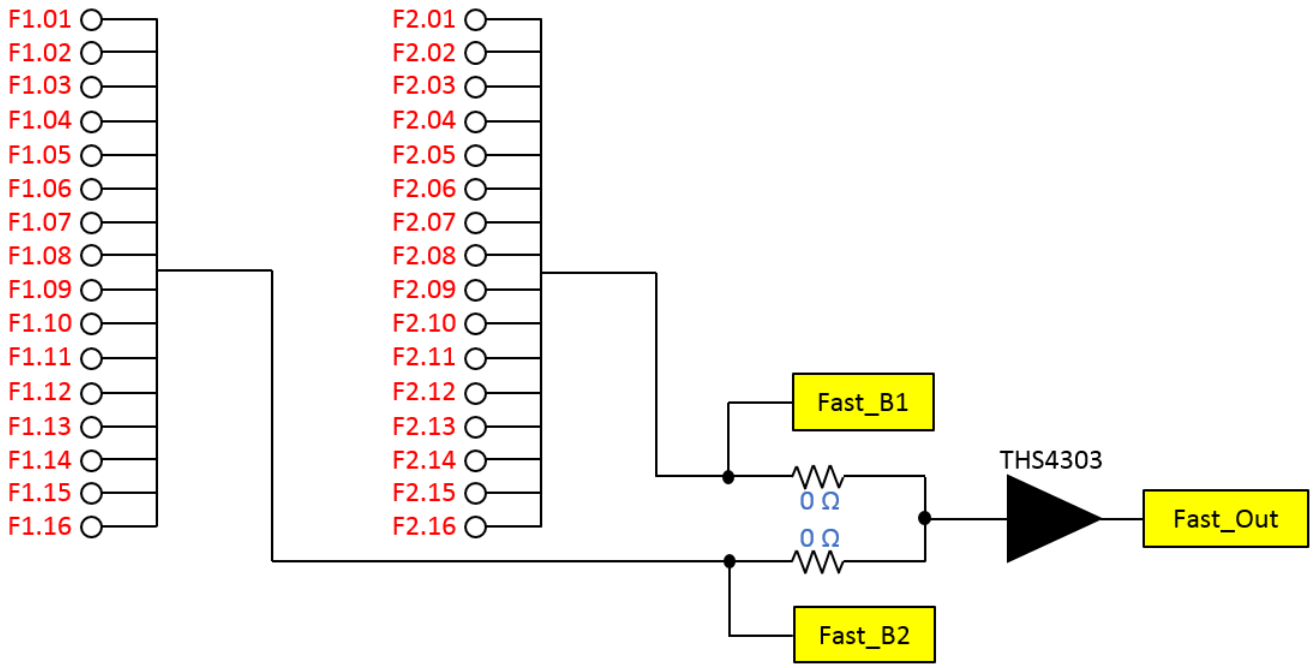

Figure 3.1.3: Simplified schematic of timing readout (i.e. fast output) implemented in the second-generation PCB board. The 4×4-summed fast outputs may be read out through the bank outputs (Fast_B1 & Fast_B2), or summed as an 8×4-to-1 output (Fast_Out) amplified by a THS4303 op-amp.

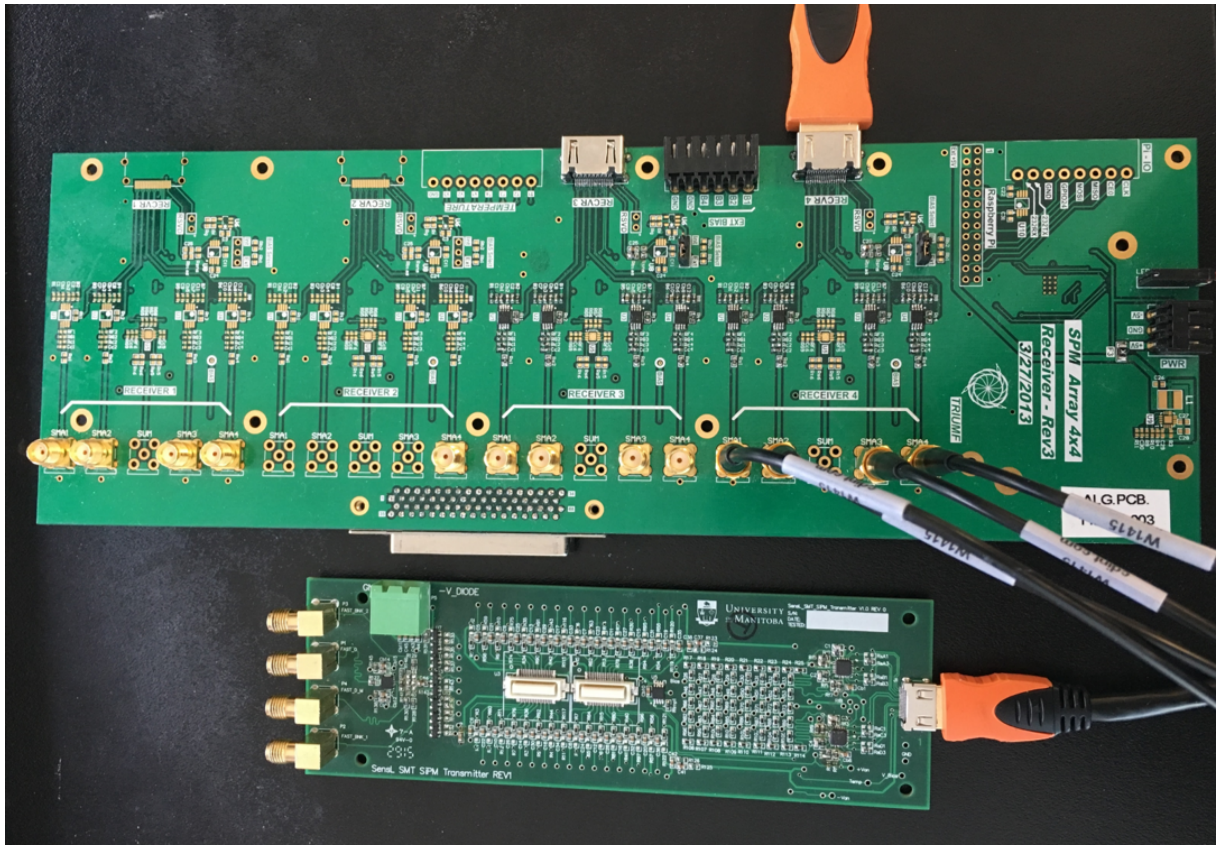

Figure 3.1.4: Detector readout board connected a detector interface board via HDMI, with four 50Ω outputs via SMA connectors.

3.2 Data Acquisition

Obtaining coincidence event data from detector readout board signals requires dedicated acquisition hardware. In general, data acquisition systems control when events are triggered and convert signals to a form that can be sampled and saved. In this work, three different acquisition systems were used: Nuclear Instrumentation Module (NIM) standard electronics, the DRS4 Evaluation Board V5 (Paul Scherrer Institute, Switzerland), and the OpenPET system (Lawrence Berkeley National Laboratory, CA).

Figure 3.2.1: NIM chassis containing several NIM modules for data acquisition.

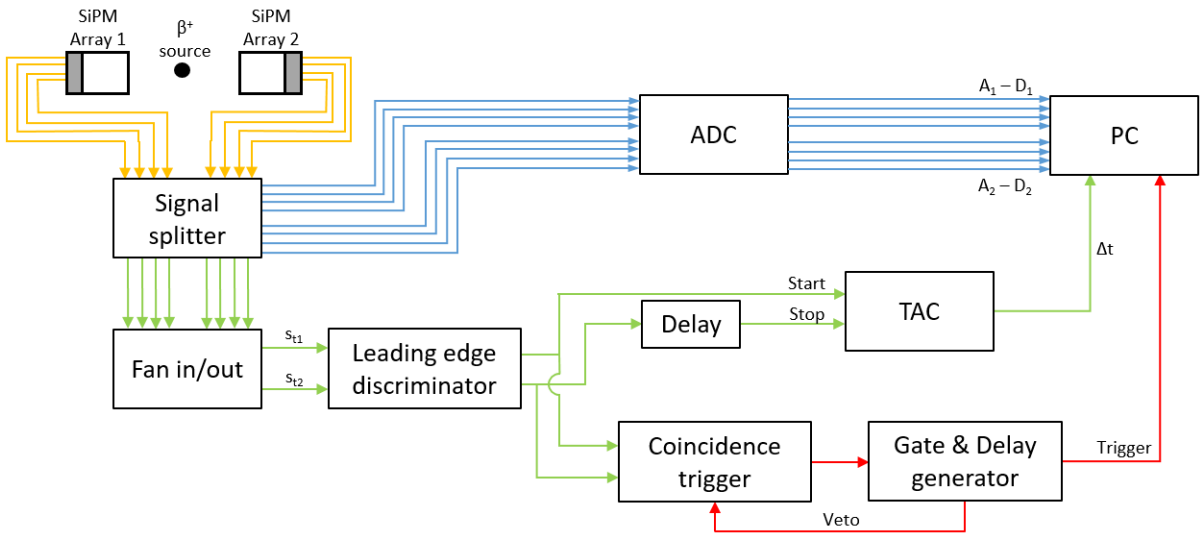

Figure 3.2.2: Schematic of a general acquisition setup using NIM electronics. Yellow lines are the A-D multiplexed signals, while blue and green lines are the energy and time signal paths, respectively.

3.2.1 NIM electronics

NIM acquisition systems are comprised of several modules that perform diverse individual tasks. By following specifications defined by the NIM standard, modules from different manufacturers can be used interchangably. Figure 3.2.1 is an image of our NIM chassis, showing a variety of modules from several manufacturers. Signal transmission between NIM modules is done with coaxial cables with LEMO or BNC connectors.

Figure 3.2.2 is a general schematic for NIM-acquired timing measurements done in this work. Two detectors in coincidence, SiPM Array 1 and SiPM Array 2, are positioned opposite each other with a positron source centred between them. DIB outputs (yellow lines) were split by a Phillips Scientific (PS) Model 778 amplifier, one for energy/positioning information (blue lines) and one for timing information (green lines). Energy signals A-D for each detector were input to a Mesytec MSCF-16-F module, which is a shaping amplifier with active baseline restoration.

Time signals were summed into a PS Model 740 linear fan in/out into two time sig-

nals s_{t1} and s_{t2} from SiPM Array 1 and 2, respectively. Time pulses are input to a CAEN N845 leading edge discriminator (LED). When time pulse amplitude surpasses a user-defined threshold, the LED outputs a transistor-transistor logic (TTL) pulse. TTL pulses are standard square pulses with 2.4 - 5.0 V amplitude. LED TTL outputs are the time start and stop pulses, with a delay module in the stop signal path if necessary. An ORTEC 567 time-to-analog converter (TAC) measures the time difference Δt between the arrival of LED TTL pulses SiPM Array 1 and 2, then produces an analog output signal with amplitude proportional to Δt.

LED TTL outputs are also fed into a PS Model 756 logic unit. When set to coincidence mode, the logic unit will output a TTL pulse only when the two LED input TTLs overlap. Users can adjust the width of LED TTL output pulses, which defines the time window of the coincidence events. Large time windows due to wide LED TTLs may cause the coincidence logic unit to trigger on random events, i.e. coincidence events resulting from two different annihilation events. Small time windows due to short LED TTLs may result in loss of true coincidence events because the time window is smaller than the difference in photon arrival times. Since timing measurements in this work involved setups with low count rates, the time window used was relatively wide and ranged from 100-250 ns.

The coincidence logic unit TTL is the master trigger which controls when events are recorded. The master trigger is fed to a PS Model 794 gate/delay generator, which has several TTL inputs that output TTL signals with user-defined width and delay. In this work, four gate/delay TTL outputs were used:

1) Energy sample-and-hold trigger. Time of this TTL is adjusted such that it coincides with the peak of the shaping ampifier output (i.e. the peak of A-D signals).

2) Timing sample-and-hold trigger. This TTL triggers digitization of the amplitude of the TAC output pulse.

3) Coincidence veto. The LED has a veto input option. The coincidence logic unit does not output a coincidence TTL pulse as long as the veto input receives a TTL from the gate/delay. The coincidence veto TTL duration is adjusted to provide adequate time for downstream electronics to digitize and record coincidence events and for the SiPMs to quench/recover.

4) Start-up veto. The data acquisition cards used for event digitization had a short start-up delay. At the moment a data acquisition is started, the acquisition software triggers the gate/delay to produce a ∼1s TTL to veto event digitization and allow for the data acquisition cards to start up.

TTL 1) and 2) are triggers input into two custom made sample-and-hold modules (Niagara Engineering Works Inc, Winnipeg, MB). When triggered by the gate/delay TTLs, samples are taken of the shaping amplifier A-D signals and of Δt from the TAC. Samples are held for 4 μs. During this time, held samples are digitized by two National Instruments PCI-6133 data acquisition cards (one for energy and one for timing sample-and-hold modules). The magnitude of held samples is assigned a voltage value up to a maximum 1.25 V. Digitization is controlled by National Instruments LabWindows/CVI software. Digitized signals are packaged into 14-bit comma delimited list-mode events. With the setup shown in Figure 3.2.2, one list-mode event would contain nine 14-bit values separated by commas (A_1,B_1,C_1,D_1,A_2,B_2,C_2,D_2,Δt). The National Instruments acquisition cards and software is described in greater detail by Goertzen *et al* (2013) [38].

3.2.2 DRS4 Evaluation Board V5

The DRS4 Evaluation Board V5 (Figure 3.2.3) is a waveform-capturing device developed by Paul Scherrer Institute (Villigen, Switzerland) . The DRS4 board is capable of sampling four input SMA channels at 5 giga-samples per second (GS/s) with 1024 sampling points.

Readout is done with an Analog Devices (Norwood, MA) 14-bit AD9245 analog-to-digital converter (ADC) and a Xilinx (San Jose, CA) Spartan 3 field-programmable gate array (FPGA). Rather than outputting a digitized value of the signal amplitude, the DRS4 digitizes each channel waveform in 1024 bins. Acquisition control and data transfer (20 MB/s) is done through a USB 2.0 bus. For more detail, see the DRS4 user manual [39].

Figure 3.2.4 displays the DRS4 oscilloscope software. The DRS4 software interface is similar to a standard digital oscilloscope. Using this interface, users can calibrate the system, choose single/coincidence triggers, set LED thresolds, set acquisition duration and/or count number, and save output waveforms for further processing.

3.2.3 OpenPET

The prototype PET insert currently uses the OpenPET system (Lawrence Berkeley National Laboratory, Berkeley, CA) for data acquisition. Figure 3.2.5a shows an image of the OpenPET system set up for one detector module readout. The OpenPET hardware consists of DIBs, detector boards (DB), support boards (SB), and the host PC. DIB output is connected via SCSI-III cable to an OpenPET DB, designed by Terasic (HsinChu, Taiwan) and characterized in [41]. DBs can read in up to 16 single-ended signals (i.e. A-D signals

Figure 3.2.3: The DRS4 board with four SMA input connections.

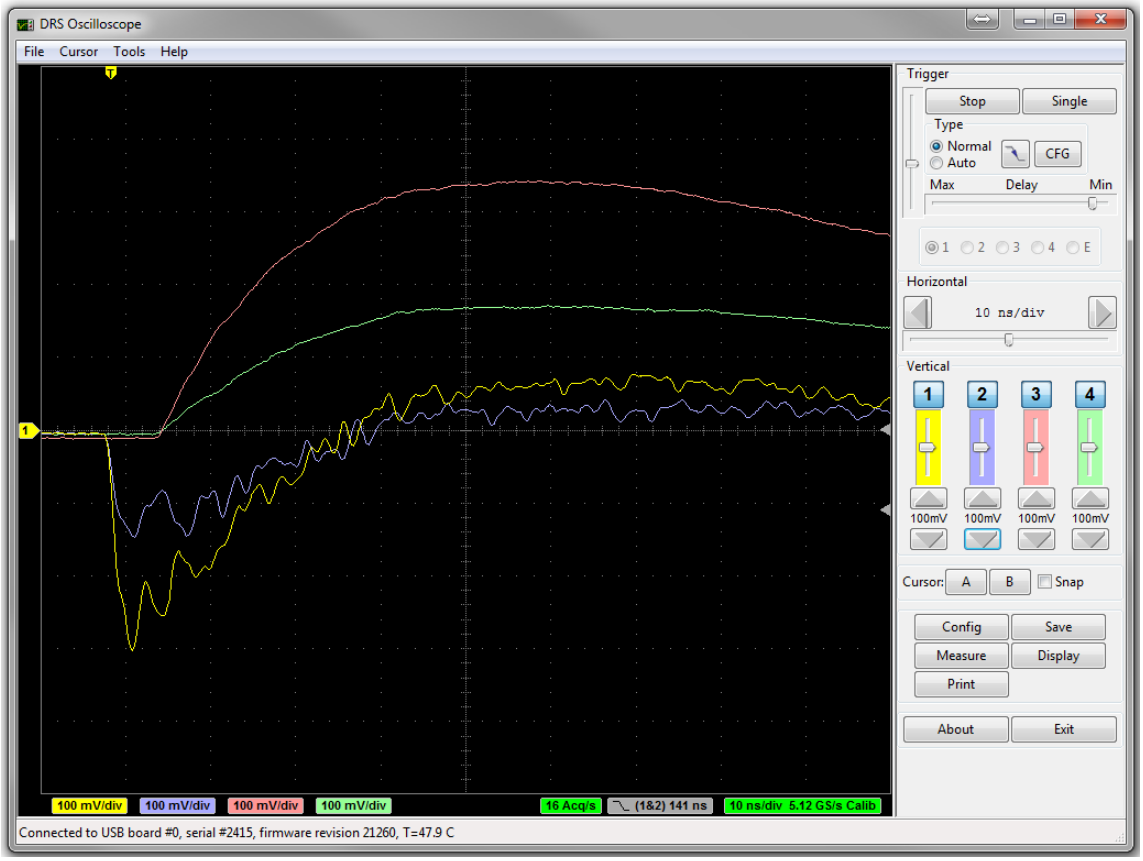

Figure 3.2.4: Screenshot of the DRS4 Oscilloscope software acquiring standard and fast outputs of SensL C-Series single-pixel SiPMs. SiPM 1 and 2 standard outputs are red and green, respectively, while fast outputs are yellow and blue, respectively.

× 4 readout boards) which are split into energy and timing paths and processed by the DB FPGA (see Figure 3.2.5b). Time channels are fed into a fast comparator for triggering, then a time-to-digital converter (TDC) clock with 400 MHz (i.e. 2.5 ns granularity) for timestamp calculation. Energy channels are fed into comparators to trigger ADC capture, which samples the input energy signal at 40 MHz. By default, the ADC takes 32 samples per trigger (32 samples × 1/40 Msamples/s = 800 ns). Downstream, the ADC capture peak is found and baselined. Energy and timestamps are compiled into 64-bit data packets. In the SB, events scanned by the input/output (I/O) FPGA that are valid are sent to the main FPGA, where it is stored in a ∼2MB memory buffer. When the buffer is full, events are transferred to the host PC via a USB 2.0 QuickUSB module (Bitwise Systems, Gotela, CA).

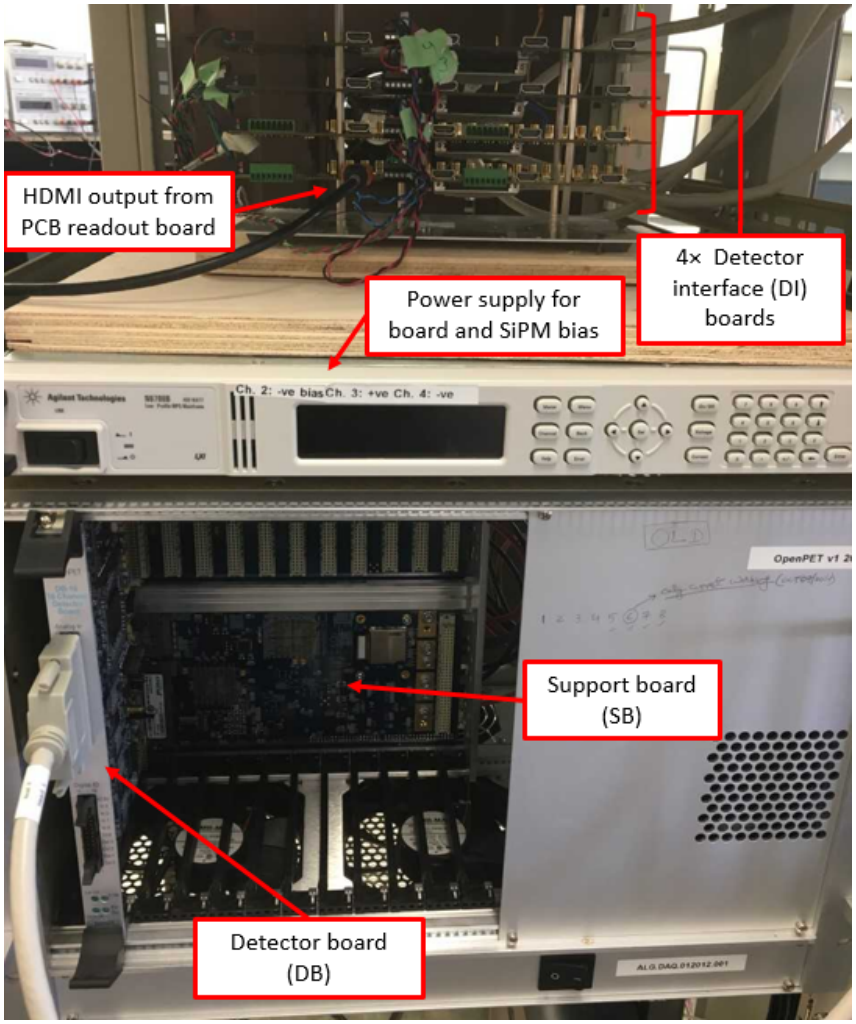

(a) The OpenPET chassis with one (of up to eight) detector board connected to the support board. The support board has a QuickUSB module on the backside for host PC transfer.

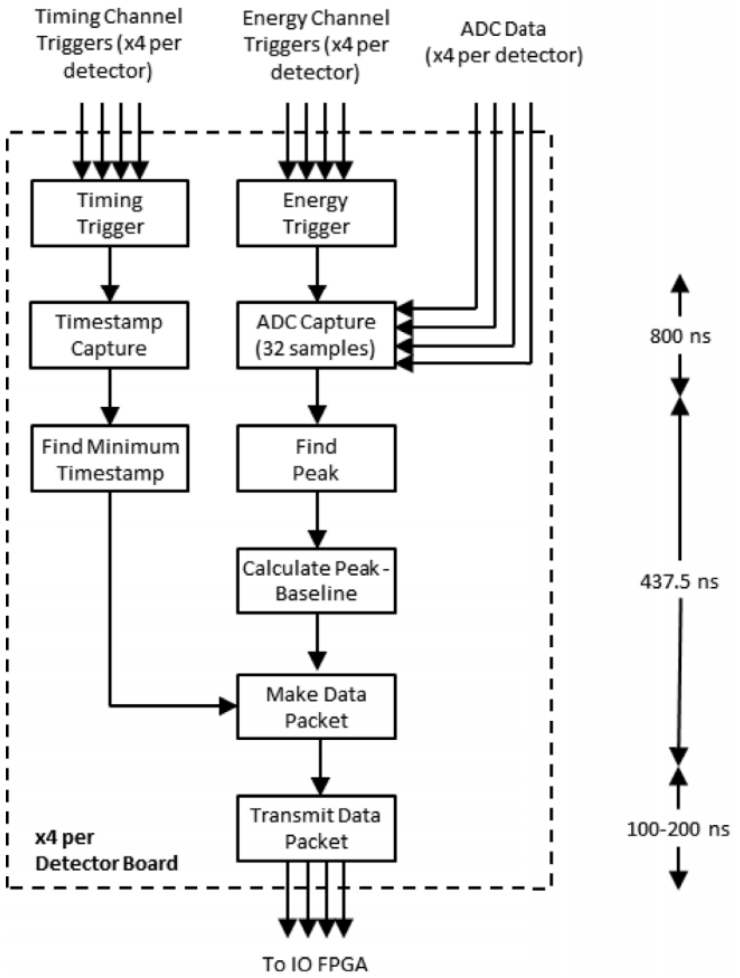

(b) Schematic of DB FPGA signal processing. Reprinted with permission [40] ©2017 IEEE.

Figure 3.2.5

3.3 Data Processing

3.3.1 Software

All singles and coincidence event data were analyzed using in-house developed software written in MATLAB 2016a (Mathworks, Natick, MA). List mode data (both singles and coincidences) from NIM and OpenPET acquisitions were processed in a pre-existing program 'PETDetectorAnalysis.m' (with several modifications made throughout this work). Pre-existing MATLAB scripts were used to compile waveform captures from DRS4 into data sets, and additional MATLAB software 'DRS4.m' was developed to further process the waveforms. In general, the 'PETDetectorAnalysis.m' and 'DRS4.m' programs were used to generate flood, energy, and time histograms which are described in this section.

3.3.2 Flood histograms

Data sets with array detectors contain digitized multiplexed signals A-D. Positional x- and y- coordinates are calculated using simple Anger logic (i.e. using Equations 3.2 & 3.3). *Flood histograms* (also called 'flood images' or 'flood maps') are two-dimensional histograms of the x- and y-coordinates of a data set. Figure 3.3.1 shows two detector setups and their corresponding flood histograms. The left column is an example of a one-to-one coupling setup where each LYSO:Ce pixel nearly matches the SiPM pixel pitch. The flood histogram shows that all 32 LYSO:Ce crystals are clearly separated or *resolved*. The right column utilizes a densely-pixelated DLO array with a 26×13 bottom layer array of 1.28×1.28×6 mm^3 crystals and a half crystal pitch offset 25×12 top layer of 1.28×1.28×4 mm^3 crystals. The DLO flood histogram shows good crystal resolvability except for some blurring at the edges and corners. Middle crystals spread light evenly through the coupling/diffuser layer

to the SiPM pixels, while edge/corner crystals do not spread light evenly due to their close proximity to an optical boundary.

Once flood histograms are generated, crystals are individually segmented by drawing a border surrounding the Gaussian centre of each crystal (Figure 3.3.2). Crystal look-up tables (CLUTs) are generated from segmented flood histograms. Downstream in the data processing chain, 'crystal 1' events correspond to all events that fall inside the border surrounding point 1. Crystal segmentation is done because there are inter-crystal discrepancies in energy and timing performance due to differences in optical coupling quality, SiPM pixel gain, etc.

3.3.3 Energy resolution

Once crystal flood histograms are segmented, crystal-by-crystal energy spectra can be generated. Event energies are calculated as the sum of A-D multiplexed outputs (Equation 3.1) then binned into *energy histograms*. An example of energy processing in the PETDetector-Analysis.m software is shown in Figure 3.3.3.

Figure 3.3.4 shows a generic energy histogram that was generated using a ^{22}Na source irradiating a PMT coupled with a 1×1×1 cm^3 LYSO:Ce pixel. The abscissa is 14-bit ADC voltage while the ordinate is the number of counts within each discrete ADC voltage bin. There is clearly a peak in the spectrum at ∼449 mV, which corresponds to scintillation events resulting from photoelectric absorption of 511 keV annihilation photons. This peak is referred to as the *photopeak*. Events in the range of roughly 100 - 350 mV are mostly Compton scattered events of 511 keV annihilation photons, with a relatively minor contribution from 202 & 307 keV γ-ray emissions of naturally-radioactive ^{176}Lu.

Ideally, all annihilation photons absorbed would produce a signal equivalent to exactly 511 keV. The corresponding energy histogram would appear to have a delta function at

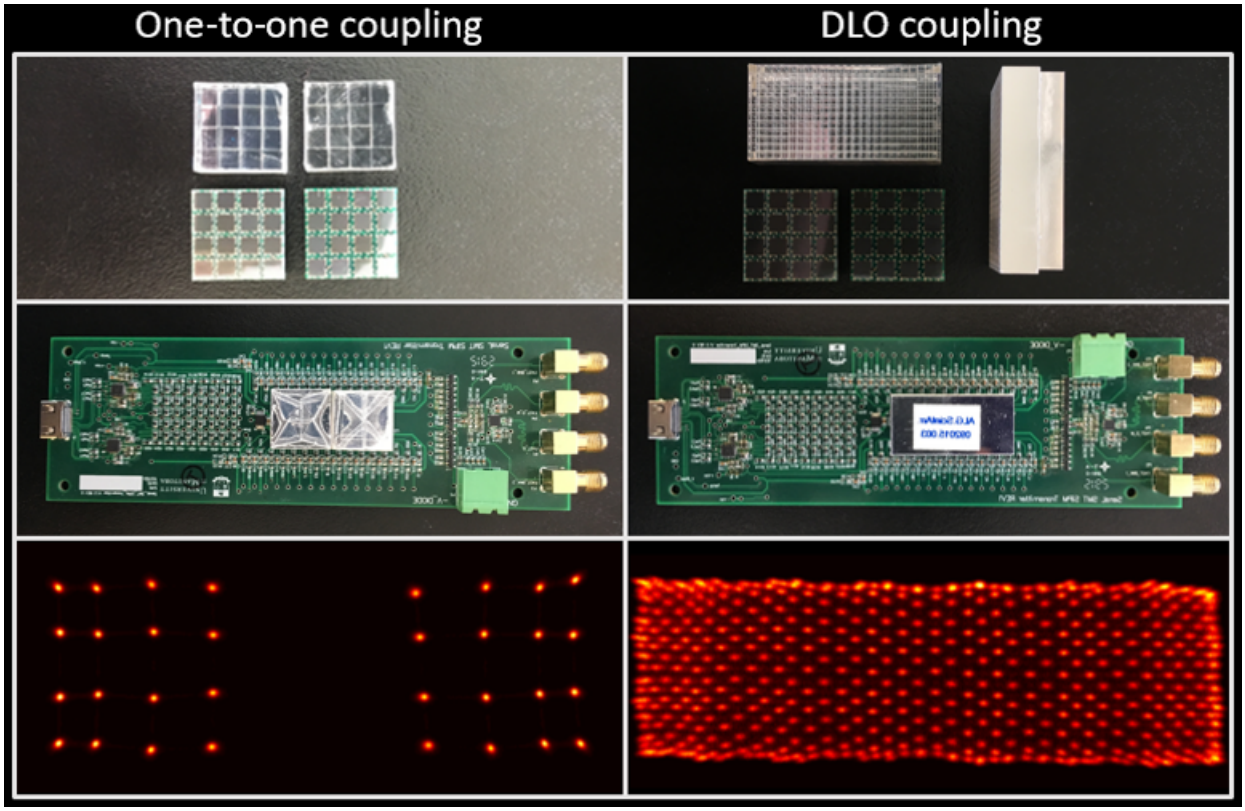

Figure 3.3.1: Detector setups and flood histograms for one-to-one (left) and DLO (right) scintillator coupling. SiPM-C and LYSO:Ce scintillators (top), detector/scintillators coupled and input to a detector readout board (centre), and the corresponding flood histogram (bottom).

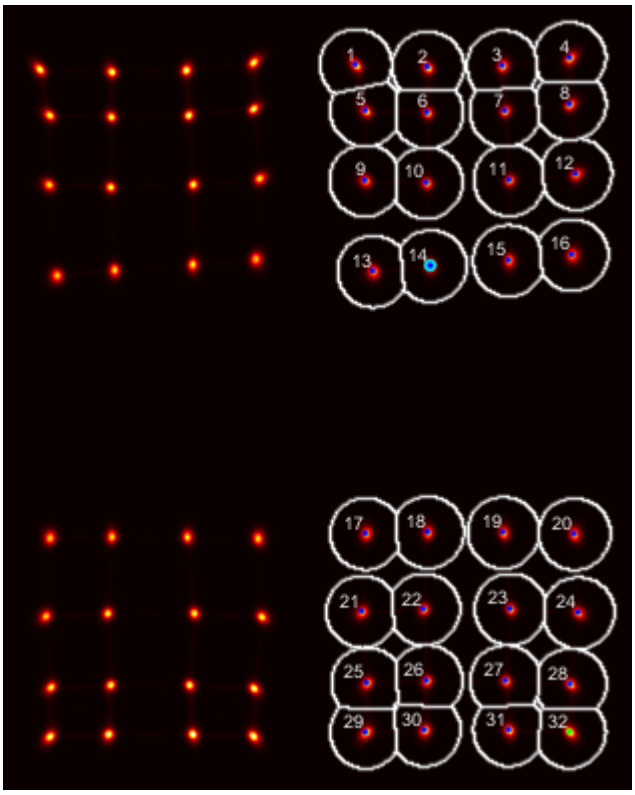

Figure 3.3.2: Flood histogram of the one-to-one coupled LYSO:Ce/SiPM-C detector readout (left), and segmented flood histogram with borders surrounding each crystal (right).

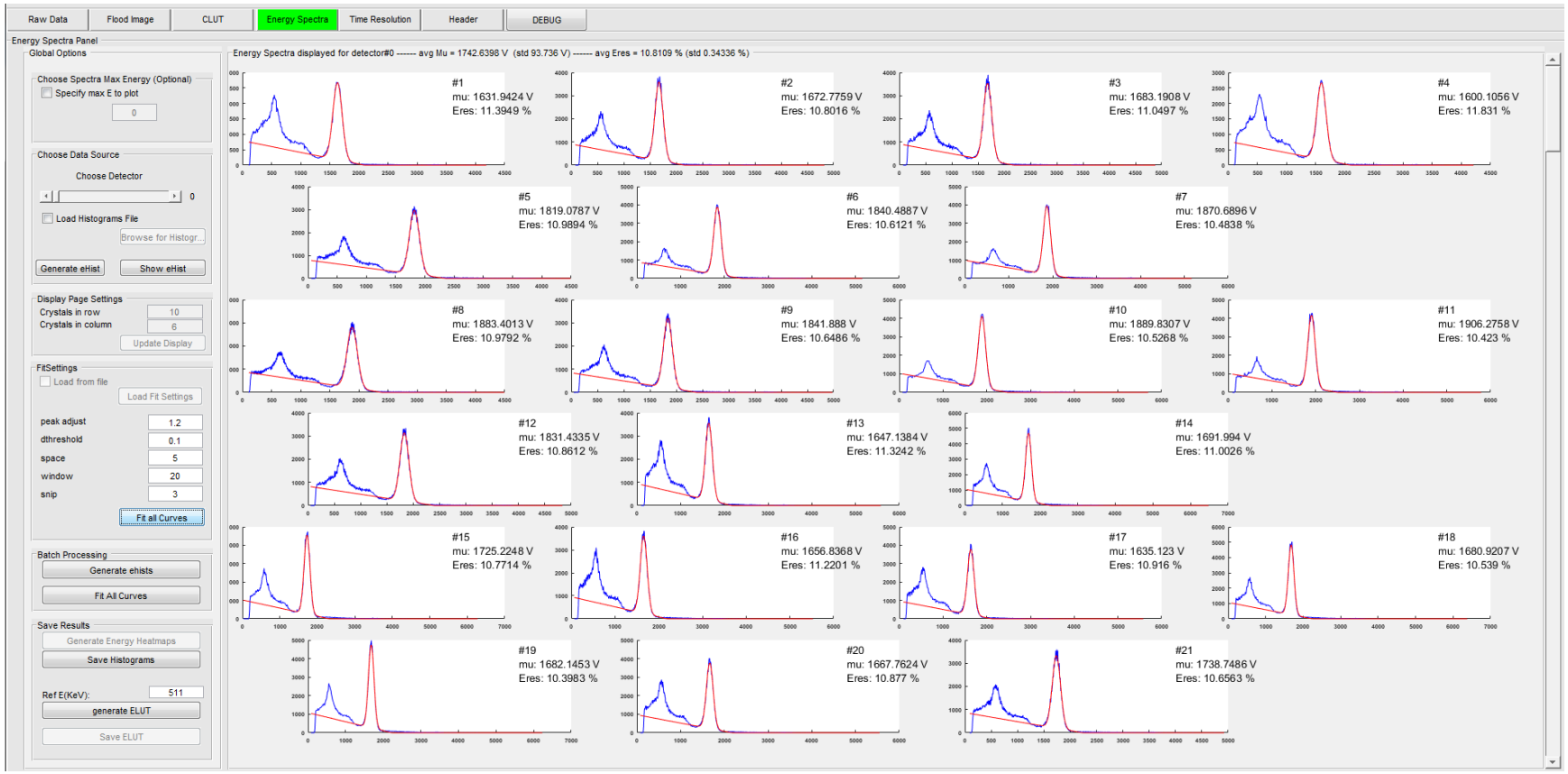

Figure 3.3.3: Screenshot of PETDetectorAnalysis.m software generating crystal-by-crystal energy spectra for the one-to-one coupled LYSO:Ce/SiPM:Ce detector readout. Each spectrum is fit with a Gaussian-plus-line function with user-defined fitting parameters input in the 'FitSettings' panel. Photopeak amplitude and energy resolution are displayed on each histogram, while crystal-averaged photopeak amplitude and energy resolution are displayed at the top of the spectra panel. ELUTs can be generated in the 'Save Results' panel for further data processing.

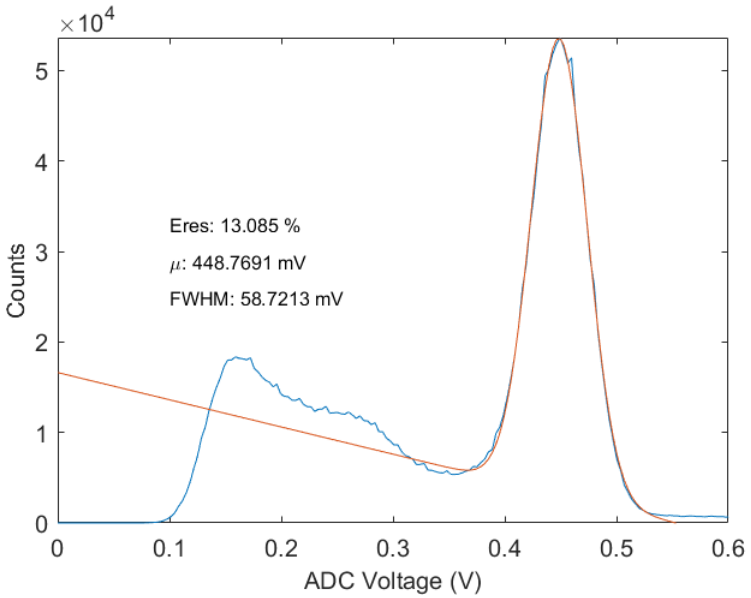

Figure 3.3.4: Energy histogram (blue) of a PMT coupled with a 1×1×1 cm^3 LYSO:Ce pixel. The data were fit with a Gaussian-plus-line function (red) to determine the photopeak amplitude and energy resolution of the spectrum.

the photopeak. Instead, photopeak events produce a spectrum that can be modelled by a Guassian distribution. Variations in photopeak event energy are the result of statistical fluctuations in optical photon generation, in the number of optical photons that reach the photodetector (i.e. that aren't absorbed at reflector and optical coupling boundaries or within the scintillator itself), in the PDE of the photodetector, and in electronic noise. Energy histogram photopeaks are typically modelled by a Gaussian distribution f_G:

$$f_G(x) = Ae^{\frac{(x-\mu)^2}{2\sigma^2}} \tag{3.4}$$

where A is the amplitude (i.e. height), μ is the mean, and σ is the standard deviation of the distribution. *Photopeak amplitude* or photopeak position is simply μ. Assuming the energy spectra is linear with energy, the x-axis can be converted from ADC voltage to energy

by multiplying by a calibration factor E_{cal}:

$$E_{cal} = \frac{511keV}{\mu} \tag{3.5}$$

Energy spectra calibration is often skipped in PET since it should be obvious (unless large errors are present) that the photopeak corresponds to the 511 keV annihilation photons. Quality of the energy spectra is quantified by the full width at half maximum (FWHM) *energy resolution* E_{res}:

$$FWHM = 2\sqrt{2\ ln2}\ \sigma \tag{3.6}$$

$$\approx 2.235\ \sigma \tag{3.7}$$

$$E_{res} = \frac{FWHM}{\mu} \times 100\% \tag{3.8}$$

$$= \frac{2.235\ \sigma}{\mu} \times 100\% \tag{3.9}$$

Energy resolution is a measure of how well the photopeak can be resolved with respect to the rest of the spectrum. Energy spectra with high μ and low σ have low E_{res} values, which means better separation between photopeak events and Compton events. Energy resolution is important when defining an energy window to select photopeak events and remove scattered events. A user-defined energy window is imposed on the spectra that can be specified in absolute terms (e.g. 400 keV - 650 keV using E_{cal}) or in relative terms (e.g. $\pm\ 2\sigma$). Events inside the window are kept while events outside the specified window are removed. Photopeak and scattered events overlap if energy resolution is poor, which may have consequences: either a significant portion of scattered events fall within the energy window, or the energy window must be made sufficiently small to cut out scattered events but will also cut out a significant portion of photopeak events.

In the example energy spectrum shown in Figure 3.3.4, clearly there is an overlap of scattered and photopeak events in the 0.35 - 0.40 V range. Scattered events may be crudely accounted for by fitting the end of the Compton shoulder with a line. The red line in Figure 3.3.4 is a Gaussian-plus-line fit $f_{G\&L}$:

$$f_{G\&L}(x) = f_G(x) + f_{line}(x) \tag{3.10}$$

$$= Ae^{\frac{(x-\mu)^2}{2\sigma^2}} + mx + b \tag{3.11}$$

where m is the slope and b is the y-intercept of the line. The Gaussian-plus-line function fits the photopeak better than a Gaussian alone, leading to better energy window definition and a more accurate measure of μ and σ. The Compton shoulder may also be crudely fit with a Gaussian function. The double Gaussian fitting function is simply:

$$f_{2G}(x) = f_{G,p}(x) + f_{G,s}(x) \tag{3.12}$$

$$= A_p e^{\frac{(x-\mu_p)^2}{2\sigma_p^2}} + A_s e^{\frac{(x-\mu_s)^2}{2\sigma_s^2}} \tag{3.13}$$

where $f_{G,p}(x)$ and $f_{G,s}(x)$ are the photopeak and scatter Gaussian functions, respectively. For both the Gaussian-plus-line fitting and double Gaussian fitting, photopeak amplitude and energy resolution are determined from the μ and σ parameters of the photopeak Gaussian only.

Energy look-up tables (ELUTs) are generated from the fitted energy spectra. ELUTs contain per-crystal energy fitting data for energy window selection in downstream processing.

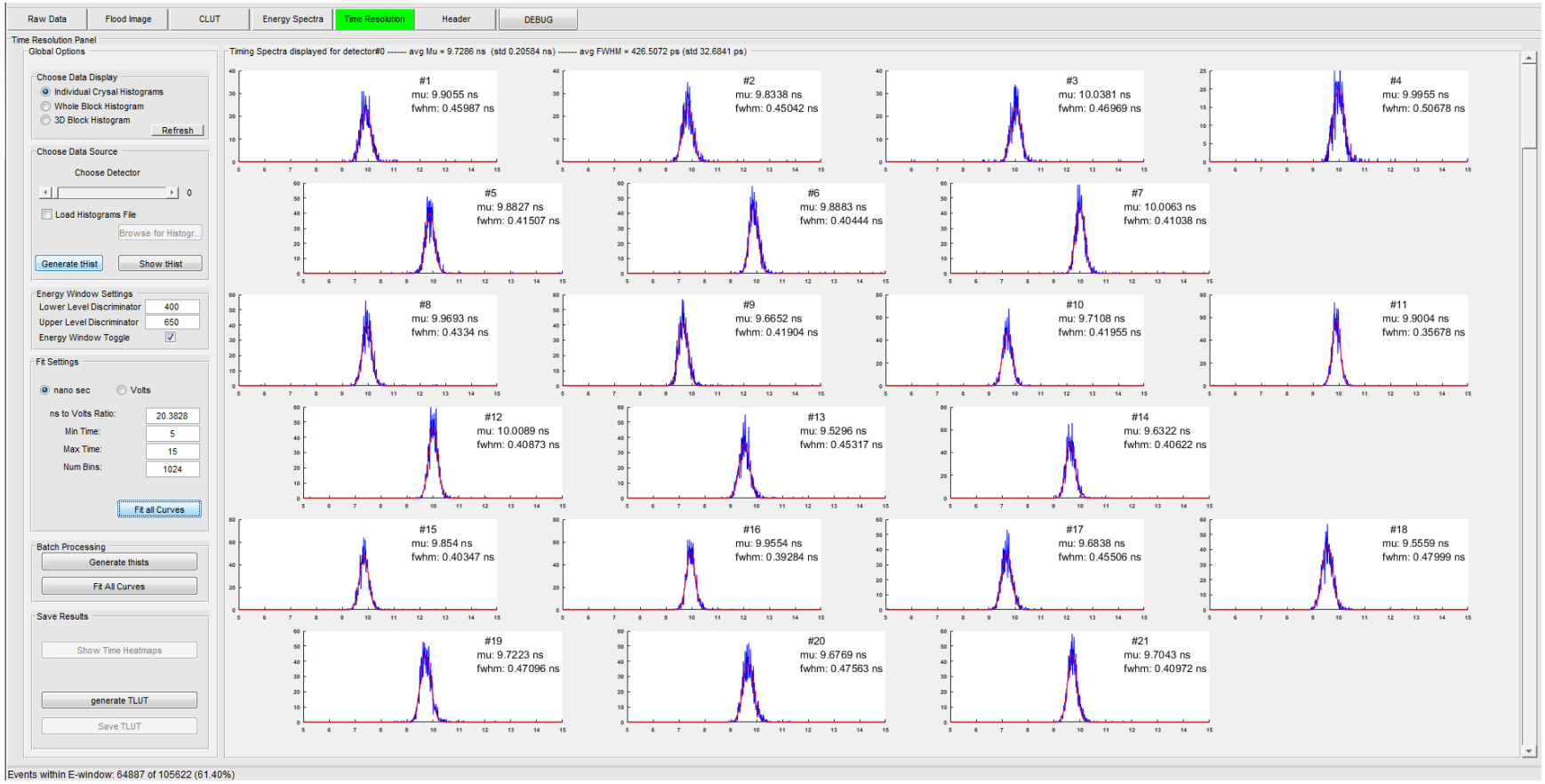

Figure 3.3.5: Screenshot of PETDetectorAnalysis.m software generating crystal-by-crystal time spectra for the one-to-one coupled LYSO:Ce/SiPM-C detector readout. Photopeak events were selected by imposing a 400-650 keV energy window. Each time spectrum is fit with a Gaussian function. Time peak position and timing resolution is displayed on each histogram, while crystal-averaged time peak position and timing resolution are displayed at the top of the spectra panel.

3.3.4 Coincidence time resolution

Data acquisitions in coincidence are processed further to extract timing information. After defining an energy window, photon arrival time differences Δt are binned into *time histograms*. Figure 3.3.5 is a 'PETDetectorAnalysis.m' screenshot of timing spectra for the one-to-one coupled LYSO:Ce/SiPM-C detector readout in coincidence with a single SiPM-J SMA pixel. Each time spectrum is fit with a simple Gaussian distribution (Equation 3.12). Time peak position is the mean of the Gaussian distribution μ. *Time dispersion* can be estimated by the standard deviation of time peak positions. The *coincidence time resolution* (CTR) is defined as the FWHM of the Gaussian fit:

$$CTR = FWHM \tag{3.14}$$

$$\approx 2.235\ \sigma \tag{3.15}$$

If photon arrival time differences for all crystals were histogrammed for the entire array, the resulting time histogram would be artificially broadened due to the presence of time dispersion. This can simply be corrected by shifting each histogram to a common centre, for example, by subtracting the abscissa of each histogram by the mean of their respective Gaussian distribution in order to centre each distribution at zero. Then, time histograms may be added and the total array CTR can be calculated. However, in this work, CTR for array detectors was calculated as the crystal-averaged CTR. Both dispersion-corrected and crystal-averaged CTR yield similar results.

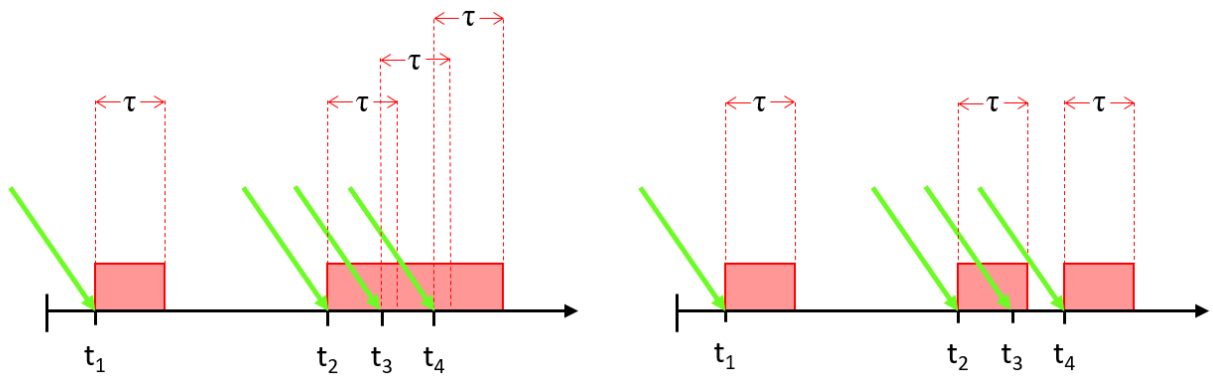

(a) (b)

Figure 3.3.6: Illustration of the paralyzable and non-paralyzable dead time models for a detector with fixed dead time τ. Four radiation events (green arrows) occur at times t_1 - t_4. Detector dead time is designated in red. In the paralyzable model (a), the arrival of an event at t_3 extends the dead time initiated by the event at t_2. Events at t_2, t_3, and t_4 are recorded as one event. In the non-paralyzable model (b), the arrival of an event at t_3 does not initiate a trigger and therefore is lost. Events at t_2 and t_4 are processed in the same manner in the presence or absense of an event at t_3.

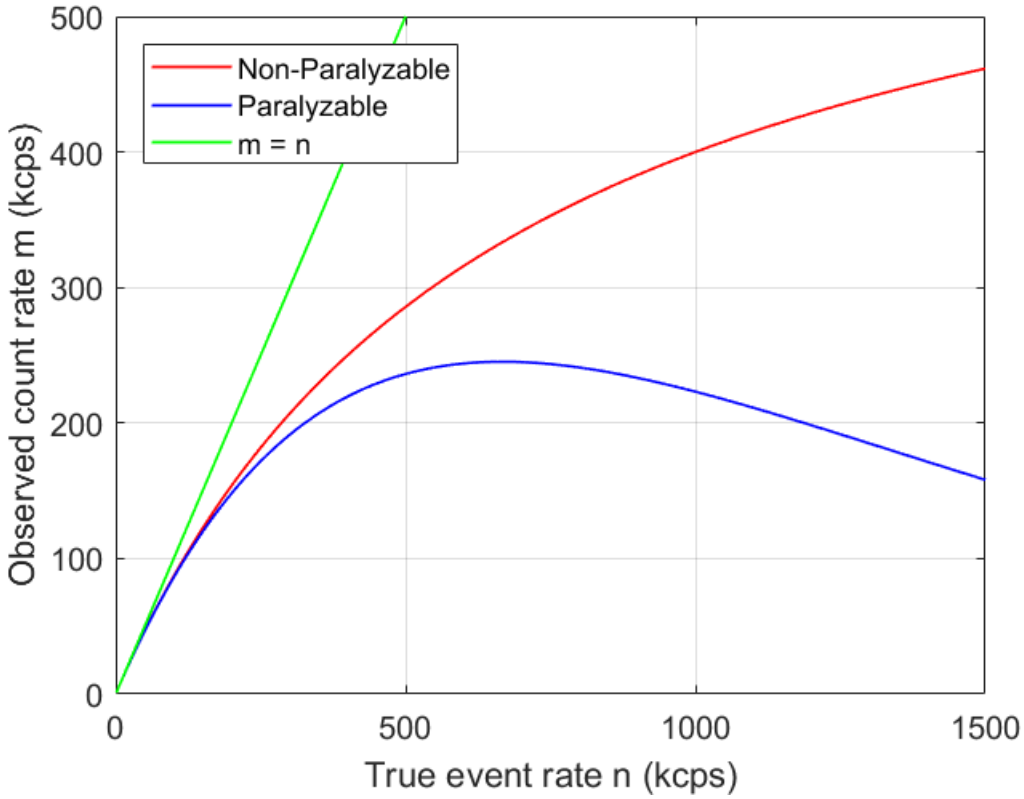

Figure 3.3.7: Dead time curve for a detector with 1.5 μs dead time. The non-paralyzable model (Equation 3.17, red line) continuously rises but approaches a plateau while the paralyzable model (Equation 3.16, blue line) reaches a peak then decreases as n increases. The green line represents zero dead time where all true events are observed regardless of the count rate.

3.3.5 Count rate and dead time

Count rate performance of preclinical PET inserts is important in applications with high activity levels (i.e. high concentrations of radioactive tracers). The data acquisition system must be able to process each event quickly and efficiently. Events are lost if they occur while preceeding events are still being processed by the PET system. *Dead time* is the minimum amount of time between the start of one radiation event to the point where the PET system is ready to process another event. There are generally two models that describe dead time behaviour, *paralyzable* and *non-paralyzable* dead time. These models are described in [25].

For systems exhibiting paralyzable dead time, the arrival of each event will render the detector 'dead' for time τ regardless of when the event occurs. Multiple events that occur within τ result in a pile up of dead time. In the illustration in Figure 3.3.6a, the arrival of an event at t_3 extends the dead time initiated by the event at t_2, and as a consequence the events at t_2, t_3, and t_4 are all 'blended' together as one event.

For systems exhibiting non-paralyzable dead time, the processing of an event cannot start unless the preceeding event is completely processed. This model assumes that events that occur within the dead time τ have no effect on the system at all. In the illustration in Figure 3.3.6b, events occurring at times t_1, t_2, and t_4 are processed normally, and the event at t_3 is completely ignored.

Both models can be described numerically. For a detector dead time τ and true event rate n, the observed count rate m according to the paralyzable model is [42]:

$$m = ne^{n\tau} \tag{3.16}$$

And according to the non-paralyzable model [42]:

$$m = \frac{n}{1 + n\tau} \tag{3.17}$$

$$= \frac{gA}{1 + gA\tau} \tag{3.18}$$

where the true count rate n is assumed to be a function of activity A multiplied by a (constant) efficiency factor g. The paralyzable and non-paralyzable models are plotted in Figure 3.3.7 for a detector dead time of 1.5 μs. As count rate is increased, the observed count rate deviates more from the true event rate. In general, event loss is greater for the paralyzable model due to the additive nature of event dead times.

Whereas digital systems typically exhibit non-paralyzable behaviour, photodetectors and other analog systems typically exhibit paralyzable behaviour. Every event produces an output pulse which causes the acquisition system to start processing the event once the output pulse exceeds the threshold setting. The output pulse must decay below the threshold

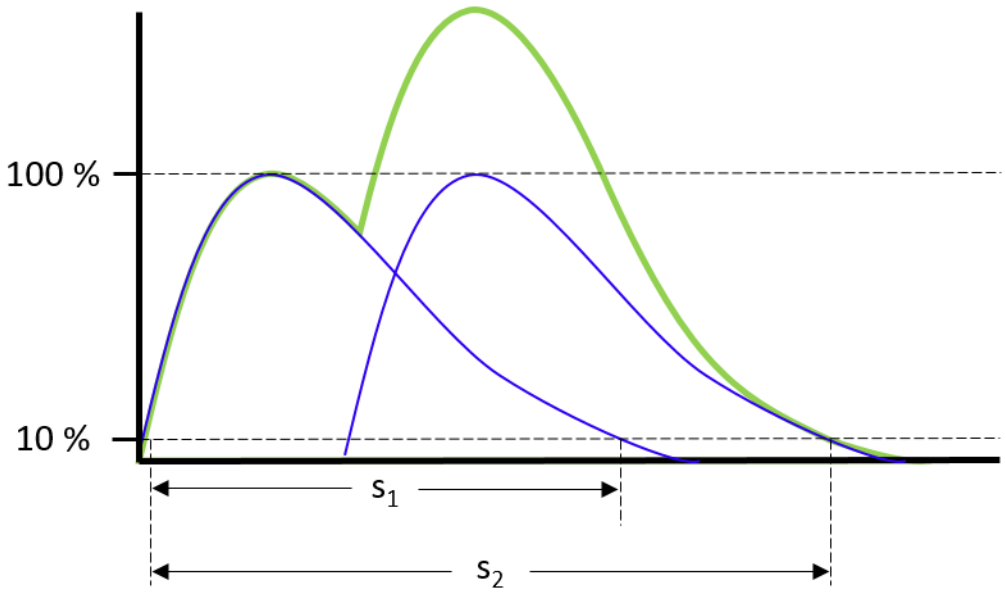

Figure 3.3.8: Illustration of signal pileup. The signal duration (i.e. time above 10 % signal amplitude) is s_1 for a single output pulse (blue). With the arrival of another event, the two output pulses overlap and add to form a pileup pulse (green) with duration s_2.

before another event can be triggered. A second radiation event may occur while the output pulse amplitude of the previous event still exceeds the threshold level. In this case, a trigger is not produced and the acquisition system does not process the second event. The phenomenon of overlapping signals due to two close-in-time events is known as *pileup* and is illustrated in Figure 3.3.8.

Pileup is generally only a concern at high count rates, and it depends on the *signal duration* of the photodetector. In this work, signal duration is defined as the time an output pulse is above 10 % amplitude. The detector modules in the first-generation PET insert had a relatively long signal duration of >1.5 μs [40]. Signal duration depends on the *time constant* or recovery time ($\tau_{RC} = RC$) of the detector. According to SensL documentation, the recovery time of a SiPM microcell is [43]:

$$\tau_{RC} = C_d(R_q + R_s N) \tag{3.19}$$

where C_d is the effective capacitance of the microcell, R_q is the resistance of the quenching resistor in series, R_s is the series resistance of the SiPM pixel, and N is the number of microcells in the pixel. Effective capacitance C_d depends on microcell size, such that larger area microcells have longer recovery times. Photodetectors exhibit low signal duration when they have a low capacitance, low microcell number, and small area per microcell. However, low microcell number and small microcell area is not ideal since the PDE and photon statistics would suffer. A compromise must be made between PDE and signal duration when choosing a photodetector.

PET acquisition systems typically exhibit hybrid dead time behaviour, where a 'block' of detectors is paralyzable and downstream processing electronics are non-paralyzable (for example, see [44]). The first-generation PET insert has been characterized with a paralyzable dead time of ∼1.3 μs due to the performance of the SensL B-Series SiPMs with the first-generation detector board readout, as well as a non-paralyzable dead time of ∼1.8 μs due

to the event processing time of the OpenPET system (see Figure 3.2.5) [40].

Chapter 4

Optical Coupling Optimization

The contents of this section is from a peer-reviewed scientific research paper published in: *Physics in Medicine and Biology, 63(5):05NT02(8pp), 2018.* doi.org/10.1088/1361-6560/aaa815

Comparison of acrylic polymer adhesive tapes and silicone optical grease in light sharing detectors for positron emission tomography

Devin J Van Elburg[1], Scott D Noble[2], Simone Hagey[2], Andrew L Goertzen[1,3]

[1] Department of Physics and Astronomy, University of Manitoba, Winnipeg, MB R3T 2N2, Canada

[2] College of Engineering, University of Saskatchewan, Saskatoon, SK S7N 5A9, Canada

[3] Department of Radiology, University of Manitoba, Winnipeg, MB R3E 3P4, Canada

4.1 Abstract

Optical coupling is an important factor in detector design as it improves optical photon transmission by mitigating internal reflections at light-sharing boundaries. In this work we compare optical coupling materials, namely double-sided acrylic polymer tapes and silicone optical grease (SiG), in the context of positron emission tomography. Four double-sided tapes from 3M of varying thicknesses (0.229 mm - 1.016 mm) and adhesive materials ('100MP', 'A100', and 'GPA') were characterized with spectrophotometer measurements as well as photopeak amplitude and energy resolution measurements using lutetium-yttrium oxy-orthosilicate (LYSO) coupled to photomultiplier tubes (PMT) or silicon photomultipliers (SiPMs). Transmission spectra from the spectrophotometer showed over 80% transmission for all tapes at 420 nm and above, with 89.6% and 88.8% transmission for the 0.508 mm and 1.016 mm thick GPA tapes, respectively, at 420 nm. Measurements with single-pixel LYSO-PMT and 4 $\times$ 4 array (one-to-one coupled) LYSO-SiPM setups determined that SiG had the greatest photopeak amplitude, with tapes showing 2.1% - 14.8% reduction in photopeak amplitude with respect to SiG. Energy resolution changed by less than 4% on a relative basis between tapes and SiG with PMT measurements, however for the SiPM array measurements the energy resolution improved from 15.6% $\pm$ 2.7% full-width at half-maximum to 11.4% $\pm$ 1.2% for SiG and 1 mm GPA, respectively. Data acquired with dual-layer offset LYSO arrays (light sharing detector designs) demonstrated that a detector coupled with 1 mm thick GPA tape produced equivalent detector flood histograms to those from a design coupled with SiG and a 1 mm thick glass lightguide. No significant degradation in photopeak amplitude and energy resolution was observed over five months of measurements, indicating the tapes maintain their coupling integrity over several months. Though minimal photopeak amplitude degradation compared to SiG occurs, double-sided tapes are convenient alternatives for optical coupling materials since they diffuse light intrinsically, acting as a light guide, offer mechanical support and durability, are easily applied and removed

from scintillators/photodetectors, and are relatively inexpensive and readily available.

4.2 Introduction

Optical coupling between the scintillator and photosensor is important to consider when constructing a PET detector. Optical photons travelling from a low refractive index medium to a high refractive index medium are likely to be reflected or absorbed, depending on the angle of incidence upon the interface boundary and the ratio of refractive indices. The critical angle, derived from Snell's law, is the maximum angle with respect to the normal axes of the interface in which photons will transmit through the interface:

$$\theta_C = sin^{-1}(\frac{n_2}{n_1}) \tag{4.1}$$

where n_1 and n_2 are the refractive indices of the entrance and exit media, respectively. The refractive index of LYSO:Ce and of the entrance window of the SensL SiPMs used in this work are $n_{LYSO} = 1.82$ and $n_{SiPM} = 1.5$, respectively, for 420 nm photons. If no optical coupling medium is present, an air boundary exists ($n_{air} = 1$). Therefore, a high degree of reflectance is expected as optical photons reach the air-SiPM interface. Optical coupling materials are often refractive-index-matched with the scintillator and SiPM to optimize transmission of optical photons. Other consideration in choosing optical coupling materials are ease of application and removal, and mechanical stability.

One of the most common optical coupling materials used is silicone optical grease (SiG) (e.g. [45, 46, 47]) which has a a refractive index of $n_{SiG} = 1.5$. Scintillators coupled with SiG may migrate from their original positions throughout data acquisitions unless additional mechanical support is supplied. Several groups use materials that are media-matched and mechanically stable, such as thermally reversible adhesives like Meltmount^{TM} (e.g. [48,

Table 4.3.1: Summary of optical coupling materials investigated.

Material	3M product #	Thickness (mm)
GPA	4910	1.016
A100	4658F	0.787
GPA	4905	0.508
100MP	F9469PC	0.229
SiG	-	$\sim 0.150^a$

[a] e.g. Modelled as 150 μm here [56]

49, 50, 51, 52]) or permanent silicone-based adhesives such as Dow Corning products (e.g. [53, 54, 55]). UV-curing glues or epoxies may also be used to provide rigid mounting, however these are typically non-reversible bonds.

An alternate approach is to use optically transparent double-sided tapes. Unlike the aforementioned coupling materials, double-sided tapes are mechanically stable, easily applied/removed optical coupling materials. Ease of application/removal is especially convenient in laboratory settings where scintillators/photodetectors are swapped repeatedly, and the use of tapes do not require any thermal treatments or UV-curing. To our knowledge, though we (anecdotally) recognize that other groups may be using double-sided tapes, a systematic comparison of tapes versus conventional optical coupling material in the context of PET has not been done.

4.3 Materials

Four acrylic polymer tapes from 3M (Saint Paul, MN) were selected for study and are summarized in Table 4.3.1. Two VHB class tapes, 1.016 mm and 0.508 mm thick, were a general purpose acrylic (GPA) adhesive deposited on a foam carrier. Another VHB class tape, 0.229 mm thick, was a 100MP acrylic adhesive without a carrier/backing. The fourth tape was 0.787 mm thick Adhesive 100 (A100) material on an acrylic foam carrier. These tapes were selected because of their off-the-shelf availability and transparent appearance, however it should be noted they are not specifically designed for optical purposes. For

Figure 4.3.1: (Seven different types of acrylic polymer double-sided tapes from 3M were ordered. Four of these tapes were used to investigate their optical coupling performance.

comparison, a standard SiG was used: Visilox V-788 silicone optical compound (Rhone-Poulenc Silicones VSI, Troy, NY).

4.4 Methods

4.4.1 Spectrophotometer measurements

Optical transparency was evaluated with spectrophotometer measurements. Simple cardboard holders were cut each with a 12×17 mm^2 aperature. Four samples of each tape (for a total of 16 samples) were mounted onto the cardboard holders, then the holders were secured to the solid sample holder of a Cary 5G dual-beam spectrophotometer (Agilent, Santa Clara, CA). The spectrophotometer operated in transmission mode with air in the reference beam

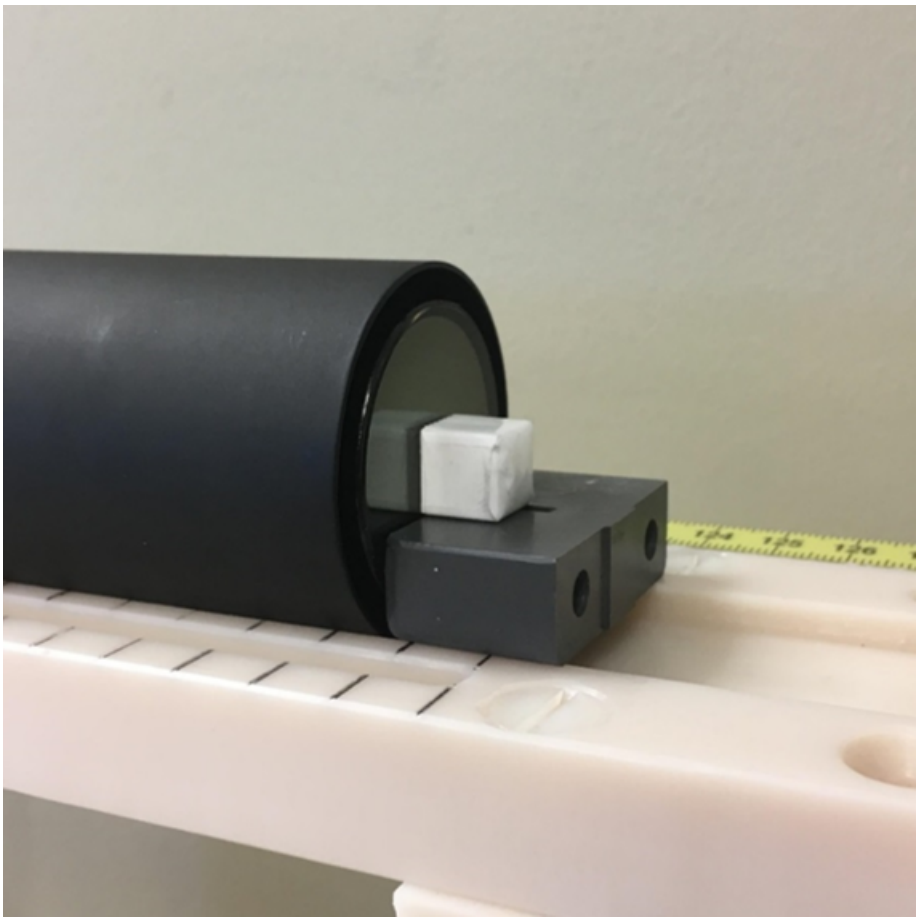

Figure 4.4.1: A single Teflon-wrapped LYSO:Ce crystal coupled with SiG to a PMT. The PMT was secured to a mount with an LYSO:Ce support.

path. For each sample, transmission data were obtained from 300-800 nm in increments of 1 nm and with a spectral band width of 2 nm. This range was chosen because it covers the wavelength of maximum emission of LYSO:Ce and the maximum PDE of SensL SiPMs (420 nm), as well as the maximum PDE for Hamamatsu MPPCs (450 nm). SiG transmission data were not obtained since the mounting stage inhibited SiG testing without transmission through support media.

4.4.2 PMT - single LYSO:Ce crystal

A Hamamatsu H3178-51 PMT was coupled with a single Teflon-wrapped $1\times1\times1$ cm^3 LYSO:Ce crystal (Proteus Inc., Chagrin Falls, OH) using the five materials in Table 4.3.1. The PMT

was biased to 1500 V using an ORTEC 556H high voltage power supply. The apparatus was placed in a light-tight box. Output was processed using standard NIM electronics in singles mode (i.e. no timing information was acquired). The PMT output signal was fed into the CAEN Model N845 LED with a relatively high 250 mV trigger threshold to ensure a large portion of events captured were photopeak events. Once triggered, the signal was digitized using a National Instruments PCI-6133 data acquisition card with National Instruments LABWindows/CVI software. Data processing was done using in-house software developed in MATLAB 2016a. Energy spectra were generated and fit with a Gaussian-plus-line function (Eq. 3.11). Photopeak amplitude (E_μ) and energy resolution (E_{res}) were obtained in order to quantify light losses and optical coupling quality. For each material, 10^6 counts were acquired using a ∼6.1 MBq ^{68}Ge rod source. For these measurements, a single data acquisition for each optical coupling material was deemed sufficient because they will be supplemented with per-crystal averaged SiPM array data.

4.4.3 SiPM array - single-layer 4×4 LYSO:Ce array

A single-layer 4×4 array of 4×4×4 mm^3 LYSO:Ce crystals (Midas Applied Materials Corp., Zhubei City, Taiwan) was constructed in-house. Inter-crystal boundaries were air gaps, while the outer surfaces of the array were glued with 3M ESR on all but the SiPM-coupling face. This array was coupled directly to one 4×4 SiPM-C array (MicroFC-30035-16P-PCB) using the optical coupling materials in Table 4.3.1. Scintillator crystal and SiPM-C pixel pitch was ∼4.0 mm and 4.2 mm, respectively, giving rise to an approximately one-to-one coupling scenario. No lightguide was used. The LYSO:Ce-coupled array, as well as an uncoupled SiPM-C array, were attached to a second-generation readout board. SiPM-C arrays were biased at 29.0 V. The detector readout board was placed in a light-tight box at room temperature. Readout board mini HDMI output was connected to a detector interface board, then the four multiplexed standard outputs to NIM electronics in singles mode. LED

threshold was set to 10 mV. A 1×1×1 cm^3 acrylic cube with an embedded ^{22}Na source (∼1.8 MBq) was placed above the detector. For each coupling material, 1.14×10^6 singles were obtained. Per-crystal averaged E_μ and E_{res} were calculated for the 4×4 coupled array.

4.4.4 SiPM array - DLO 9×9/8×8 LYSO:Ce array

Two SiPM-C arrays (i.e. 8×4 pixel array) were setup and read out with the NIM acquisition system. SiPM-C bias was 29.0 V. Four coupling scenarios were investigated using a DLO LYSO:Ce array (Proteus Inc., Chagrin Falls, OH) which has bottom and top layers of 9×9 (1.41×1.41×6 mm^3 crystals) and 8×8 (1.41×1.41×4 mm^3 crystals) arrays, respectively. In each scenario, the DLO LYSO:Ce array was coupled to one of the SiPM-C arrays. The four coupling scenarios were:

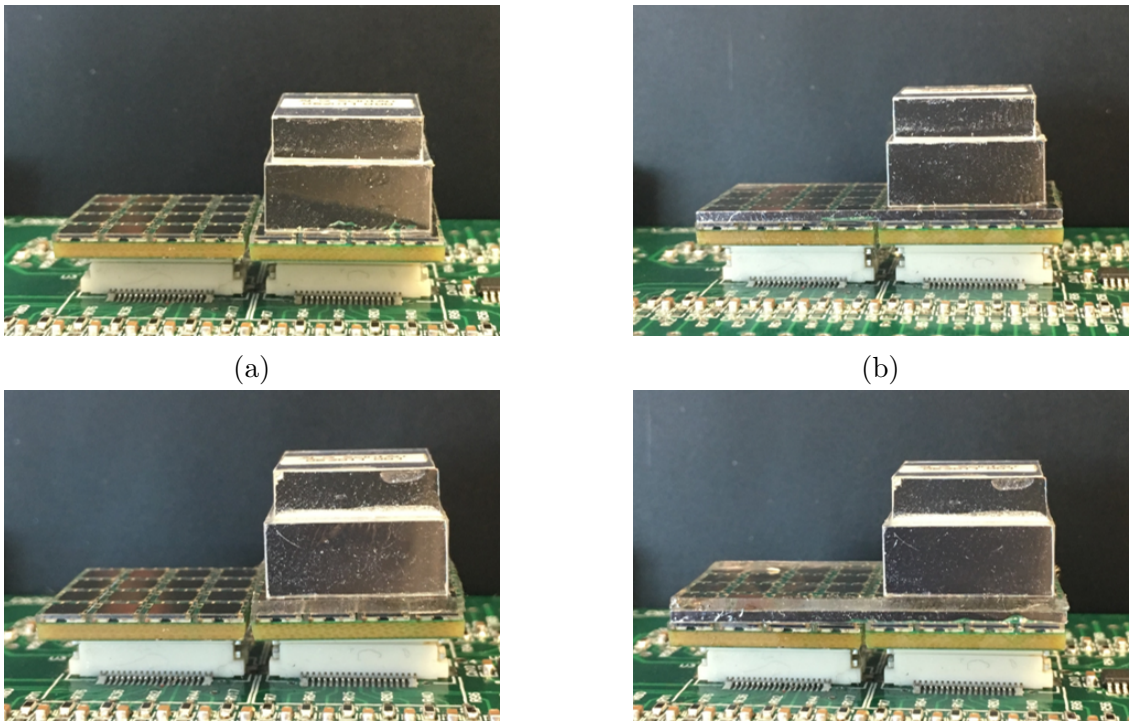

(a) (b) (c) (d)

Figure 4.4.2: (Four coupling scenarios of the 9×9/8×8 DLO LYSO:Ce and SiPM-C arrays: (a) LYSO:Ce - SiG - SiPM-C, (b) LYSO:Ce - SiG - lightguide - SiG - SiPM-C, (c) LYSO:Ce - 1mm GPA - SiPM-C, and (d) LYSO:Ce - 1mm GPA - lightguide - SiG - SiPM-C.

i) LYSO:Ce → SiG → SiPM-C

ii) LYSO:Ce → SiG → 0.96 mm lightguide → SiG → SiPM-C

iii) LYSO:Ce → 1.016 mm GPA tape → SiPM-C

iv) LYSO:Ce → 1.016 mm GPA tape → 0.96 mm lightguide → SiG → SiPM-C

The apparatus was placed in a light-tight box with a ^{68}Ge rod source (∼6.1 MBq) placed on top. For each coupling scenario, 5×10^6 counts were obtained. Coupling scenarios were compared by visual inspection of flood histograms. Photopeak amplitude and energy resolution was obtained for coupling scenarios ii) & iii).

4.4.5 SiPM array - DLO 26×13/25×12 LYSO:Ce array

The same SiPM-C 8×4 array setup and readout was used as described in Section 4.4.4. Both SiPM-C arrays were coupled to a DLO LYSO:Ce array (Proteus Inc.), with bottom and top layers of 26×13 (1.28×1.28×6 mm^3 crystals) and 25×12 (1.28×1.28×4 mm^3 crystals) arrays, respectively. Optical coupling was done with SiG and the 0.96 mm lightguide, as well as with 1.016 mm GPA tape without the lightguide.

ESR grids were constructed with 32 square 3×3 mm^2 holes in an 8×4 array such that the dead space between SiPM-C pixels was covered in ESR. The purpose of the ESR grid was to enhance light collection. For the SiG-lightguide scenario, the ESR grid was glued directly to the lightguide, and the ESR-face was coupled with SiG directly to the SiPM-C arrays. For the 1.016 mm GPA scenario, the grid was placed between the tape-SiPM array interface. Four acquisitions of 1×10^7 events were obtained with the ^{68}Ge rod source:

i) SiG & lightguide,

ii) 1 mm GPA tape,

iii) SiG & lightguide with ESR grid,

iv) 1 mm GPA tape with ESR grid.

Flood histograms for each coupling scenario were constructed for visual comparison.

4.4.6 Tape stability vs time

Optical coupling integrity of the 1.016 mm GPA tape over time was measured using the PMT (Section 4.4.2) and SiPM-9×9/8×8-DLO (Section 4.4.4) setups. The PMT setup was placed in a light-tight box at room temperature. The SiPM-DLO setup was placed in a thermally-insulated light-tight box with temperature maintained at 20.0°C. Using the ^{68}Ge rod source, several acquisitions of 2×10^6 and 5×10^6 counts were obtained for the PMT and SiPM setups, respectively, over the span of five months. Values of E_μ and E_{res} were calculated for each PMT acquisition, while per-crystal averaged values of E_μ and E_{res} were obtained for the central 5×5 bottom layer and central 4×4 top layer crystals for each SiPM-DLO acquisition.

4.5 Results

4.5.1 Spectrophotometer measurements

Spectrophotometer transmission data are shown in Figure 4.5.1a. Optical transmission was over 80% for all tapes for photons between 400-800 nm. For 1.0 mm GPA, 0.5 mm GPA, 100MP, and A100, optical transmission at 420 nm was 88.8%, 89.6%, 85.2%, and 81.6%, respectively. Reproducibility of transmission data is demonstrated in Figure 4.5.1b, where the standard deviation of optical transmission was below 1.05 % for all tapes in the 400-800 nm photon range.

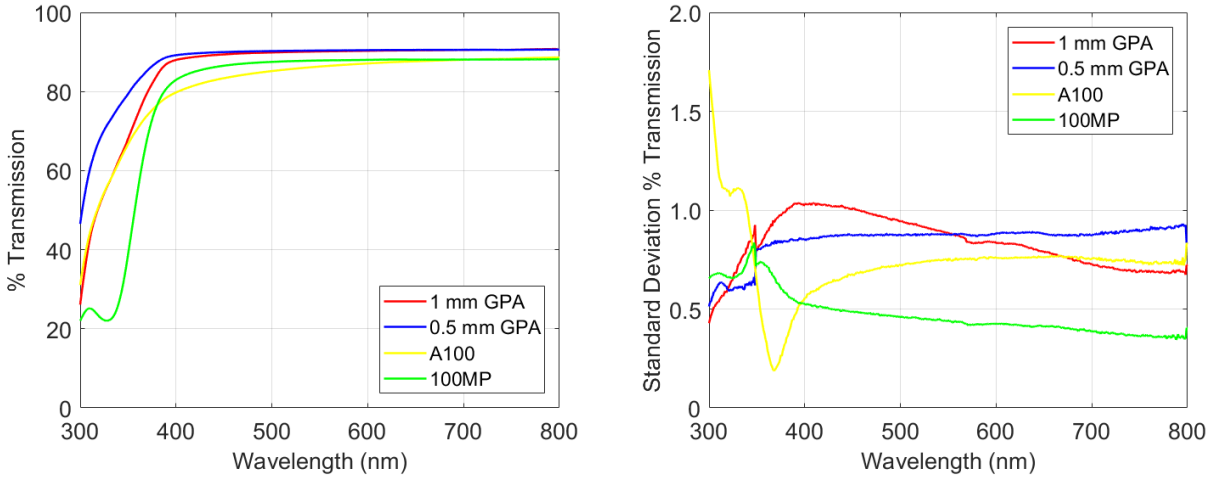

(a) (b)

Figure 4.5.1: (a) Transmission of 300-800 nm light through each tape, averaged over four samples per tape. (b) Standard deviation of transmission between tape samples.

Table 4.5.1: Photopeak amplitude (E_μ) and energy resolution (E_{res}) of the 511 keV photopeak of fitted energy histrograms obtained from coupling a single Teflon-wrapped 1×1×1 cm^3 LYSO:Ce crystal to a PMT using various coupling materials.

Material	Thickness (mm)	E_μ (V)	E_{res} (%)
GPA	1.016	1.36	10.9
A100	0.787	1.30	11.0
GPA	0.508	1.36	10.9
100MP	0.229	1.31	11.2
SiG	∼0.150	1.44	10.8

4.5.2 PMT - single LYSO:Ce crystal

Table 4.5.1 gives the photopeak amplitude and energy resolution for the PMT and single pixel LYSO:Ce coupling cases. Photopeak amplitude of the GPA tapes was 1.36 V, slightly greater than the 100MP and A100 tapes with 1.31 V and 1.30 V amplitude, respectively. SiG had the highest photopeak amplitude of 1.44 V. Energy resolution was 10.8 % for SiG, 10.9 % for both GPA tapes, 11.0 % for A100, and 11.2 % for 100MP.

Table 4.5.2: Per-crystal averaged photopeak amplitude and energy resolution of the 511 keV photopeak of fitted energy histrograms obtained from approximately one-to-cone coupled 4×4 LYSO:Ce and SiPM-C arrays. Uncertainties are given as the standard deviation of values for the 16 segmented crystals.

Material	Thickness (mm)	E_μ (V)	E_{res} (%)
GPA	1.016	5.36 ± 0.17	11.4 ± 1.2
A100	0.787	5.41 ± 0.18	12.3 ± 1.4
GPA	0.508	5.70 ± 0.16	11.7 ± 1.3
100MP	0.229	4.96 ± 0.34	14.0 ± 1.5
SiG	∼0.150	5.82 ± 0.25	15.6 ± 2.7

4.5.3 SiPM array - single-layer 4×4 LYSO:Ce array

Table 4.5.2 gives the per-crystal averaged photopeak amplitude and energy resolution for the PMT and single pixel LYSO:Ce coupling cases. Photopeak amplitude was greatest for SiG at (5.82 ± 0.25) V, while photopeak amplitude reduction for the tapes was in the range of 2.1 % (0.5 mm GPA) and 14.8 % (100MP) with respect to SiG. Energy resolution was

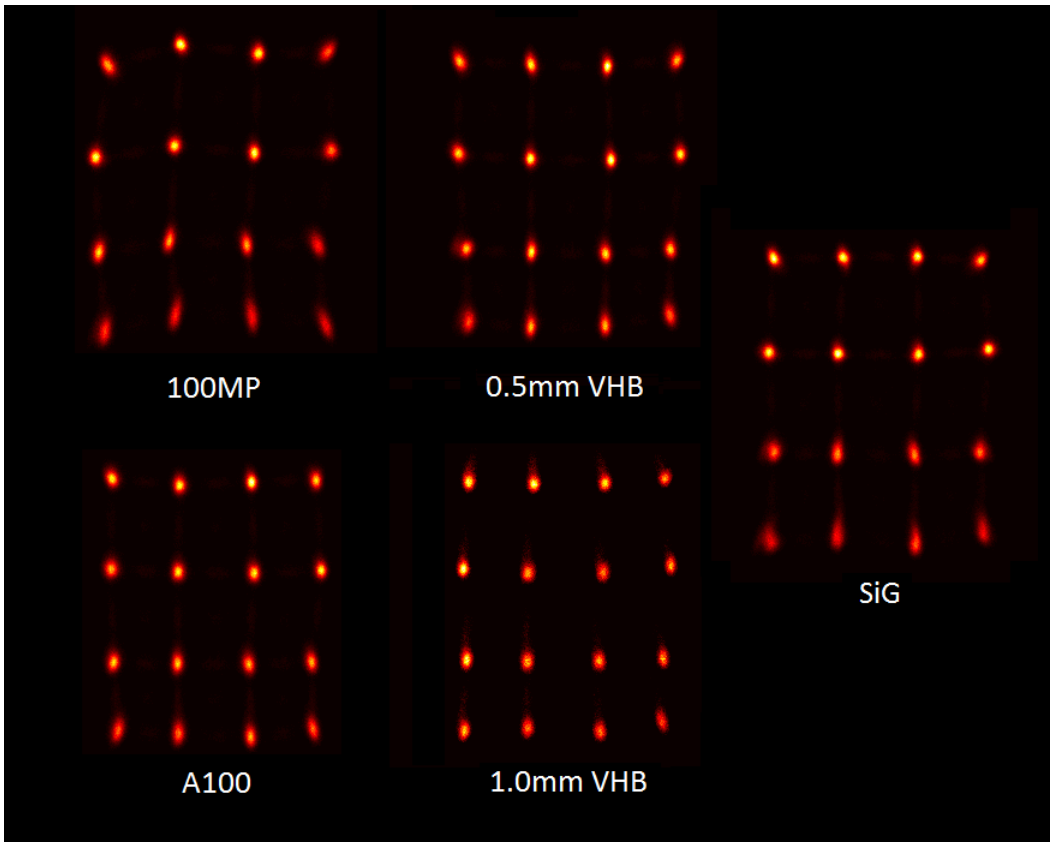

Figure 4.5.2: Flood histograms of one-to-one coupled 4×4 LYSO:Ce-SiPM arrays using various coupling media.

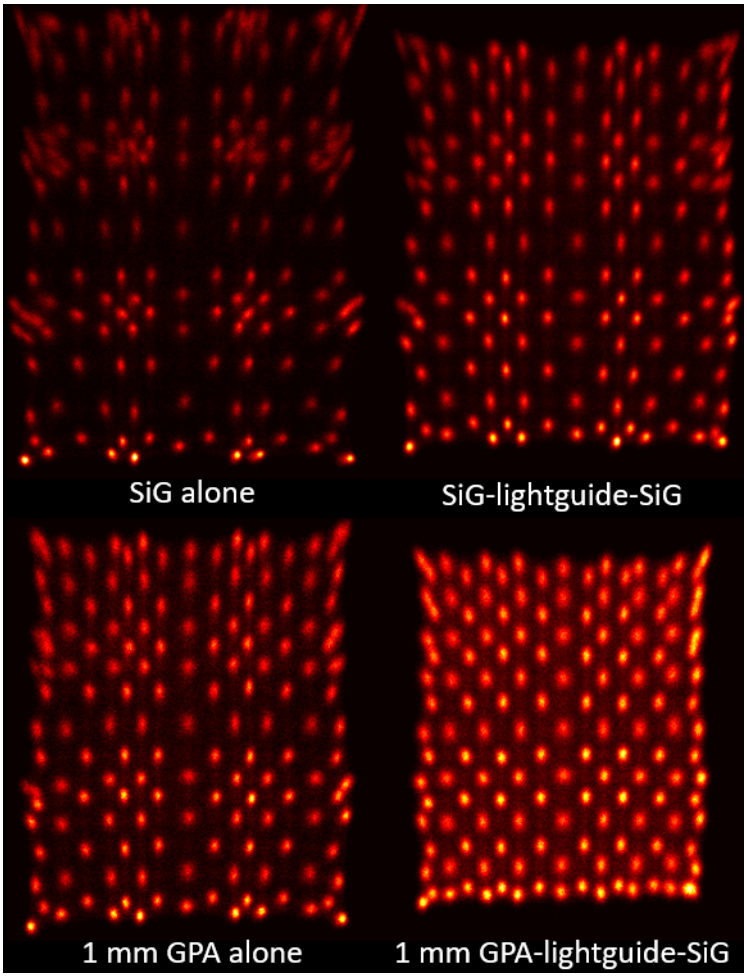

Figure 4.5.3: Flood histograms of the 9×9/8×8 DLO array coupled with SiG alone, SiG - 1 mm lightguide - SiG, 1 mm GPA tape alone, and 1 mm GPA tape - 1 mm lightguide - SiG. Too little light diffusion (SiG alone) causes flood crystal clustering at the SiPM pixels, while too much light diffusion (GPA-lightguide-SiG) causes crystal blurring and uniform flood condensing. Flood histograms for the SiG-lightguide-SiG and the 1 mm GPA tape alone coupling conditions have approximately the same thickness of diffuser and hence are nearly indistinguishable.

best for 1.0 mm GPA at (11.4 ± 0.17) %, and was poorest for SiG at (15.6 ± 2.7) %. Flood histograms in Figure 4.5.2 showed good crystal resolvability for all 16 LYSO:Ce crystals.

4.5.4 SiPM array - DLO 9×9/8×8 LYSO:Ce array

Flood histograms of the four 9×9/8×8 DLO LYSO:Ce coupling scenarios are shown in Figure 4.5.3. Clustering of crystals at the SiPM-C pixels occurs when using SiG alone for coupling.

Table 4.5.3: Photopeak amplitude and energy resolution when using SiG-lightguide coupling and with 1 mm GPA coupling, averaged over the central 5×5/4×4 crystals of the 9×9/8×8 DLO LYSO:Ce array.

Coupling Material	Lightguide?	E_μ (V)	E_{res} (%)
SiG	Yes	6.2 ± 0.2	11.4 ± 1.2
1 mm GPA	No	6.3 ± 0.2	11.3 ± 0.9

Crystal uniformity is best when using the tape and lightguide scenario, however the flood histogram is condensed and the individual crystals are larger.

Table 4.5.3 gives the photopeak amplitude and energy resolution averaged over the central 5×5/4×4 crystals for two coupling scenarios. Very little difference in photopeak amplitude and energy resolution were observed.

4.5.5 SiPM array - DLO 26×13/25×12 LYSO:Ce array

Four flood histograms using the DLO 26×13/25×12 LYSO:Ce array are shown in Figure 4.5.4. Flood histograms with the ESR grid show more uniform crystal separation across the flood image, as well as better crystal resolvability at the corner and edge crystals.

4.5.6 Tape stability vs time

Tape coupling integrity over time is shown in Figure 4.5.5. Relative change in photopeak amplitude and energy resolution measurements were below 10 % for all measurements, relative to Day 0. Gradual improvement is shown for the PMT energy resolution measurements. PMT photopeak amplitude seemed to fluctuate between a 0 - 5 % baseline, which may be explained by daily fluctuations in room temperature since this apparatus was not insulated. In fact, during Day 0 - 37, the laboratory was experiencing inconsistent heating between ∼21.0°C - 23.0°C due to a faulty thermostat. Day-to-day fluctuations in PMT photopeak amplitude appear greater during this time period. After Day 37, the thermostat was fixed

and room temperature was regulated at 20.0°C. However, SiPM measurements were done in a thermally insulated, temperature controlled box, and were not affected by room temperature issues. SiPM measurements showed relatively consistent photopeak amplitude and energy resolution data with a baseline around 0 % relative change. In absolute terms, the maximum difference in SiPM energy resolution was ∼0.5 % with respect to Day 0.

4.6 Discussion

The spectrophotometer transmission data were insightful, but not directly applicable to PET detector coupling scenarios. This transmission data represents the 'worst case scenario' of

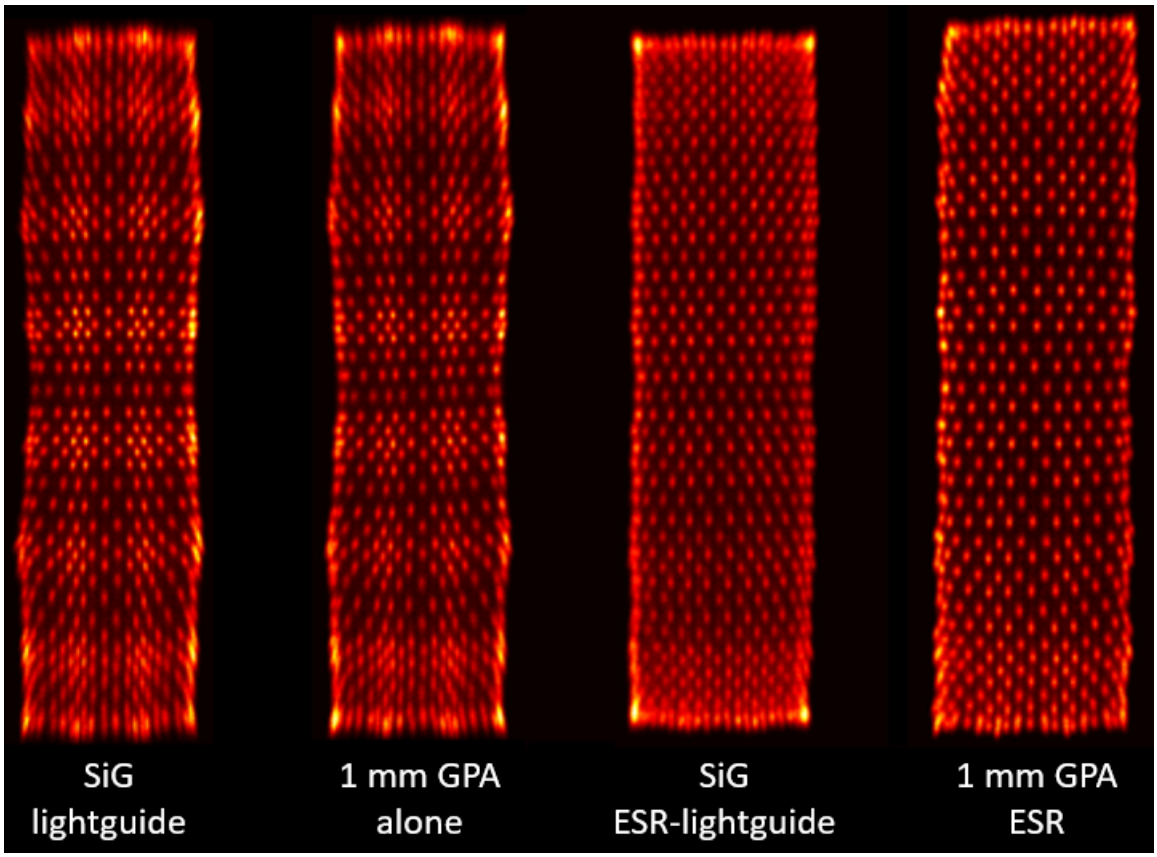

Figure 4.5.4: Flood histograms of a DLO 26×13/25×12 LYSO:Ce array with various coupling scenarios. The left two flood histograms are SiG-lightguide-SiG and GPA-alone coupling, similar to what is shown in Figure 4.5.3. The right two histograms are also coupled with an ESR grid that covers the SiPM-C deadspace between pixels (SiG-lightguide-ESR-SiG coupling and GPA-ESR coupling).

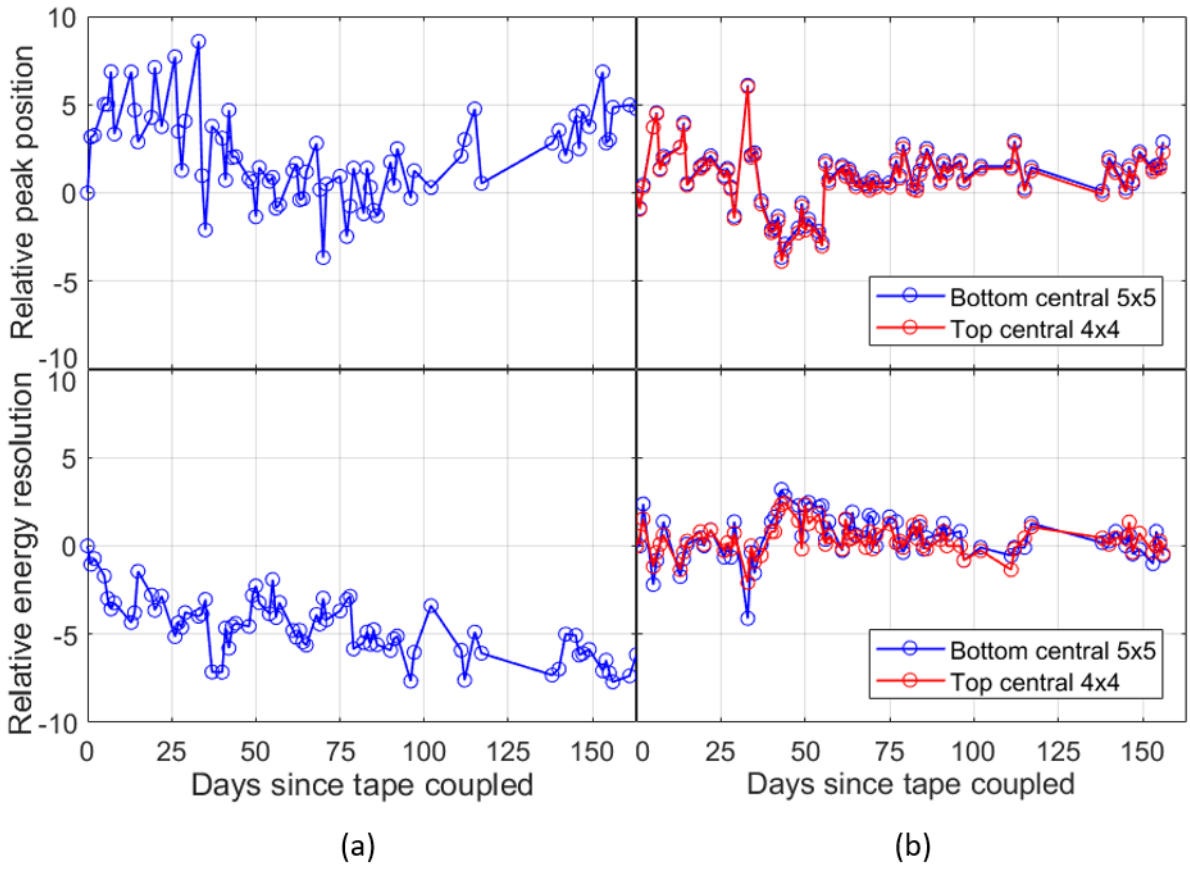

Figure 4.5.5: Stability of photopeak amplitude (top) and energy resolution (bottom) for the PMT - single LYSO:Ce crystal (left) and SiPM - 9×9/8×8 DLO LYSO:Ce array (right). SiPM array data is averaged over the central 5×5/4×4 central pixels of the DLO array. Data is presented as relative change, or percent difference, from Day 0. At Day 0: photopeak position was 437 mV, 6.80 V, and 6.73 V for the PMT, SiPM bottom layer, and SiPM top layer, respectively; energy resolution was 14.0 %, 11.0 %, and 11.1 % for the PMT, SiPM bottom layer, and SiPM top layer, respectively.

tape coupling, since it is a measure of optical transmission through air-tape-air interfaces and not scintillator-tape-photodetector interfaces. Air pockets may be present between scintillator-tape-photodetector interfaces, and this transmission data is more representative of air pocket regions. Optical transmission through scintillator-tape-photodetector coupling is expected to be better, since the refractive index between materials at each interface is better matched than air. Spectrophotometer measurements were consistent with photopeak measurements: since the two GPA tapes had higher photon transmission at 420 nm than the other tapes, more optical photons are expected to be collected for each scintillation event leading to a higher photopeak amplitude.

Photopeak amplitude was greater for SiG than the tapes for both the PMT and SiPM measurements. In relative terms, the photopeak amplitude when using GPA tape was reduced by 2.1 % - 7.8 % with respect to SiG. There are three explanations for this:

i) SiG refractive index (n $\approx$ 1.5) is better matched than the tapes (n is unknown), and therefore optical reflections at the scintillator-SiG-photosensor interfaces are reduced.

ii) The relative thickness of the optical coupling layer is $\sim$0.150μm for SiG [56] versus 508μm or 1016μm for the GPA tapes, and therefore there is more opportunity for absorption as optical photons pass through the tapes.

iii) More air pockets may be present between the tape coupling versus the SiG coupling. The liquid nature of SiG allows for removal of air pockets with relative ease, while the non-liquid but malleable form of tapes make air pocket removal more difficult.

Energy resolution was slightly improved for the PMT coupled to the single LYSO:Ce crystal using SiG, which is likely the result of increased light collection and photopeak amplitude. However, per-crystal energy resolution of the one-to-one coupled 4×4 LYSO:Ce-SiPM arrays using SiG was worse than the tapes. The improvement of energy resolution with the tapes may be explained by light diffusion. Per-crystal energy resolution was best for the 1 mm GPA and worst for SiG, which were the thickest and thinnest coupling media, respectively. Thicker coupling media allow for optical photons to spread over a larger area of the SiPM array. The LYSO:Ce was not perfectly one-to-one coupled to the SiPM array due to differences in pitch (4.0 mm and 4.2 mm for the scintillator and SiPM arrays, respectively) and due to scintillator misalignment while coupling. These effects are minimized if the optical photons are distributed over a larger area of SiPM sensitive volume. Therefore, energy resolution generally improves as the coupling medium thickness increases.

Figure 4.5.3 demonstrates the importance of light diffusion in light sharing detector designs where the scintillator crystal density is greater than the SiPM pixel density. When

coupling the 9×9/8×8 DLO array with SiG only, poor light diffusion causes the flood crystals to appear clustered at the SiPM pixels, leading to poor crystal resolvability and unfeasible crystal segmentation. Crystal resolvability improves drastically when inserting a 1 mm lightguide with SiG coupling, and crystal separation is much more uniform across the flood histogram. The flood histogram when optical coupling with 1 mm GPA tape alone is nearly indistinguishable from the SiG-lightguide-SiG coupling case. There was no difference in photopeak amplitude and energy resolution between these coupling scenarios. The equivalent performance of 1 mm tape versus SiG-lightguide-SiG is because in both scenarios they have approximately the same thickness of diffuser (∼1 mm), hence optical photons are distributed onto the SiPM pixels in a similar fashion. Diffusion layer thickness is effectively doubled (∼2 mm) when adding a lightguide to the GPA coupling. Consequently, crystal sizes are broadened, crystal spacing is condensed, and crystal resolvability suffers (particularly for edge and corner crystals). Flood histograms would condense towards a single point if diffusion layer thickness was increased indefinitely.

A promising attribute to tapes as optical coupling media is that they can effectively replace lightguides as light diffusers. Optical photons must travel through four consecutive media interfaces in conventional light sharing PET detector modules since they must pass through the scintillator-SiG-lightguide-SiG-photodetector media. If tape is used instead, the number of media interfaces is reduced to two: scintillator-tape-photodetector. There is less opportunity for reflectance of optical photons if they must pass through less media interfaces. Furthermore, replacing lightguides with tape is practical, cost-effective, and straightforward.

Figure 4.5.4 demonstrates how 'treating' the diffuser layers by adding an ESR grid can improve flood histograms. Without the ESR grids, flood crystals tended to cluster around the SiPM pixels. Crystal clustering could be eliminated by increasing the diffuser layer thickness. However, this would cause flood crystal size to broaden and flood crystal separation to condense, leading to degradation in crystal resolvability. Instead, the flood histograms were

improved by adding the ESR grid, giving optical photons bound towards SiPM deadspace the opportunity to be reflected and collected by SiPM sensitive volume elsewhere. Both ESR flood histograms showed superior crystal resolvability and separation uniformity versus non-ESR flood images due to increased light collection. Edge and corner crystal resolvability was also improved with ESR coupling, however many of these crystals were still not resolved. The edges of the SiG-ESR-lightguide flood histogram were very straight owing to the rigidity of the glass lightguide. The edges of the GPA-ESR flood histogram were not as uniform, however crystal resolvability of these edge crystals was similar to the glass lightguide case. Edge crystal non-uniformity with tape-ESR coupling is due to the semi-rigid nature of the tapes. The ESR grid has a non-zero thickness, leading to potential air pockets around the rim of the ESR pixel cutouts. Air pockets can generally be worked out with SiG due to it's liquid form, but cannot be worked out easily with the semi-rigid tapes. Furthermore, the edges of the tape itself are not straight, either due to compression of the tapes when coupling the scintillator and SiPMs together or due to human errors when cutting tapes with a box-cutter style knife.

Tape stability over time is demonstrated in Figure 4.5.5. PMT day-by-day fluctuations are likely due to room temperature fluctuations. When temperature is controlled (i.e. for the SiPM measurements), the tape performance in terms of photopeak amplitude and energy resolution remained quite stable. PMT energy resolution improvement may be explained by the tape bond strength over time. According to 3M datasheets, the GPA bond strength approaches its maximum over the first few days. This implies the optical coupling quality is worst during the first few days and improves over time. For the PMT, energy resolution improved over the course of the first week. Subsequent PMT energy resolution measurements can be considered a baseline shift due to the tape reaching its maximum bond strength. This is not evident in the SiPM data. The LYSO:Ce crystal size was $1.41\times1.41\times4$ mm^3 for the 9×9/8×8 array, which has an optical photon exit surface area about 2 % the size of $1.0\times1.0\times1.0$ cm^3 single LYSO:Ce crystal used in the PMT measurements. Optical coupling

quality likely depends on the coupling surface area, and therefore the effect increasing bond strength over time is minimized for the SiPM data since it is evaluated on a per-crystal basis.

The general purpose of optical coupling is to provide a media matched interface that allows for optimal transmission of optical photons from the scintillator to the photodetector. Both SiG and acrylic polymer double-sided tapes have been shown to be operational optical coupling media. The tapes showed minimal photopeak degradation compared to SiG, and their semi-rigid nature resulted in potential air pocket issues. However, there are several advantages of using tapes as optical coupling media. Tapes may be used as light diffusers which eliminates the need for a lightguide, reduces the number of media interfaces, and simplifies the detector module setup. In research applications where scintillators and photodetectors are constantly being changed, tapes are incredibly conventient because they offer mechanical stability without the need for external supports, they are readily available off-the-shelf, and they are applied and removed with relative ease. Tapes may be used in more permanent coupling applications since they were shown to maintain their optical coupling integrity over time, at least over the span of five months. Despite minimal photopeak degradation compared to SiG, acrylic polymer double-sided tapes are an attractive optical material for light sharing photodetector designs.

Chapter 5

Timing Measurements with Single-Pixel SiPM Detectors

5.1 Introduction

In this section, baseline timing measurements were obtained using the DRS4 Evaluation Board V5 and the NIM system for data acquisition. Timing performance for each acquisition system is optimized and characterized. These data represent the optimal detector conditions with a simple two single-pixel SiPM coincidence setup and a high bandwidth signal processing system. Performance degradation is expected when testing full detector modules due to the introduction of SiPM arrays with signal multiplexing, and increase in electronic noise from the addition of more acquisition hardware. Since future coincidence time resolution (CTR) measurements will use a single-pixel as a reference detector, it is important to obtain single-pixel CTR in order to estimate the CTR of a full detector module.

5.2 DRS4 Evaluation Board V5 Acquisitions

5.2.1 Materials

Three pairs of SensL SiPMs were used: B-series (SiPM-B), C-series (SiPM-C), and J-series (SiPM-J). Their specifications are given in Table 5.2.1. Each SiPM is mounted to a PCB board with three SMA connections for SiPM bias, standard output, and fast output. Several data sets were obtained with bias voltage set to 27.0 V - 29.0 V in 0.5 V increments in order to determine which bias results in optimum CTR. SiPMs were coupled to a Teflon-wrapped $4\times4\times4$ mm^3 LYSO:Ce crystal manufactured by Midas Applied Materials Corp., Zhubei City, Taiwan). Visilox V-788 (Rhone-Poulenc Silicones VSI, Troy, NY) silicon optical compound

Table 5.2.1: General properties of the three SensL single-pixel SiPMs. Note these SiPM-B pixels have a fast output, unlike the SiPM-B array SPMArray4B discussed in Section 2.4.3.

Detector	SiPM-B	SiPM-C	SiPM-J
Pixel model	MicroFB-SMA-30035	MicroFC-SMA-30035	MicroFJ-SMA-30035
Active area (mm^3)	3×3×3	3×3×3	3.07×3.07×3.07
No. of microcells/pixel	4774	4774	5676
Microcell fill factor (%)	64	64	75
Breakdown voltage V_{br} (V)	24.0 - 25.0	24.2 - 24.7	24.2 - 24.7
Peak PDE λ_{peak} (nm)	420	420	420
PDE for λ_{peak} (%)	31	31	38
Gain (standard output)	3×10^6	3×10^6	2.9×10^6
Dark count rate (MHz)	6.7	0.300 (max 0.860)	0.405 (max 1.413)
Capacitance standard output (pF)	850	850	1000
Capacitance fast output (pF)	12	12	40

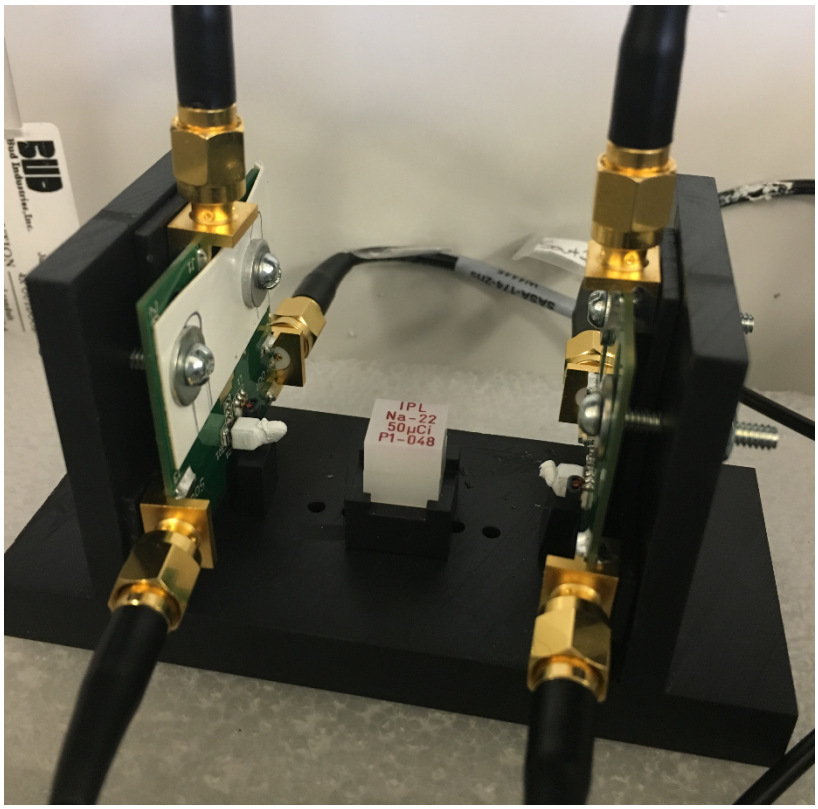

Figure 5.2.1: 3D printed support with SiPM PCB mounts, variable-size supports for scintillators, and a 10×10×10 mm^3 source stage positioned at the centre of the SiPMs.

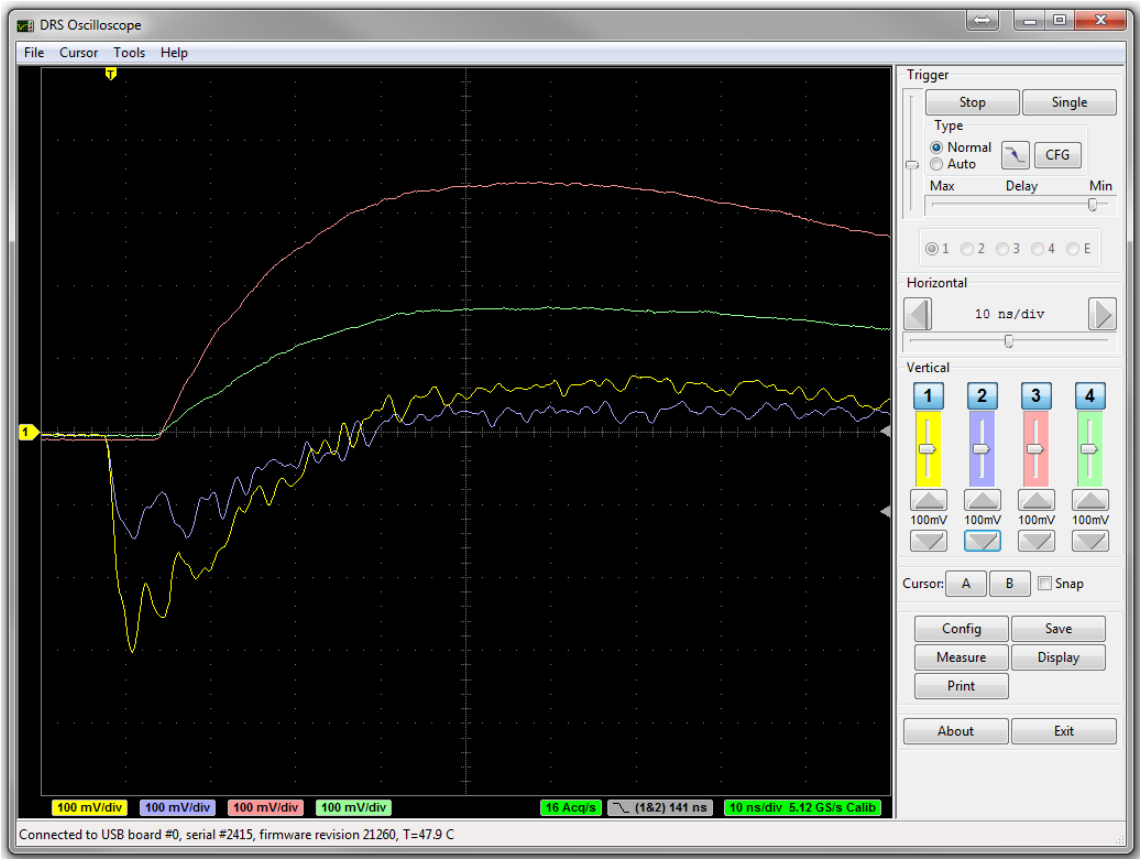

Figure 5.2.2: Screenshot of DRS Oscilloscope, showing captured waveforms of the standard outputs (red & green) and fast outputs (yellow & blue).

(SiG) was used for optical coupling. The positron source used was a ∼50 μCi ^{22}Na source embedded in a 1×1×1 cm^3 acrylic cube. A custom support was 3D printed in-house with PCB mounts, LYSO:Ce pixel supports, and a ^{22}Na source holder for precise source alignment (shown in Figure 5.2.1). When mounted, the SiPM pixels were separated by ∼4.9 cm. The detector setup was placed in a light tight box and covered in a thick black curtain to minimize light leakage.

Signal readout was done with a DRS4 Evaluation Board V5, the pocket-sized waveform digitizer briefly described in Section 3.2.2. SiPM standard outputs were input directly into the DRS4 analog input channels. SiPM fast outputs were transmitted via RG-174 SMA-SMA cables to ZX60-4016-S+ amplifiers then transmitted via RG-58 SMA-SMA cables to the DRS4 analog inputs. The RG-174 cables are 10 ns long with 3 GHz bandwidth, while RG-58 cables are 2 ns long with 1 GHz bandwidth. The DRS4 board output was connected to PC via USB, and the DRS Oscilloscope software (Figure 5.2.2) was used for data acquisition. For all DRS4 board measurements, 3×10^4 coincidence events were obtained. Total event count was kept relatively small due to the high computation time of the DRS4 board waveform output files. The waveform capture trigger was set to the standard outputs in coincidence with a threshold of 150 mV. This threshold was found to be within the Compton portion of the energy spectra, therefore a significant portion of the 3×10^4 coincidence events were 511 keV photopeak events. The waveforms of the standard and fast output of each SiPM pixel were captured for further processing.

Waveform processing was done using 'DRS4.m' software developed in MATLAB 2016a (MathWorks, Natick, MA). Standard output waveforms were corrected for DC offset (for example, notice the presence of a ∼10 mV offset of the standard output (red) in Figure 5.2.2) and filtered/smoothed with a simple boxcar filter. Energy values for each event were taken as the maximum amplitude of the corrected standard output waveform. Separate energy histograms for each pixel were constructed and fit with the double Gaussian function

(Equation 3.13). Recall that one Gaussian is fit to the 511 keV photopeak and the other is crudely fit to the Compton shoulder. The energy histograms were processed with 400 - 650 keV and 440 - 600 keV energy windows, as well as no energy window, to determine how CTR is affected by energy window selection.

Next, the time waveforms of the energy-filtered coincidence events were processed. Several time pickoff thresholds were investigated to determine the optimal threshold setting. For each user-defined threshold, the first time waveform bins above and below the threshold value were found. The timestamp was determined through linear interpolation between these bins. The difference in photon arrival times (Δt) was the calculated as the difference in timestamps between opposing SiPM pixels. Coincidence times were histogrammed and fit with a double Gaussian function: one to fit the primary Gaussian peak and the other to crudely fit noise events at the tails of the primary Gaussian peak. Unlike with energy measurements, the FWHM CTR was determined analytically: the two half-maximum points of the fit were found through linear interpolation of neighbouring bins, and the CTR was simply the difference between these points. An example of analyzed DRS4 data with fitted energy and time histograms is shown in Figure 5.2.3.

5.2.2 Methods

The following measurements were performed to determine optimum DRS4 acquisition conditions:

Comparison of SiPM-B, SiPM-C, and SiPM-J photosensors. Two SiPM-B pixels were placed in coincidence, each coupled with a Teflon-wrapped 4×4×4 mm^3 LYSO:Ce crystal. The SiPMs were biased at 29.0 V. Energy spectra were filtered with a 400/650 keV energy window. CTR was obtained from the waveform data using time pickoff thresholds of 5, 10, 25, 50, 75, and 100 mV. This process was repeated for the SiPM-C and SiPM-J

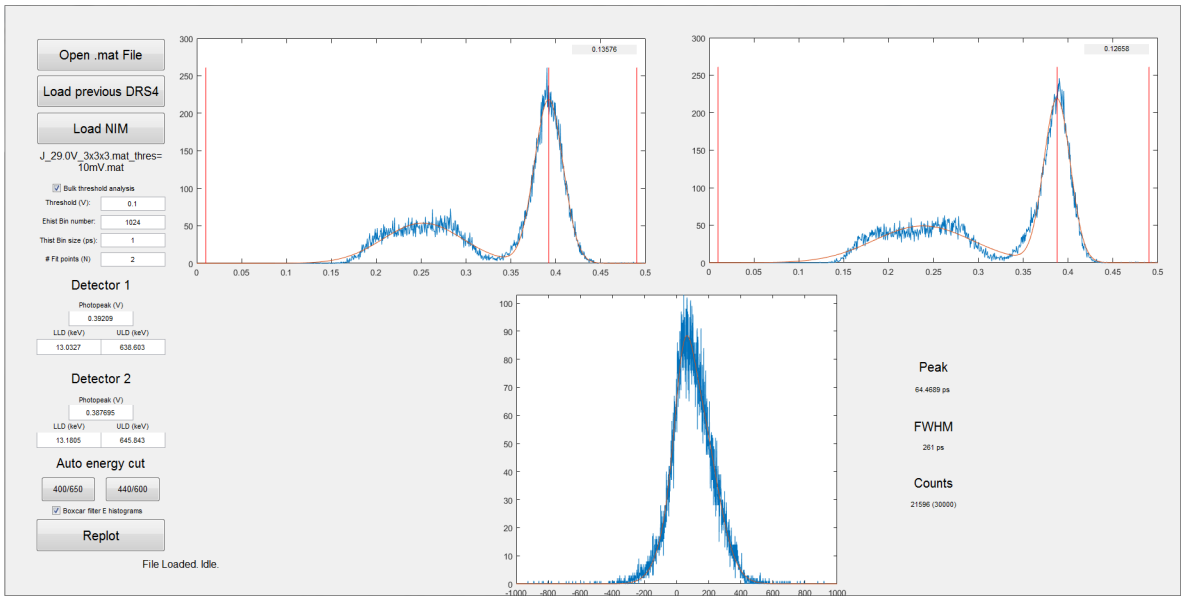

Figure 5.2.3: Screenshot of MATLAB software for DRS4 board measurements. The processed data is from a SiPM-J coincidence measurement with 3×3×3 mm^3 LYSO:Ce crystals and a 10 mV time pickoff threshold. The top two plots are the energy spectra of each of the SiPM pixels, fit with a double Gaussian function. The outer red vertical lines represent the lower and upper discriminators of the energy window, and the central vertical line is set to the photopeak fit maximum. The bottom plot is the time histogram of all events falling inside the energy window, fit with a double Gaussian function.

pixels.

Fine-tune of time pickoff threshold. For the SiPM-J pixels, the waveforms captured in the previous section were reprocessed using time pickoff thresholds of 5 - 15 mV in 1 mV increments.

Optimization of bias voltage. For SiPM-C and SiPM-J pixels, measurements were obtained with the bias voltage set to 27.0 V - 29.0 V in 0.5 V increments. At each bias voltage, CTR was obtained from the waveform data using time pickoff thresholds of 5, 10, 25, 50, 75, and 100 mV.

Signal transmission cable optimization. The use of 1 GHz and 3 GHz bandwidth SMA-to-SMA cables was investigated using SiPM-J pixels. SiPM bias was 29.0 V and time pickoff threshold was 10 mV. SiPMs were coupled to Proteus Inc. (Chagrin Falls, OH)

3×3×3 mm^3 LYSO:Ce crystals. Two timing measurements were obtained: one with the same cable configuration as previously described (i.e. fast output to amplifier via RG-174 cables, then amplifier to DRS4 via RG-58 cables), and the other swapping out the RG-58 cable (i.e. fast output to amplifier to DRS4 each via RG-174 cables). CTR was calculated for an 8 mV time pickoff threshold and 400 - 650 keV energy window.

5.2.3 Results and Discussion

Comparison of SiPM-B, SiPM-C, and SiPM-J photosensors. The CTR for SiPM-B, SiPM-C, and SiPM-J pixels at various time pickoff thresholds is shown in Figure 5.2.4. For all pickoff thresholds, CTR was best for the SiPM-J. Improvement of CTR between SensL SiPM generations can be explained by inter-generational improvement in PDE. Higher PDE improves timing because ballistic optical photons are more likely to cause microcell firing. According to SensL datasheets, PDE of 420 nm optical photons is 31 %, 31 %, and 38 % the SiPM-B, SiPM-C, and SiPM-J SMA single-pixel detectors, respectively, when biased at breakdown voltage (V_{br}) + 2.5 V. This explains why SiPM-J CTR was better than the others.

Dark count rates (i.e. the rate of microcell firing in the absense of optical photons) also affects CTR. When a dark count occurs in one SiPM pixel, a false coincidence trigger will occur if a count (a real radiation event or a dark count) occur in the other SiPM pixel within the coincidence time window. At bias of V_{br} + 2.5 V, the dark count rate is 6.7 MHz, 300 kHz, and 450 kHz for SiPM-B, SiPM-C, and SiPM-J, respectively. The improvement of CTR from SiPM-B to SiPM-C generations is likely due to the reduction in dark count rate by a factor of ∼20.

The primary difference between SiPM-C and SiPM-J generations is an increase in microcell concentration. Consequently, both PDE and dark count rate increased: improvement

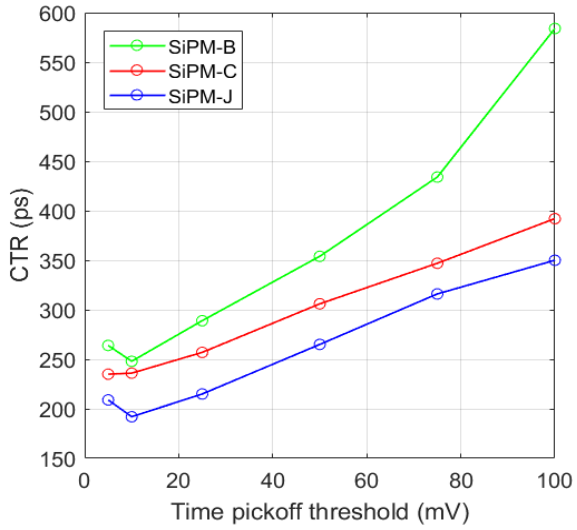

Figure 5.2.4: Coincidence time resolution of SiPM-B, SiPM-C, and SiPM-J pixels at various time pickoff thresholds using DRS4 waveform capture. CTR was best for SiPM-J at all thresholds. The optimal time pickoff threshold was 10 mV for all SiPMs.

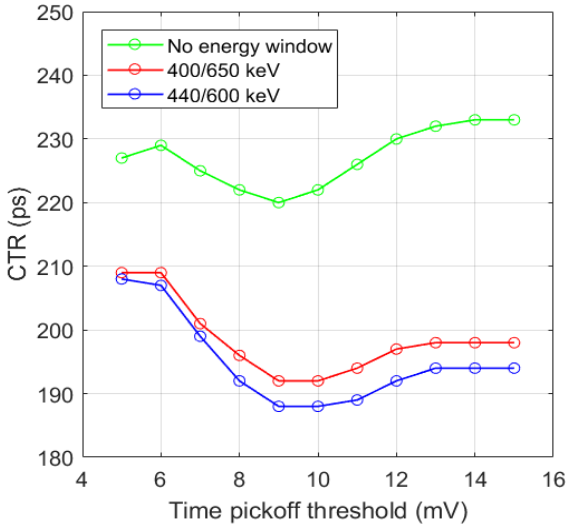

Figure 5.2.5: CTR of SiPM-J at timing pickoff thresholds of 5-15 mV for three energy window settings.

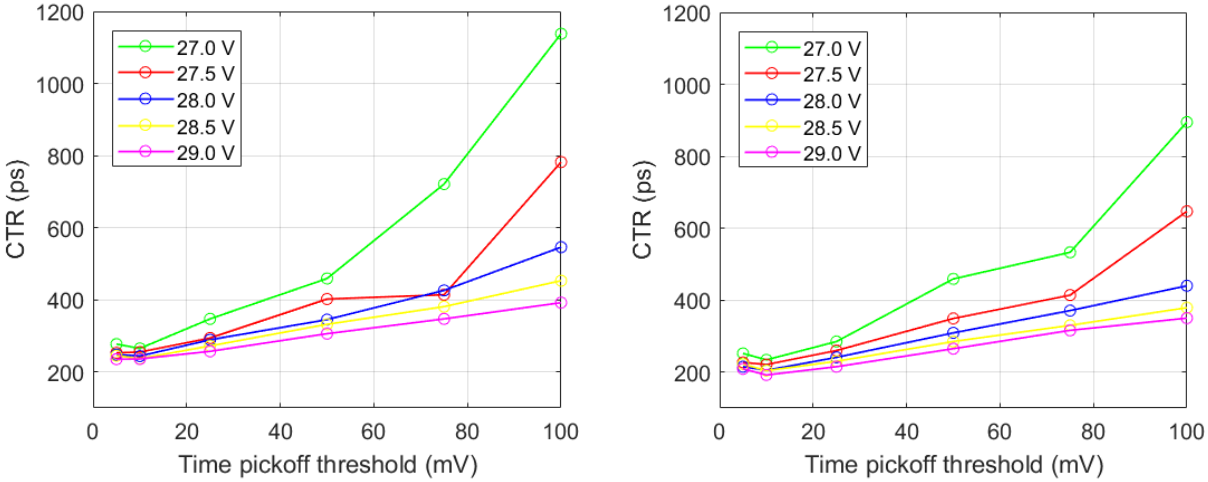

(a) (b)

Figure 5.2.6: CTR for various voltage biases and time pickoff thresholds for (a) SiPM-C and (b) SiPM-J pixels in coincidence.

in CTR between SiPM-C and SiPM-J is likely the tradeoff between increased PDE and increased dark count rate.

In general, CTR is optimized when timestamps are extracted from the initial rising portion of the time waveforms [57]. The lowest trigger thresholds should yield the best results. This initial rise of the fast output waveform represents the first generated photoelectrons due to the arrival of ballistic optical photons. Ideally, the timing pickoff threshold would be set just below one photoelectron for the best timing results. In practice, electronic noise and SiPM dark counts cause coincidence triggering when the time pickoff threshold is set too low. Time pickoff threshold must be set high enough to avoid dark triggers, but low enough to preserve the optimum timing performance. As shown in Figure 5.2.4, CTR was best at 10 mV for each SiPM. At 10 mV threshold, CTR was 193 ps, 236 ps, and 248 ps for SiPM-J, SiPM-C, and SiPM-B, respectively.

Fine-tune of time pickoff threshold. Results from fine-tuning of the optimum time pickoff threshold is shown in Figure 5.2.5. Optimum pickoff threshold was found to be 9 - 10 mV. Figure 5.2.5 also demonstrates the effect of energy window selection on CTR. At 9 mV threshold, CTR was 220 ps when using no energy window, while CTR was 192 ps and 188 ps when using 400/650 keV and 440/600 keV energy windows, respectively. Energy windows are imposed in order to exclude scattered events. If an annihilation photon is scattered within the scintillator, the recoil electron generates less optical photons than a photoelectron would, leading to poorer photon statistics and degraded CTR. Note that annihilation photons directed away from the scintillators may be scattered towards the scintillator and absorbed, further degrading CTR. In-scattering in this manner is highly improbable for this single-pixel setup, but is much more of a concern for large PET imaging systems.

Table 5.2.2: CTR when using 3 GHz bandwidth cables versus 1 GHz for signal transmission of the fast outputs from the amplifiers to the DRS4 analog inputs.

Cable type	Cable length (ns)	Bandwidth (GHz)	CTR (ps)
RG-174	10	3	168
RG-58	2	1	191

Optimization of bias voltage. CTR versus SiPM bias for the SiPM-C and SiPM-J pixels is plotted in Figure 5.2.6. For both detectors, CTR was best with the bias at 29.0 V. CTR was 236 ps and 192 ps for SiPM-C and SiPM-J, respectively at 10 mV threshold and 29.0 V bias. Bias voltages higher than 29.0 V resulted in a significant increase in dark count triggering and therefore were not used for CTR measurement.

Signal transmission cable optimization. The choice in signal transmission cable had a significant impact on CTR. For the 3 GHz RG-174 and 1 GHz RG-58 cables, CTR was 168 ps and 191 ps, respectively. CTR was degraded due to the limiting bandwidth of the RG-58 cables. All future timing measurements with the NIM acquisition system were performed with 3 GHz bandwidth RG-174 cables for signal transmission.

5.3 TAC Calibration

The ORTEC 567 TAC was calibrated before any NIM-acquired timing measurements were done. This TAC unit outputs a unipolar pulse with 0 to 10 V amplitude proportional to the start/stop time difference. Three time range options are available: 50 ns, 100 ns, and 200 ns (R50, R100, and R200, respectively). In order to extract real timing information from digitized time signals, a calibration factor must be applied to convert ADC voltage to time.

Note that the full 0 to 10 V TAC range was not used. Before digitization, the TAC output (as well as ADC output) was fed into the Niagra Engineering Works sample-and-hold unit which has a 0 to 3 V amplitude range. Therefore, all input signals (both standard

and fast output signals) were limited to a maximum amplitude of 3 V.

A basic NIM setup (as discussed previously in Section 3.2.1 and shown in Figure 3.2.2) was used to calibrate the TAC for each time range option. Two SiPM-C pixels were placed in coincidence, each coupled with SiG to a Teflon-wrapped 4×4×4 mm^3 LYSO:Ce crystal. The LED was set to coincidence mode with a 10 mV fast output threshold. The ~50 μCi ^{22}Na source was placed between the SiPMs secured on the SMA mount. One LED TTL was fed directly into the TAC start input, while the other was fed to a Phillips Scientific 792 delay module before being input into the TAC stop. For the R50 and R100 settings, the delay module was set to 6, 8, 10, 12, and 14 ns. For the R200 setting, the delay module was set to 8, 12, 16, 18, 20, 22, and 24 ns. Each TAC delay shifts the timepeak in a linear proportion. Data were acquired for five minutes at each delay setting.

The digitized NIM output was processed in MATLAB with the 'DRS4.m' software which was modified to read in NIM data (i.e. no waveform capture analysis required). Energy histograms were fit with a double Gaussian function then filtered with a 440/600 keV energy window. Time histograms were fit with a single Gaussian function. Time peak positions (i.e. the mean of the time Gaussian fit) were plotted versus delay module setting and fit with a linear trendline. The 'Data Analysis' toolbox in Microsoft Excel 2016 (Microsoft, Red-

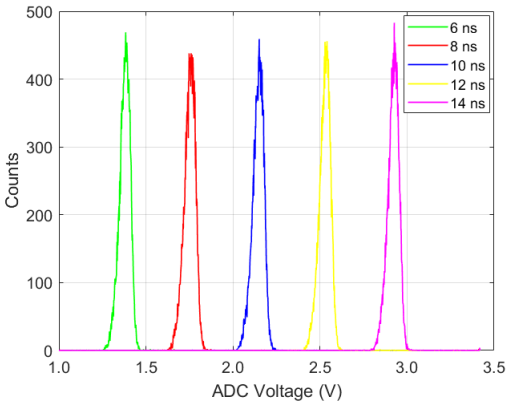

Figure 5.3.1: Time histograms of the R50 TAC calibration measurements with start/stop delays of 6, 8, 10, 12, and 14 ns.

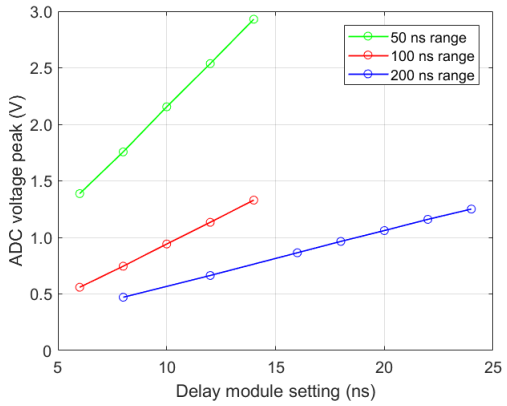

Figure 5.3.2: Calibration of R50, R100, and R200 settings for the TAC. The slopes of each linear fit give the calibration factor for each setting.

Table 5.3.1: TAC calibration factors and 95% confidence intervals.

Setting	Slope (V/ns)	Calibration factor (ns/V)	95% confidence interval
R50	0.19328	5.1738	5.0724 / 5.2794
R100	0.09650	10.3632	10.2066 / 10.5247
R200	0.04906	20.3828	20.1323 / 20.6398

mond, WA) was used to perform linear regression on the data and calculate 95% confidence intervals. The inverse slope of the linear fit gives the TAC calibration factor.

The time histograms of the R50 calibration measurements are plotted in Figure 5.3.1. Each time histogram appears uniformly spaced, indicating a linear relationship between start/stop delay and ADC voltage. The TAC calibration plot is shown in Figure 5.3.2. Linear fit slopes, calibrations factors, and the 95% confidence interval is given in Table 5.3.1. The coefficient of determination (R^2) was 0.9999 for each linear fit, indicating good agreement between the fit and the calibration data. Calibration factors in Table 5.3.1 were used to convert ADC voltage to time for all NIM timing measurements in this work.

5.4 NIM Acquisitions

5.4.1 Materials

Several timing measurements were obtained with single-pixel SiPMs using the NIM acquisition system. The SiPM SMA boards were secured to the 3D printed mount and placed in a light-tight box. SiPMs were biased at 29.0 V. Standard outputs were input directly into the Mesytec shaping amplifier, while fast outputs were amplified by Mini-Circuits ZX60-4016-S+ amplifiers then input into the LED. Twenty minute acquisitions were obtained with the ^{22}Na source placed in the centre of the SiPMs. Using the modified DRS4.m software, energy histograms were fit with a double Gaussian function, and time histograms were fit with a single Gaussian function. CTR was calculated using a 400/650 keV energy window.

5.4.2 Methods

The following measurements were made for CTR characterization and optimization using the NIM acquisition system:

DRS4 and NIM acquisition comparison. NIM timing measurements were directly compared to DRS4 measurements using identical detector setups. SiPM-J and SiPM-C pixels were coupled with SiG to either the Midas 4×4×4 mm^3 or the Proteus Inc. 3×3×3 mm^3 LYSO:Ce crystals (both crystals were Teflon-wrapped). For each of these four setups, the data were acquired using the DRS4 Evaluation Board V5 and the NIM electronics. The apparatus was left untouched when switching between acquisiton systems. For DRS4 acquisitions, waveforms were captured with a 100 mV coincidence trigger on the standard output, and 3×10^4 coincidence events were processed in software with a 10 mV fast output time pickoff threshold. For NIM acquisitions, events were triggered on fast output coincidence with the LED set to 10 mV.

NIM LED threshold fine-tune. SiPM-C pixels were coupled with SiG to 3×3×3 mm^3 Proteus LYSO:Ce crystals. Coincidence was triggered on the fast outputs with the LED set to 4 - 10 mV in 1 mV increments.

'Cascaded' amplifier setup. SiPM-C pixels were coupled with SiG to 3×3×3 mm^3 Proteus LYSO:Ce crystals. The fast outputs were each passed through two consecutive amplifiers: first Mini-Circuits ZX60-4016-S+ then Mini-Circuits ZFL-1000LN+. Coincidence events were triggered on the double-amplified fast outputs with LED thresholds of 100, 200, and 255 mV. Note the maximum LED threshold option is 255 mV for the CAEN Model N845 LED module.

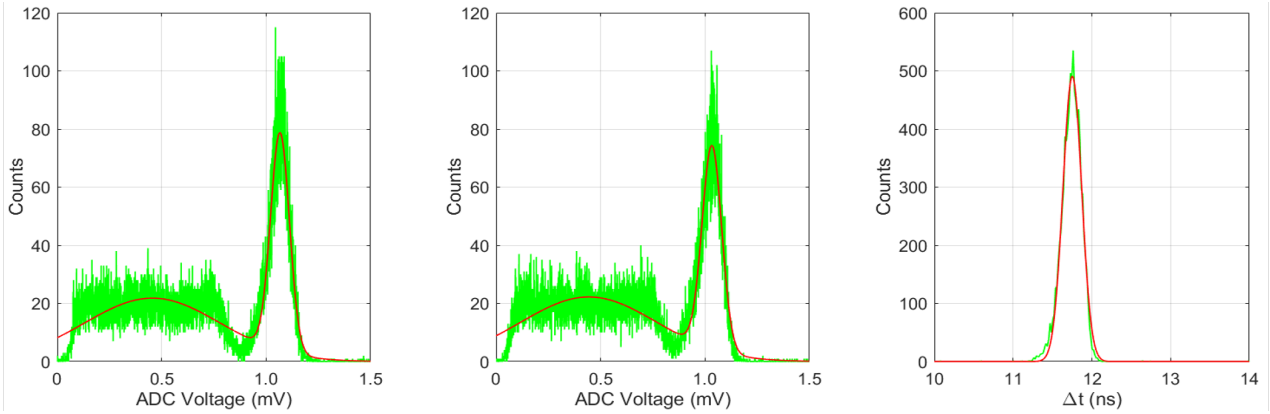

(a) (b) (c)

Figure 5.4.1: (a) and (b) Energy histograms of each pixel, and (c) the coincidence time histogram for SiPM-C single-pixels coupled to 3×3×3 mm^3 LYSO:Ce crystals. Data was acquired with the NIM system using a 10 mV LED threshold.

NIM reproducibility. SiPM-C pixels were coupled with SiG to 3×3×3 mm^3 Proteus LYSO:Ce crystals. The master trigger was set to fast output coincidence with a 10 mV LED threshold. Four 20 minute acquisitions were obtained with the ^{22}Na source. Between each acquisition, the LYSO:Ce crystals were removed and recoupled.

5.4.3 Results and Discussion

DRS4 and NIM acquisition comparison. Table 5.4.1 gives the CTR of the DRS4 and NIM measurements for various SiPM and scintillator setups. For all measurements with

Table 5.4.1: CTR of SiPM-C and SiPM-J pixels using two different size LYSO:Ce crystals, comparing the timing performance of DRS4 and NIM acquisition systems. CTR values were obtained with a 400/650 keV energy window.

SiPM type	LYSO:Ce crystal size (mm^3)	Acquisition system	CTR (ps)
SiPM-J	3×3×3	DRS4	163
SiPM-J	3×3×3	NIM	239
SiPM-J	4×4×4	DRS4	195
SiPM-J	4×4×4	NIM	333
SiPM-C	3×3×3	DRS4	200
SiPM-C	3×3×3	NIM	270
SiPM-C	4×4×4	DRS4	232
SiPM-C	4×4×4	NIM	362

the same SiPM and scintillator setup, the CTR with DRS4 acquisition was significantly better than NIM acquisition. Each module introduces electronic noise and may have limited bandwidth, which degrades the time signal. Signal path length is much longer for NIM acquisition, and some signal degradation occurs along LEMO-LEMO RG-174 transmission cables between the various modules. In contrast, time signals are preserved when using the 5 GS/s waveform capture of the DRS4, allowing for more precise threshold selection in the processing software.

Other comparisons between detector setups can be made with these data. CTR improvement between SiPM-J and SiPM-C pixels was 31-37 ps, which is consistent with the DRS4 measurements in Section 5.2. The scintillator size affected the CTR as well. CTR improvement between 3×3×3 mm^3 and 4×4×4 mm^3 LYSO:Ce was 32 ps for DRS4 acquisitions and 94 - 99 ps for NIM acquisitions. The difference in CTR may be due to the crystal size. Ideally, each photoelectron generates the same number of optical photons in both crystal types. However, since the coupling face of the 4×4×4 mm^3 LYSO:Ce is larger than the 3×3 mm^2 active area of the SiPM pixel, a significant number of optical photons encounter the dead space surrounding the SiPM pixel. Light loss leads to poorer photon statistics which can degrade CTR. This is because time TTLs are triggered on the arrival of the first few ballistic photons, which are the optical photons that travel in a straight path to the photodetector without any reflections or scatters. Photons destined for pixel dead space or reflective boundaries generally do not contribute to timing performance. Instead, the difference in CTR is likely due to the quality of the LYSO:Ce pixels since they were obtained from different manufacturers.

NIM LED threshold fine-tune. CTR versus LED threshold is plotted in Figure 5.4.2b. CTR was optimum at thresholds 4 - 7 mV. At 7 mV and 10 mV thresholds, CTR was 236 ps and 270 ps, respectively. Normalized energy histograms of the acquisitions with LED threshold of 4 mV, 7 mV, and 10 mV are shown in Figure 5.4.2a. For 4 mV, 7 mV, and

Table 5.4.2: Energy resolution and CTR when amplifying SiPM-C fast outputs through consecutive ZX60-4016-S+ and ZFL-1000LN+ Mini Circuits amplifiers.

LED threshold (mV)	E_{res} pixel 1 / pixel 2 (%)	CTR (ps)
100	7.9 / 8.1	210
200	9.0 / 8.5	205
255	9.1 / 8.4	200
10*	9.9 / 10.7	270

*Acquired with only amplification using Mini Circuits ZX60-4016-S+ amplifiers.

10 mV, photopeak amplitude was 431 mV, 417 mV, and 417 mV, respectively, while energy resolution was 8.4 %, 9.1 %, and 9.1 %, respectively. The difference in photopeak amplitude between the 4 mV and other acquisitions is likely due to a difference in ambient room temperature, since these acquisitions were taken on different days. Notice the sharp peak at the beginning of the 4 mV and 7 mV spectra which correspond to dark count triggers. At very low LED thresholds, the relative number of dark triggers versus true triggers rises. A compromise must be made between CTR and dark count trigger rate when choosing the LED threshold level.

'Cascaded' amplifier setup. The energy resolution and CTR for the cascaded amplifier measurements is given in Table 5.4.2. CTR improved significantly when using consecutive amplifiers versus the standard 10 mV threshold single-amplifier scenario. This is because the portion of the signal that corresponds to the first few photoelectrons is amplified, and therefore the trigger threshold of the LED is selected with higher precision.

The energy histograms for each cascaded amplifier measurement are shown in Figure 5.4.3. Significant dark count triggers are seen in the 100 mV threshold energy spectrum.

NIM reproducibility. NIM reproducibility measurements are given in Table 5.4.3. Photopeak position and energy resolution varied from 0.88 V to 1.15 V and 9.0 % to 10.7 %, respectively, likely due to misalignment of the 3×3×3 mm^3 LYSO:Ce crystal between acquisitions. Despite these variations, CTR remained within 268 - 277 ps. Small crystal

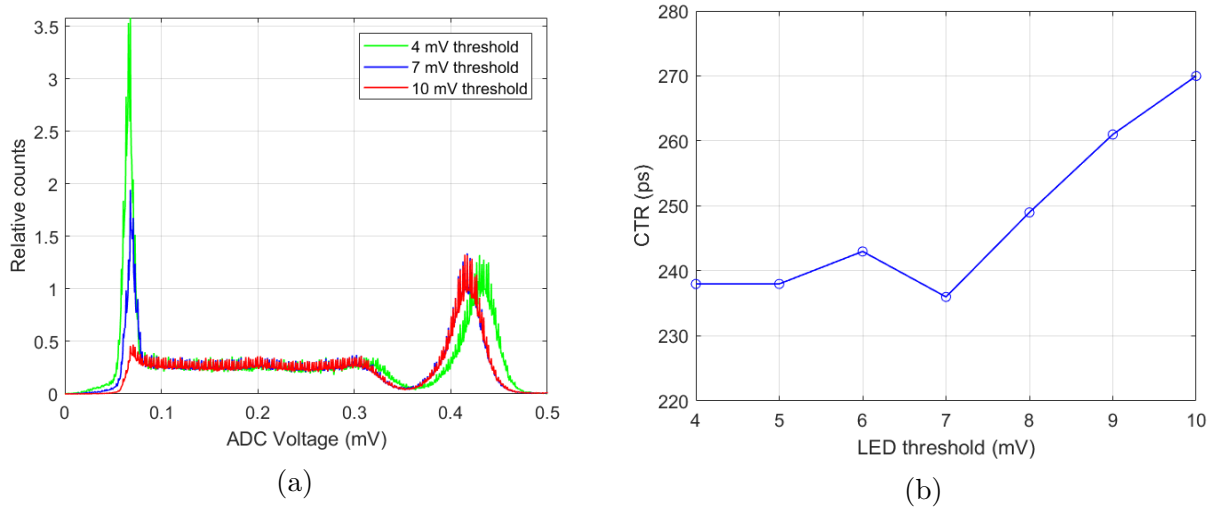

(a) (b)

Figure 5.4.2: LED threshold fine-tuning for NIM acquisition. (a) Energy histograms of one SiPM-C pixel for 4 mV, 7 mV, and 10 mV LED threshold acquisitions, with counts normalized to their respective photopeak amplitude. (b) CTR versus LED threshold.

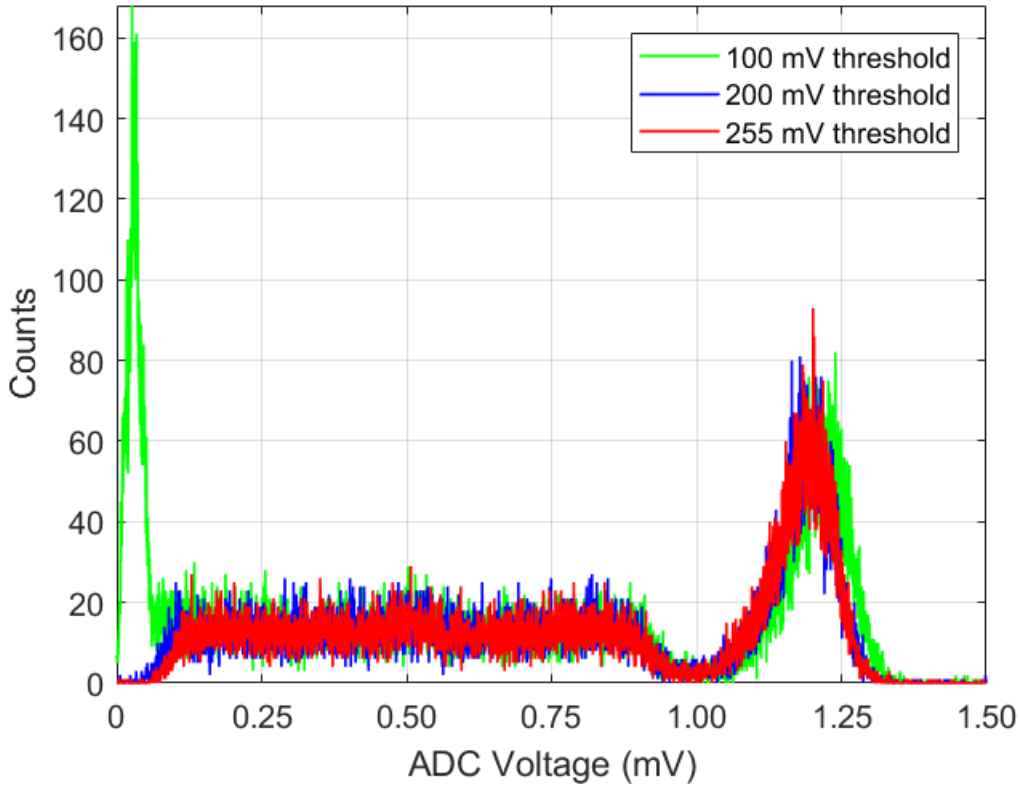

Figure 5.4.3: Energy histograms of NIM acquired data when using cascaded amplification of fast outputs with LED thresholds of 100 mV, 200 mV, and 255 mV Significant dark count triggers are present for the 100 mV energy histogram.

Table 5.4.3: Energy resolution and coincidence time resolution of four SiPM-C single-pixel measurements using the NIM system for data acquisition. Each apparatus was identical, except the 3×3×3 mm^3 LYSO:Ce crystals were recoupled between acquisitions.

Measurement #	E_μ pixel 1 / pixel 2 (V)	E_{res} pixel 1 / pixel 2 (%)	CTR (ps)
1	1.15 / 1.00	9.2 / 9.2	277
2	1.09 / 0.93	9.0 / 10.0	270
3	1.05 / 0.93	9.9 / 9.9	272
4	1.10 / 0.88	9.8 / 10.7	268

misalignments do not affect CTR as much since timing dependends on the arrival of the first few ballistic photons rather than the collection of many optical photons.

5.5 Conclusion

Several calibration, optimization, and characterization measurements of single-pixel CTR were obtained using DRS4 and NIM acquisition. In general, CTR was optimum under the following conditions:

1) The most recent generation of SiPM was used (i.e. SiPM-J),

2) SiPMs were coupled with high-quality LYSO:Ce crystals,

3) SiPMs were biased as high as possible (i.e. 29.0 V) before significant dark triggering occurred,

4) Time thresholds (i.e. waveform pickoff threshold for DRS4 and LED threshold for NIM) were set as low as possible before significant dark triggering occurred,

5) High bandwidth signal transmission cables were used for fast output transmission (i.e. 3 GHz RG-174 cables instead of 1 GHz RG-58 cables),

6) Fast outputs were double-amplified to facilitate precise threshold setting,

7) Acquisition with high-sample-rate wave capture with linear interpolation for time

threshold measurement was done instead of signal processing using consecutive NIM modules which introduce electronic noise and degrade time performance.

The NIM system will be used for future CTR measurements of the second-generation PET detector modules. This is because the DRS4 board can only read out four channels at once, and also because the DRS4 waveform capture output files are large and take a relatively long time to process versus the NIM list-mode output files.

Chapter 6

Timing and Count Rate Measurements with Detector Modules

6.1 Coincidence Time Resolution

6.1.1 Introduction

Coincidence time resolution measurements of the second-generation PET detector module were performed in this section. All timing measurements were done in coincidence with a single-pixel SiPM-J (MicroFJ-30035-SMA). The SiPM-J pixel is referred to as the *reference detector*, since it will be used to determine the CTR for other detectors, and its' CTR has already been characterized.

Any system CTR measurement is a combination of the *single-ended CTR* of the individual detectors that absorbed the annihilation photon pair:

$$CTR = \sqrt{CTR_{SE,det1}^2 + CTR_{SE,det2}^2} \tag{6.1}$$

where $\mathrm{CTR}_{SE,det1}$ and $\mathrm{CTR}_{SE,det2}$ are the single-ended CTR of each detector in coincidence. Given that each detector for the baseline measurements were the same, Equation 6.1 can be rearranged to solve for the single-ended CTR of each single-pixel detector ($\mathrm{CTR}_{SE,pixel}$):

$$CTR_{SE,pixel} = \frac{CTR}{\sqrt{2}} \tag{6.2}$$

For the SiPM-J pixel coupled to a Teflon-wrapped 3×3×3 Proteus LYSO:Ce pixel and read out with the NIM acquisition system, single-ended CTR is:

$$CTR_{SE,pixelJ} = \frac{239\ ps}{\sqrt{2}} \tag{6.3}$$

$$= 169\ ps \tag{6.4}$$

Finally, the single-ended CTR of any detector module in coincidence with the SiPM-J pixel can be calculated by combining and rearranging Equations 6.1 & 6.3:

$$CTR_{SE,det} = \sqrt{CTR^2 - CTR^2_{SE,pixelJ}} \tag{6.5}$$

$$= \sqrt{CTR^2 - (169\ ps)^2} \tag{6.6}$$

Equation 6.6 allows for direct comparison of CTR between detector modules by removing the single-ended CTR contribution of the single-pixel SiPM-J.

6.1.2 Materials

Timing performance of four photodetector arrays was evaluated (Figure 6.1.1): SensL B-Series SPMArray4B (SiPM-B), SensL C-Series ArrayC-30035-16P-PCB (SiPM-C), SensL J-Series ArrayJ-30035-16P-PCB (SiPM-J), and Hamamatsu S13361-3050AE-04 (MPPC). These photodetectors consist of an array 4×4 of SiPM pixels, each with active surface area

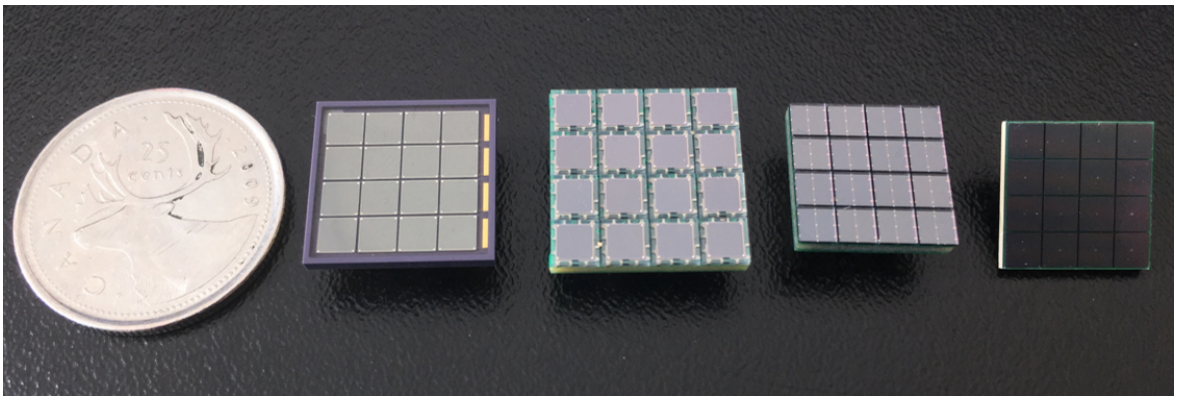

Figure 6.1.1: Left to right: The SiPM-B, SiPM-C, SiPM-J, and MPPC arrays, with a quarter for size reference. The SiPM-B, SiPM-J, and MPPC pixel pitch are all ∼3 mm, while the SiPM-C pixel pitch is 4.2 mm.

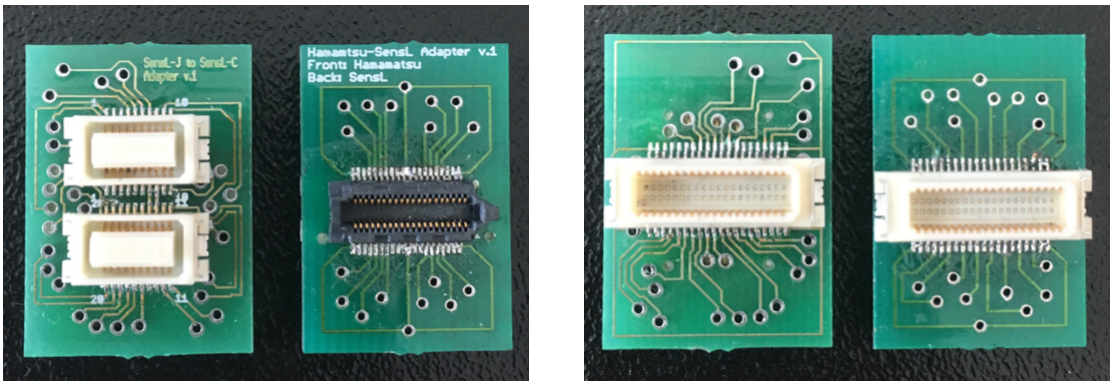

(a) (b)

Figure 6.1.2: PCB adapter boards. (a) Front side of adapter boards, with SiPM-J (left) and MPPC (right) input connectors. (b) Back side of adapter boards with SiPM-C connectors.

of ∼3×3 mm^2 and output to conventional anode and cathode connections (i.e. 'standard' outputs). The SiPM-C and SiPM-J pixels have an additional fast output connection. For more information on these photodetectors, refer to Section 2.4.3 and Table 2.4.2.

LYSO:Ce arrays were constructed in-house with 4×4×4 mm^3 Midas crystals. Crystals were separated with inter-crystal air-gaps (i.e. no coupling or wrapping of individual crystals). ESR was glued to the sides and top of the LYSO:Ce using Dymax OP-20 optical adhesive (Dymax Corporation, Torrington, CT), while the bottom LYSO:Ce face was left bare for scintillator-SiPM coupling. Due to differences in SiPM pixel pitch, two sizes of arrays were constructed: two 4×4 LYSO:Ce arrays to couple to the SiPM-C arrays, and two 3×3 LYSO:Ce arrays to couple to the SiPM-B, SiPM-J, and MPPC arrays.

The second-generation detector readout board was designed to read in two PCB SiPM-C arrays. Modifications to the detector board were made to facilitate readout of SiPM-J and MPPC arrays. Custom adapter PCB boards were designed using Autodesk EAGLE software (Autodesk, San Rafael, CA), manufactured by AP Circuits (Calgary, AB), and assembled in-house. The adapter boards are shown in Figure 6.1.2. PCB female connectors for SiPM-J and MPPC input were soldered on the front while the SiPM-C PCB male connectors were soldered on the back. Standard output pins (and fast output pins for SiPM-J) were routed to their appropriate locations such that SiPM-J/MPPC pixel input had the same spatial layout as the SiPM-C pixels. Pin-rerouting was particularly important to preserve positional information of the charge-division multiplexing circuit. On the detector readout board itself, several 50V-rated capacitors were replaced with 100V-rated capacitors because MPPCs require over 50 V bias. These adaptations/modifications allowed for SiPM-C equivalent readout of SiPM-J and MPPC arrays using the same detector readout board.

As briefly discussed in Section 3.1.2, the detector readout boards have three options for fast output readout: two unamplified 'banks' Fast_B1 and Fast_B2 (referred to as 'Fast_Bs'), one on-board amplified Fast_Out, and Schottky diode output. The Schottky diode output was not investigated in this work. The Fast_Bs and Fast_Out can be toggled by simply adding or removing two 0 Ω series resistors downstream from the Fast_B outputs. Simplified schematics of the Fast_Bs and Fast_Out readout configurations are shown in Figure 6.1.3.

6.1.3 Methods

6.1.3.1 SiPM-C measurements

SiPM-C arrays were coupled with 0.508 mm GPA double-sided tape to the 4×4 Midas LYSO:Ce arrays for approximate one-to-one coupling. The reference detector was a SiPM-J single-pixel (MicroFJ-SMA-30035) coupled with SiG to a Teflon-wrapped 3×3×3 mm^3

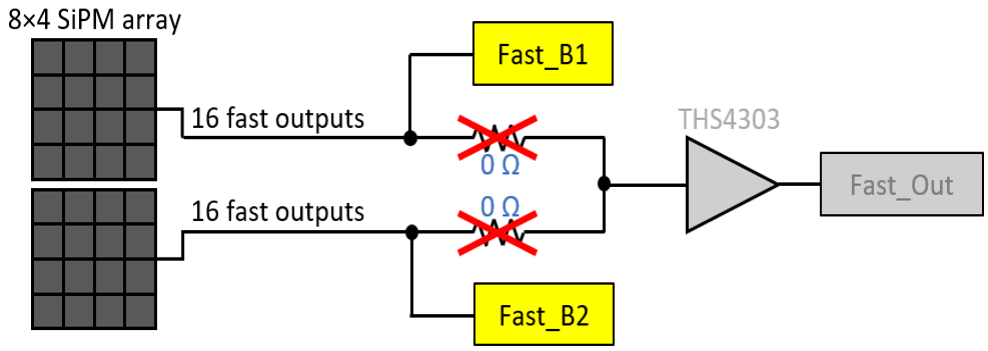

(a)

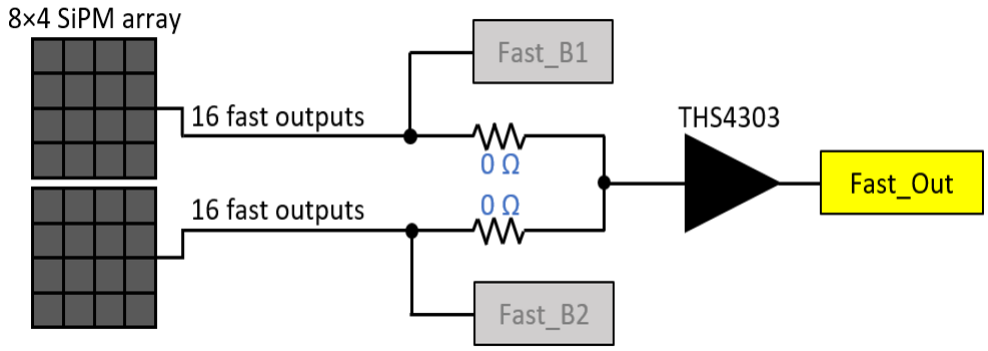

(b)

Figure 6.1.3: Simplified schematic of fast output readout board. (a) Two downstream 0 Ω series resistors are removed for Fast_B1 and Fast_B2 readout. This readout requires external amplification. (b) By adding the 0 Ω series resistors, all 32 fast outputs are summed, amplified with an on-board Texas Instruments THS4303 op-amp, and transmitted via Fast_Out SMA connection.

Proteus LYSO:Ce pixel. The reference detector fast output was amplified with a Mini-Circuits ZFL-1000LN+ amplifier. The optimum LED thresholds were determined to be 8 mV and 10 mV for the reference detector and array detector, respectively. The detector readout board and reference detector SMA board were placed in coincidence by mounting them to a 3D-printed support (Figure 6.1.4). The support was placed in a light-tight box. A $\sim$50μCi ^{22}Na source embedded in a 10×10×10 mm^3 acrylic cube was placed on a stage directly in front of the reference detector. At least 3×10^5 coincidence events were obtained for each measurement.

The NIM acquisition system was set up as described in Section 3.2.1 with a few differences. Both the Fast_Bs and Fast_Out timing readout options were used. When using the Fast_Out, LED TTL outputs from the array and reference detectors were inverted by

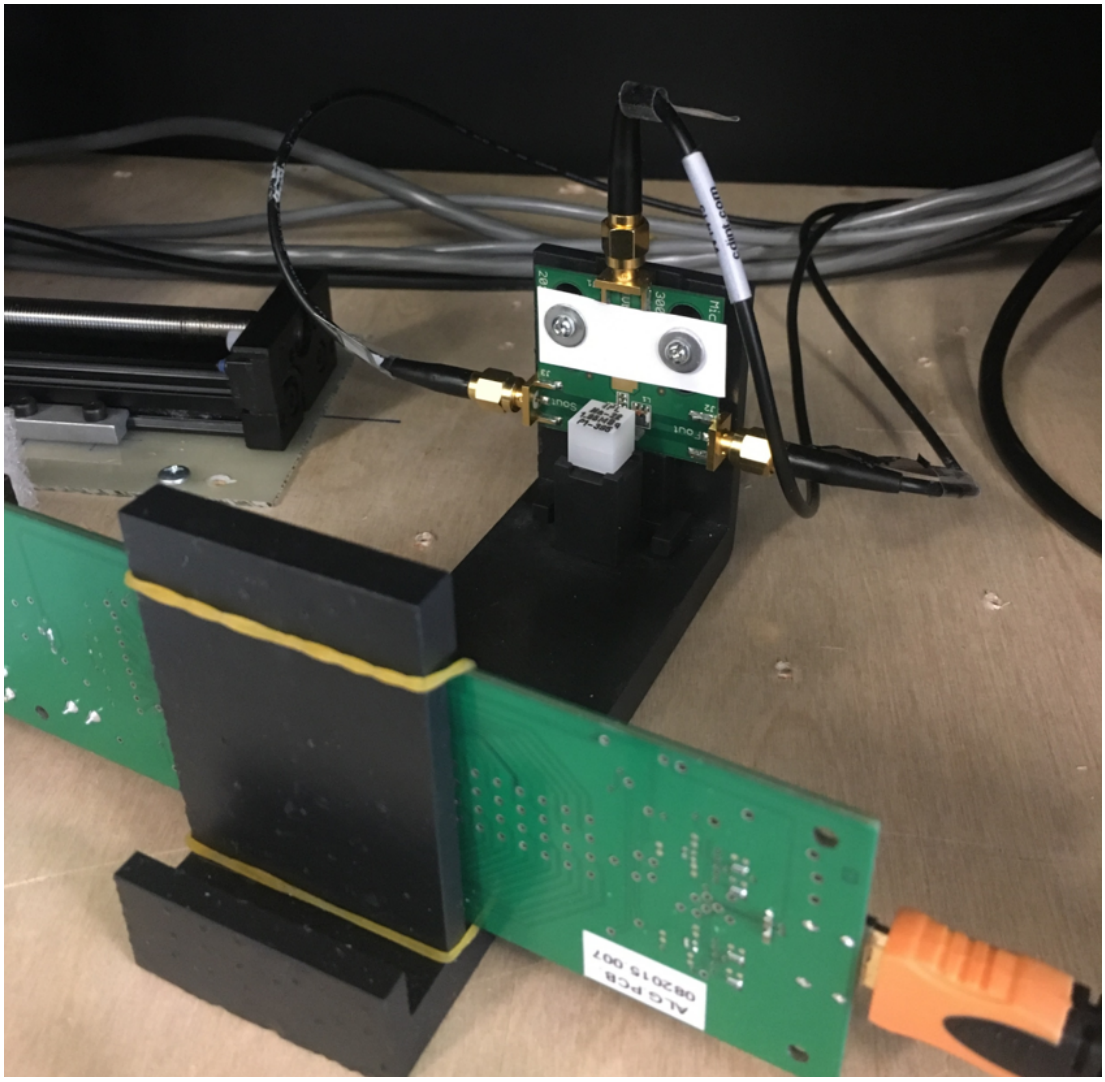

Figure 6.1.4: The detector readout board and reference detector mounted in coincidence. The ^{22}Na acrylic cube was mounted to a stage directly in front of the reference detector.

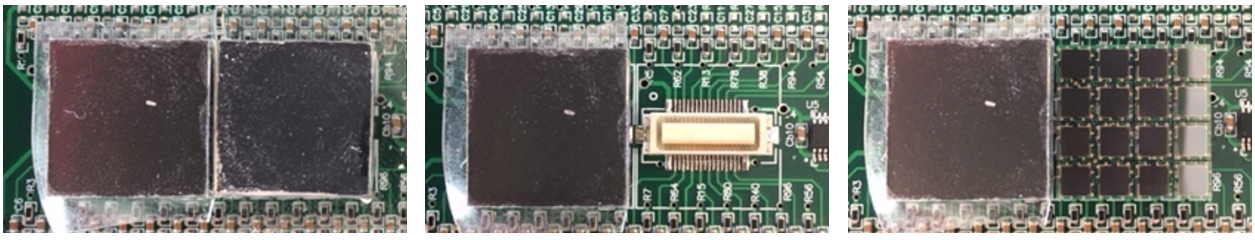

(a) (b) (c)

Figure 6.1.5: SiPM-C array measurements were obtained with three detector-scintillator arrangements: (a) two SiPM-C arrays attached, each coupled with a LYSO:Ce array, (b) one SiPM-C array attached, coupled with a LYSO:Ce array, and (c) two SiPM-C arrays attached, only one coupled with a LYSO:Ce array.

a Phillips Scientific Model #460 inverting transformer then fed into the Phillips Scientific Model 756 logic unit set to coincidence mode. When using the Fast_Bs, each array fast output was amplified by a Mini-Circuits ZX60-4016-S+ amplifier before being fed into the LED. LED TTL outputs from Fast_B1 and Fast_B2 were input to the logic unit set to singles mode to generate an array TTL whenever either of the Fast_Bs produce a TTL. The array TTL and the reference detector fast output LED TTL was input into another logic unit set to coincidence mode. For both readout cases, the reference detector served as the TAC start while the array outputs served as the TAC stop. The TAC was set to R200 (with a calibration factor of 20.3828 ns/V).

Three detector-scintillator arrangements were used and are shown in Figure 6.1.5. For the Fast_Bs and Fast_Out measurements, the effect of attaching one or two SiPM-C/LYSO:Ce arrays was investigated by using the arrangements shown in Figure 6.1.5a & 6.1.5b. Additionally, one measurement with the Fast_Out was obtained with two SiPM-C arrays attached but only one LYSO:Ce coupled, as shown in Figure 6.1.5c. Thus, a total of five CTR measurements were obtained.

Data were processed in the PETDetectorAnalysis.m MATLAB software. Events were filtered with a 400/650 keV energy window on both the array and reference detector data. All measurements were analyzed on a pixel-by-pixel basis. Pixel-averaged energy resolution (E_{res}) was obtained from a Gaussian-plus-line fit of the energy histograms, while timepeak position and CTR were obtained from a single Gaussian fit of the time histograms. The time dispersion (σ_t) between pixels of the SiPM-C arrays was estimated by calculating the standard deviation of the timepeak position.

6.1.3.2 Comparison of SiPM-B, SiPM-C, SiPM-J, and MPPC

Timing measurements of the SiPM-B, SiPM-C, SiPM-J, and MPPC arrays were obtained. Table 6.1.1 summarizes the detector setups. SiPM-C detectors were coupled to 4×4 Midas LYSO:Ce arrays while the SiPM-B, SiPM-J, and MPPC arrays were all coupled with 3×3 Midas LYSO:Ce arrays. Optical coupling was done with 1.016 mm thick GPA tape. The SiPM-B arrays were read out with the first-generation readout board, while the SiPM-C, SiPM-J, and MPPC arrays were read out with the second-generation readout board. Note the SiPM-J and MPPC arrays required the adapter PCB boards for readout. The bias and LED threshold for each detector was optimized by performing preliminary CTR measurements and are given in Table 6.1.1. Coincidence events were triggered off the standard outputs for the SiPM-B and MPPC arrays, and triggered off the Fast_Bs of the SiPM-J. SiPM-C array measurements were done twice, once with standard output triggering and once with Fast_B triggering.

When using array standard output coincidence triggering, the multiplexed A-D energy signals were first summed into the Phillips Scientific Model 740 linear fan in/out, then fed into the LED. The standard output TTL and reference detector fast output TTL were input into the logic unit set to coincidence for event triggering. When using array fast outputs for coincidence triggering, the Fast_Bs were amplified by Mini-Circuits ZX60-4016-S+ amplifiers then fed to the LED. Fast_B LED TTLs were input to the logic unit set to singles mode which outputs an array TTL whenever either of the Fast_B outputs produced a trigger.

Table 6.1.1: Detector setups for CTR comparison between SiPM-B, SiPM-C, SiPM-J, and MPPC.

Detector	Pixel pitch (mm)	Scint. array	Readout board	Bias (V)	Master trigger	LED thres. (mV)
SiPM-B	3.36	3×3	1st gen.	28.5	Standard	50
SiPM-C	4.2	4×4	2nd gen.	29.0	Standard	10
SiPM-C	4.2	4×4	2nd gen.	29.0	Fast	10
SiPM-J	3.36	3×3	2nd gen.	30.0	Fast	10
MPPC	3.2	3×3	2nd gen.	54.25	Standard	15

Table 6.1.2: Energy and timing results of SiPM-C 4×4 and 8×4 arrays using Fast_Bs and Fast_Out readout. Total CTR is given (i.e. of the single pixel and array detectors together). Uncertianties were calculated as the standard deviation of values across all pixels.

Readout	# SiPM arrays	# LYSO:Ce arrays	E_{res} (%)	σ_t (ps)	CTR (ps)
Fast_Bs	1	1	13.6 ± 2.0	155	437 ± 26
Fast_Bs	2	2	13.5 ± 1.8	206	425 ± 33
Fast_Out	1	1	13.6 ± 2.0	155	438 ± 26
Fast_Out	2	2	13.5 ± 1.8	276	724 ± 66
Fast_Out	2	1	13.3 ± 1.6	172	647 ± 44

Then, the array TTL and reference detector fast output TTL were then input to a logic unit set to coincidence mode.

For each detector, two arrays were attached to the readout board to make an 8×4 pixel array (i.e. the same arrangement as Figure 6.1.5a). Arrays were mounted to the 3D printed support. The reference detector was a SiPM-J single-pixel (MicroFJ-SMA-30035) coupled with SiG to a Teflon-wrapped 3×3×3 mm^3 Proteus LYSO:Ce pixel. The reference detector fast output was amplified by a Mini-Circuits ZFL-1000LN+ amplifier and input into the LED with an 8 mV threshold setting. The ∼50 μCi ^{22}Na point source was placed directly in front of the reference detector. At least 3×10^5 coincidence events were obtained for each detector.

Output data were processed on a per-crystal basis using the PETDetectorAnalysis.m software. For each crystal, energy histograms were constructed and fit with a Gaussian-plus-line function. A global 400-650 keV energy window was applied. Time histograms were constructed and fit with a single Gaussian function. Per-crystal energy resolution, time dispersion, and CTR was obtained.

6.1.4 Results

6.1.4.1 SiPM-C measurements

Table 6.1.2 gives the energy and timing results of the SiPM-C array measurements. Energy resolution was within 13.3 % - 13.6 % for all measurements. Time dispersion was 155 ps for both cases where one SiPM-C array was attached, but degraded to 172 ps - 276 ps for the other detector-scintillator coupling cases. The Fast_B CTR was 437 ± 26 ps and 425 ± 33 ps when reading out one and two SiPM-C arrays, respectively. For the Fast_Out, CTR was 438 ± 26 ps when reading out one SiPM-C array, which degraded to 647 ± 44 ps and 724 ± 64 ps when reading out two SiPM-C arrays with one and two LYSO:Ce arrays, respectively.

6.1.4.2 Comparison of SiPM-B, SiPM-C, SiPM-J, and MPPC

Table 6.1.3 gives the energy resolution, time dispersion, and CTR for each array measurement. Energy resolution was 12.1 % - 14.7 % for the SiPM-B and SiPM-C detectors, and 8.6 % - 9.5 % for the SiPM-J and MPPC detectors. Time dispersion was 644 ps for the SiPM-B and between 192 ps - 306 ps for the other detectors. CTR was 1847 ± 141 ps and 806 ± 86 ps for SiPM-B and SiPM-C standard output triggering, respectively. The CTR of the SiPM-C fast output, SiPM-J fast output, and MPPC standard output was 425 ± 33 ps,

Table 6.1.3: Results of SiPM-B, SiPM-C, SiPM-J, and MPPC array timing measurements. Uncertainties of energy resolution and coincidence time resolution were calculated as their standard deviations across all 32 pixels, while time dispersion was the standard deviation of the timepeak position. Single-ended CTR was calculated using Equation 6.6.

Detector	Master trigger	E_{res} (%)	σ_t (ps)	CTR (ps)	CTR_{se} (ps)
SiPM-B	Standard	12.1 ± 0.7	644	1847 ± 141	1839 ± 140
SiPM-C	Standard	14.7 ± 1.0	192	805 ± 86	787 ± 84
SiPM-C	Fast	13.5 ± 1.8	206	425 ± 33	390 ± 30
SiPM-J	Fast	9.5 ± 0.4	286	438 ± 29	404 ± 27
MPPC	Standard	8.6 ± 0.4	306	434 ± 26	400 ± 24

438 ± 30 ps, and 435 ± 26 ps, respectively. Flood histograms for each detector are shown in Figure 6.1.6. For the crystals circled in blue, energy histograms and time histograms are generated in Figure 6.1.7 and Figure 6.1.8, respectively.

6.1.5 Discussion

6.1.5.1 SiPM-C measurements

The SiPM-C measurements showed consistent energy resolution regardless of how many arrays were attached or what method of fast output readout was used. Event positioning is calculated from standard output data, and therefore fast output configuration does not have a significant impact on energy information. Similar energy resolution between one and two attached SiPM-C arrays indicate that optical coupling between detector-scintillator was consistent for both SiPM-C arrays.

Time dispersion was minimized when only one SiPM-C array was attached, regardless of the fast output configuration. However, time dispersion is increased when attaching a second SiPM-C array. When both SiPM-C arrays were coupled with LYSO:Ce arrays, time dispersion was 206 ps and 276 ps for the Fast_Bs and Fast_Out, respectively. The benefit of Fast_B readout is that the SiPM-C arrays are decoupled: time signals from one array do not affect the other array. In contrast, the Fast_Out readout couples all of the SiPM-C fast outputs together. Consider the case when Fast_Out was was used with two SiPM-C arrays and only one LYSO:Ce array. Time dispersion degraded from 155 ps to 172 ps when attaching a second SiPM-C array even though no LYSO:Ce array was coupled to it. The increase in time dispersion is because all fast outputs are coupled, and the bare SiPM-C increases the effective capacitance and dark noise of the detector as a whole.

Significant degradation in CTR occurs when using array detectors compared to single-

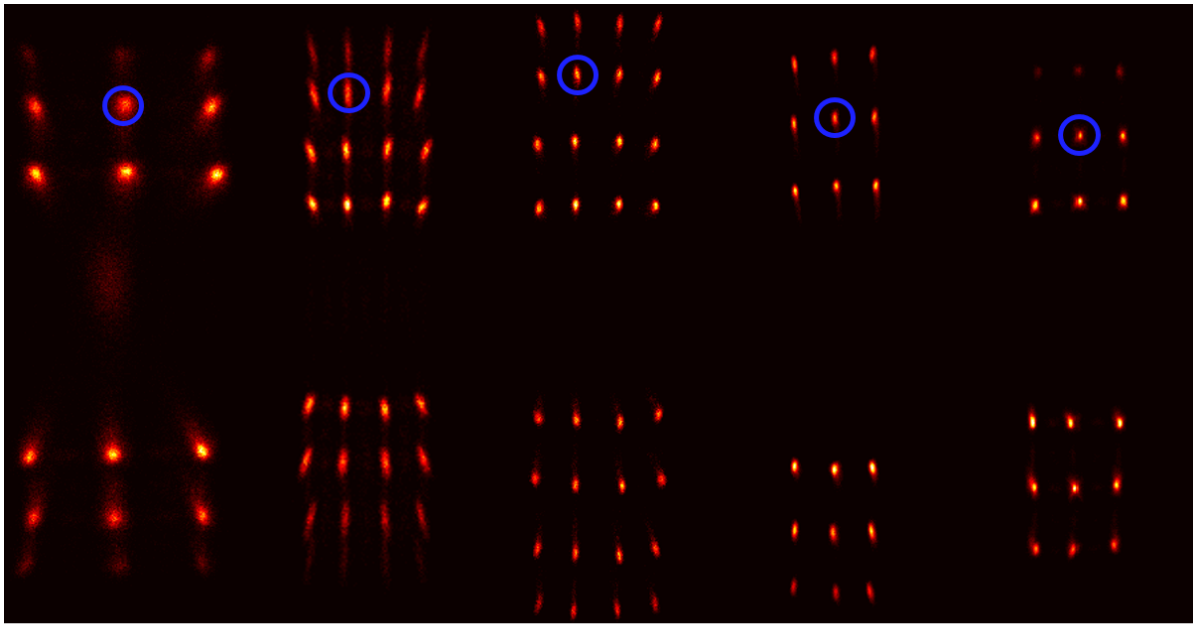

Figure 6.1.6: Flood histograms of the (a) SiPM-B, (b) SiPM-C (standard output triggering), (c) SiPM-C (fast output triggering), (d) SiPM-J, and (e) MPPC arrays. Subsequent energy histogram and time histogram plots are generated from the crystals circled in blue.

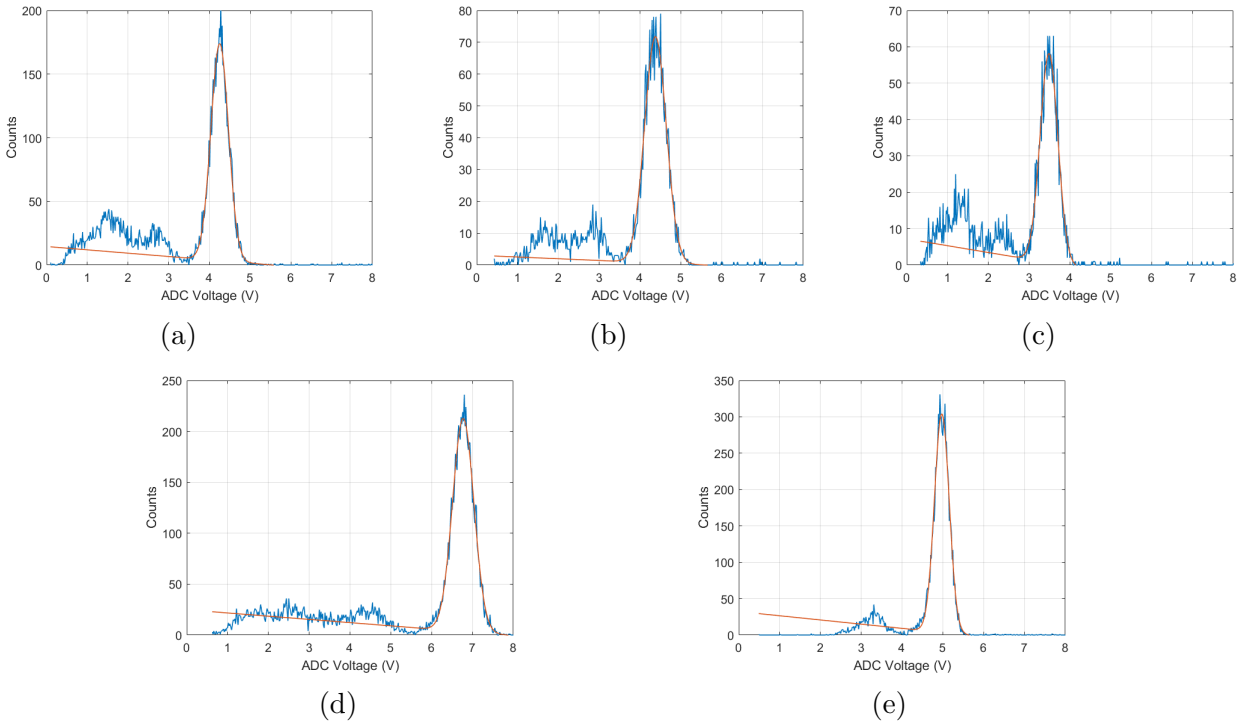

Figure 6.1.7: Energy histograms of (a) SiPM-B, (b) SiPM-C (standard output), (c) SiPM-C (Fast_Bs), (d) SiPM-J, and (e) MPPC. Each histogram was generated for the pixel circled in Figure 6.1.6. Differences in photopeak amplitude are due to differences in SiPM PDE, SiPM bias, LYSO:Ce array size, and ADC gain setting.

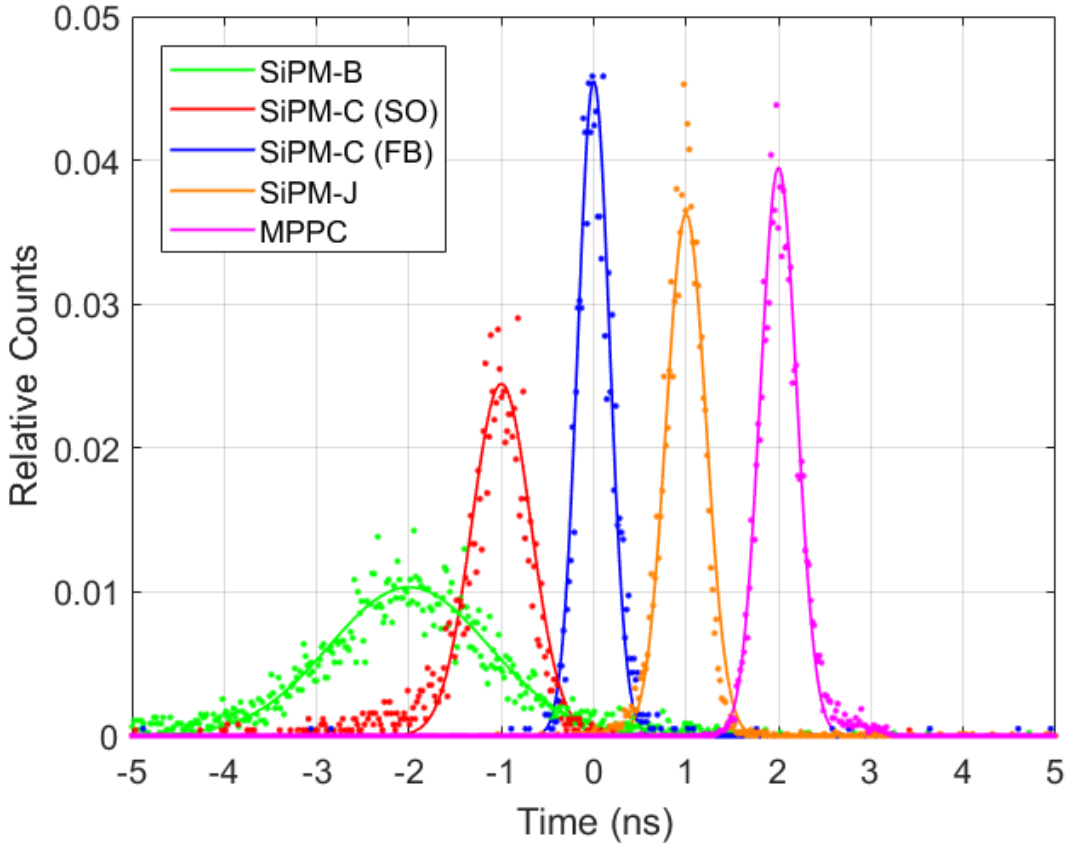

Figure 6.1.8: Time histograms for SiPM-B, SiPM-C (standard output), SiPM-C (Fast_Bs), SiPM-J, and MPPC. Histograms were re-centred at -2, -1, 0, 1, and 2 ns, respectively. Each histogram was generated for the pixel circled in Figure 6.1.6. The y-axis is relative counts, where each bin has been divided by the total counts for each data set. The dots and solid lines are the bin data and single Gaussian fits, respectively.

pixel detectors. Table 6.1.3 lists the single-ended CTR for each detector array measurement, where CTR_{SE} of the SiPM-C arrays was 390 ps. In Section 5.4.3, CTR was 362 ps for two single SiPM-C pixels in coincidence (coupled with Teflon-wrapped 4×4×4 LYSO:Ce Midas crystals), and therefore the single-ended CTR was 362 / $\sqrt{2}$ ps = 256 ps. This single-pixel arrangement is more appropriate to compare with the SiPM-C array measurements because they both use the same SiPM pixel technology and LYSO:Ce Midas crystals. Clearly, the SiPM-C array contributes the majority of CTR degradation when put on coincidence with a single-pixel. Light-sharing detector designs with signal coupling and/or multiplexing degrades CTR because light collection is not optimal and photon statistics suffer [57]. Even though the detector setup in these measurements are 4×4 LYSO:Ce coupled to 4×4 SiPM-C

arrays with similar pitch, this design is still considered to be light sharing because of optical photon diffusion in the GPA tape layer. For array detectors, physical coupling of output signals by multiplexing causes undesired shaping effects through added capacitance, dark noise, and crystal cross talk [57]. Additionally, there are likely subtle differences gain and signal path length between individual SiPM-C pixels.

CTR degradation with signal coupling is further demonstrated when comparing 4×4 and 8×4 arrays measurements. Since SiPM arrays are decoupled when using the Fast_Bs, CTR was not significantly different when reading out one and two SiPM-C arrays. However, the Fast_Out readout cases demonstrate the effect of adding another coupled SiPM array. CTR degraded from 438 ps to 647 ps when adding a second SiPM-C array even though it was not coupled with a LYSO:Ce array. Again, this is because the effective capacitance and dark noise of the entire module is increased.

Another difference between the Fast_B and Fast_Out readouts was signal amplification. The Fast_B outputs used external Mini-Circuits ZX60-4016-S+ amplifiers which have a bandwidth up to 4 GHz. However, the Fast_Out used the on-board Texas Instruments THS4303 op-amp which a bandwidth up to 1.8 GHz. The difference in bandwidth between amplifiers had little consequence since CTR was not significantly different between Fast_B and Fast_Out readouts with one SiPM-C array. This was worth investigating because baseline timing measurements showed degraded CTR when using 1 GHz bandwidth RG-58 transmission cables.

6.1.5.2 Comparison of SiPM-B, SiPM-C, SiPM-J, and MPPC

Energy resolution was poorest for the SiPM-C arrays due to the difference in pixel pitch. Since pixel pitch is 4.2 mm for the SiPM-C arrays and 3.2 - 3.36 mm for the other arrays, the increase in dead space between pixels results in light loss which degrades energy resolution.

Energy resolution was 12.1 %, 9.5 %, and 8.6 % for the SiPM-B, SiPM-J, and MPPC, respectively. These variations are likely due to differences in photon detection efficiency, where PDE of 420 nm is 31 % and 38 % for SiPM-B and SiPM-J, respectively, and PDE of 450 nm is 40 % for MPPC. Differences in energy resolution may also be due to difference in detector gain and in optical coupling quality.

Time dispersion was 644 ps for SiPM-B, which was over a factor of two greater than the values for the other detectors. When the first-generation PCB detector readout board was designed, the signal path length between pixel standard outputs was not considered. Therefore, time dispersion is likely due to differences in arrival times of standard output signals to the multiplexing circuit. Increased time dispersion may be due to differences in signal paths of individual pixels in the SiPM-B array itself. Time dispersion degraded from ∼200 ps to ∼300 ps for the SiPM-C and the SiPM-J/MPPC detectors, respectively, since the latter required PCB adapter boards to reroute anode and SensL fast outputs, and signal path length was not considered when designing these boards.

Single-ended CTR data in Table 6.1.3 may be used to estimate the total CTR of a full ring system. Theoretically, the total CTR of two detector modules in coincidence is the root sum of the square of single-ended CTR (i.e. CTR = $\sqrt{2}\ CTR_{SE}$). Therefore, CTR of a PET system with the SiPM-B, SiPM-C standard output, SiPM-C Fast_B outputs, and MPPC are 2600 ps, 1110 ps, 550 ps, and 570 ps, respectively.

CTR between SiPM-B and SiPM-C standard output triggering improved, likely due to enhancements between SiPM generations and detector readout board generations. Within their standard deviations, the CTR of SiPM-C (fast), SiPM-J (fast), and MPPC (standard) were not statistically different. This was expected for the SiPM-C and SiPM-J fast outputs, since the primary differences between these SiPM generations are in microcell number and sensitivity range. The SiPM-C arrays may have had slightly better CTR than the SiPM-J arrays because a larger scintillator array volume was used per unit area of sensitive SiPM

volume, leading to better photon statistics. However, the MPPC arrays performed just as well despite not having dedicated fast outputs.

6.1.6 Conclusion

Coincidence time resolution was improved by using an enhanced second-generation detector readout board with either SiPM-C, SiPM-J, or MPPC readout. The best CTR was obtained using the SiPM-C fast output. However, the first-generation PET insert currently uses the OpenPET system for data acquisition which requires modifications before additional signals can be processed. As it stands, the OpenPET system only reads in the conventional anode signals for energy and timing information. CTR was still improved when using the standard outputs of the SiPM-C, which can be credited to improvements in the multiplexing circuit of the second-generation readout board. The MPPC standard output had nearly the same CTR as the SiPM-C Fast_Bs, but their use required further modifications to the second-generation detector readout board.

6.2 Signal Duration

6.2.1 Introduction

In Section 3.3.5, it was stated that the first-generation PET insert had a relatively long signal duration of >1.5 μs and a paralyzable dead time of ∼1.3 μs. Both can be reduced by using a photodetector with a low time constant (Equation 3.19). In this section, signal duration was evaluated using OpenPET waveform capture of the standard output signals from the SiPM-B, SiPM-C, and MPPC detectors. Shorter signal durations will reduce pileup effects and the paralyzable component of dead time.

6.2.2 Materials

Three photodetectors were used in this section: the SiPM-B (SPMArray4B), SiPM-C (ArrayC-30035-PCB-16P), and MPPC (S13361-3050AE-04). Details on these detectors were given in Table 2.4.2. Perhaps the most relevent detector property in this section is terminal capacitance, which is 850 pF, 850 pF, and 320 pF for SiPM-B, SiPM-C, and MPPC, respectively. SiPM-J arrays were not tested in this section since the SiPM-C and SiPM-J array technology is similar and the SiPM-J capacitance of 1000 pF is slightly higher than the SiPM-C capacitance. The MPPC array has the lowest terminal capacitance and microcell number of the detectors tested, leading to a lower time constant (Equation 3.19). Therefore, the MPPC is expected to have the shortest signal duration and least pileup effects.

The scintillators used were the single-layer 4×4 and 3×3 arrays of 4×4×4 mm^3 Midas LYSO:Ce crystals. These arrays were constructed in-house with inter-crystal air gaps and outer ESR wrapping. Due to differences in pixel pitch, the SiPM-C arrays were coupled with 4×4 LYSO:Ce arrays while the SiPM-B and MPPC arrays were coupled with 3×3 LYSO:Ce arrays. Optical coupling was done with 1.016 mm GPA tape. Two SiPM/MPPC arrays were attached for each measurement (i.e. 8×4 arrays of one-to-one coupled LYSO:Ce-SiPM pixels).

SiPM-B arrays were read out with the first-generation PCB detector readout boards while the SiPM-C and MPPC arrays were read out with the second-generation detector readout boards. MPPC arrays were input using PCB adapter boards which rerouted pin outputs for SiPM-C equivalent readout. Additionally, several 50V-rated capacitors on the MPPC detector readout board were swapped out for 100V-rated capacitors due to the >50 V MPPC bias requirement.

6.2.3 Methods

Photodetectors were placed one at a time in a light-tight box along with a ∼4.3 MBq ^{68}Ge rod source. Waveform captures were obtained using the OpenPET system using a 30 mV LED threshold. For each triggered event, 256 samples/event for each of the four multiplexed standard outputs were captured by the ADC at 40 MHz (i.e. 25 ns/sample). Several hundred events were obtained for the SiPM-B, SiPM-C, and MPPC detectors. Signal duration was calculated as the time above 10 % of the maximum signal amplitude. For each detector, signal durations were histogrammed into 25-ns-size bins, and the true signal duration was taken as the mean plus/minus the standard deviation ($\mu \pm \sigma$ in Equation 3.12).

6.2.4 Results and discussion

Standard output waveform captures from the OpenPET system are shown in Figure 6.2.1. Signal durations were 1850 ± 150 ns, 600 ± 25 ns, and 350 ± 25 ns for SiPM-B, SiPM-C, and MPPC, respectively. Note the presence of signal undershoot for the SiPM-C and MPPC detectors, which peaks at ∼50 mV below baseline and slowly recovers over several microseconds. Unlike the first-generation readout board, the second-generation readout boards have 10 nF capacitive coupling of the standard anode outputs which causes signal undershoot (described in [47]).

Improvement of signal duration was demonstrated by choice of photodetector and by enhancements to the detector readout board. The MPPC arrays had the shortest signal duration, since it had a lower capacitance and lower microcell number than the other photodetectors. However, signal duration was significantly better for SiPM-C versus SiPM-B despite the fact that both have the same terminal capacitance and microcell number. This improvement is due to the detector readout boards used. The first-generation readout board

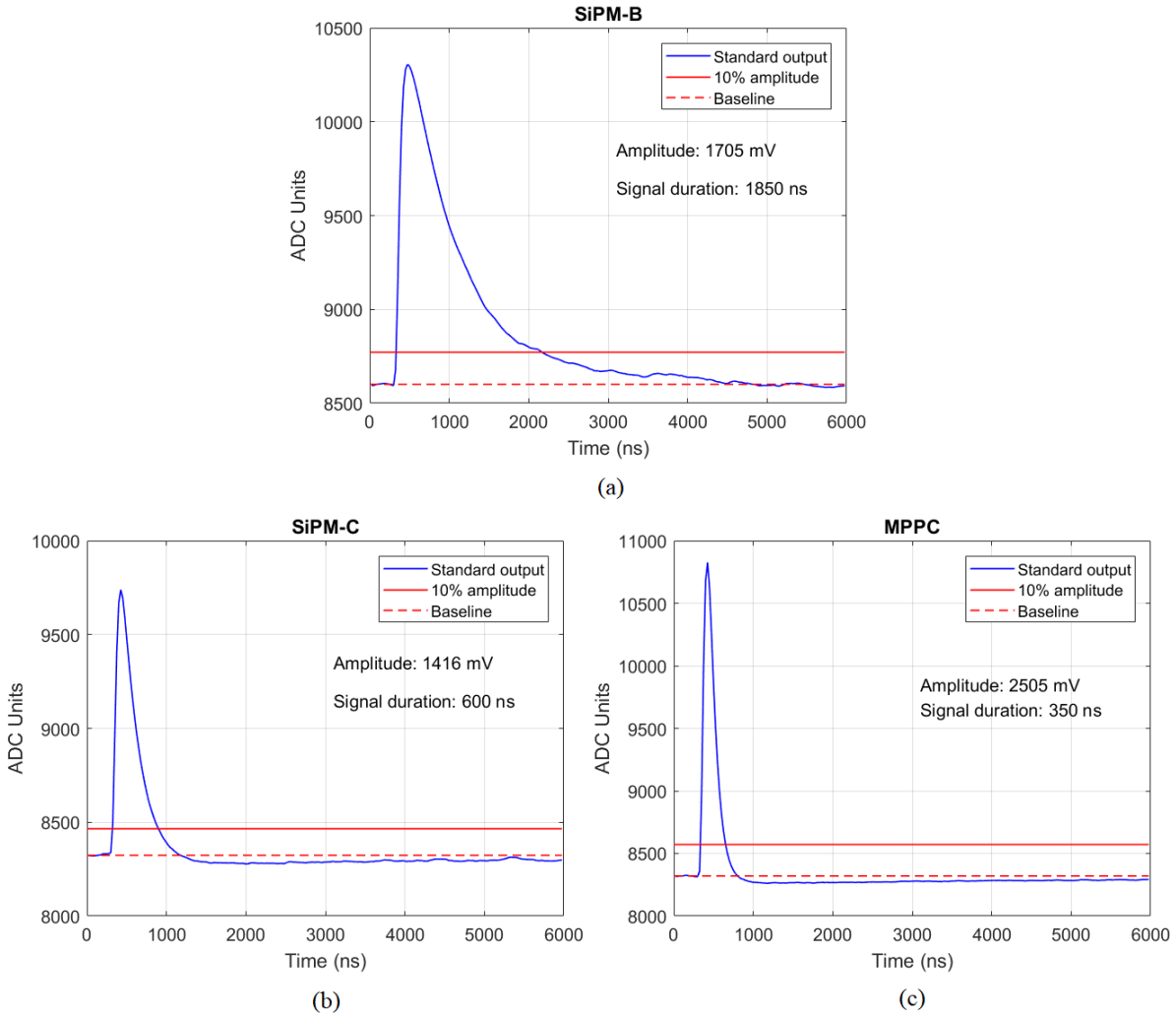

Figure 6.2.1: Waveform capture of (a) SiPM-B, (b) SiPM-C, and (c) MPPC standard outputs using the OpenPET system.

had greater resistor values in the resistor based charge division multiplexing circuit, which increases the time constant and signal decay time. In the second-generation readout board, the resistance of the multiplexing network was reduced and therefore the signal duration decreased.

These waveform captures are insightful because they represent true waveforms that the OpenPET system analyzes for signal digitization. From these waveform samples, downstream OpenPET components calculate signal amplitude as peak minus baseline and digitize these values for each of the four multiplexed outputs. The longer the signal duration, the more probable that a pileup event will occur. If two radiation events occur in rapid suc-

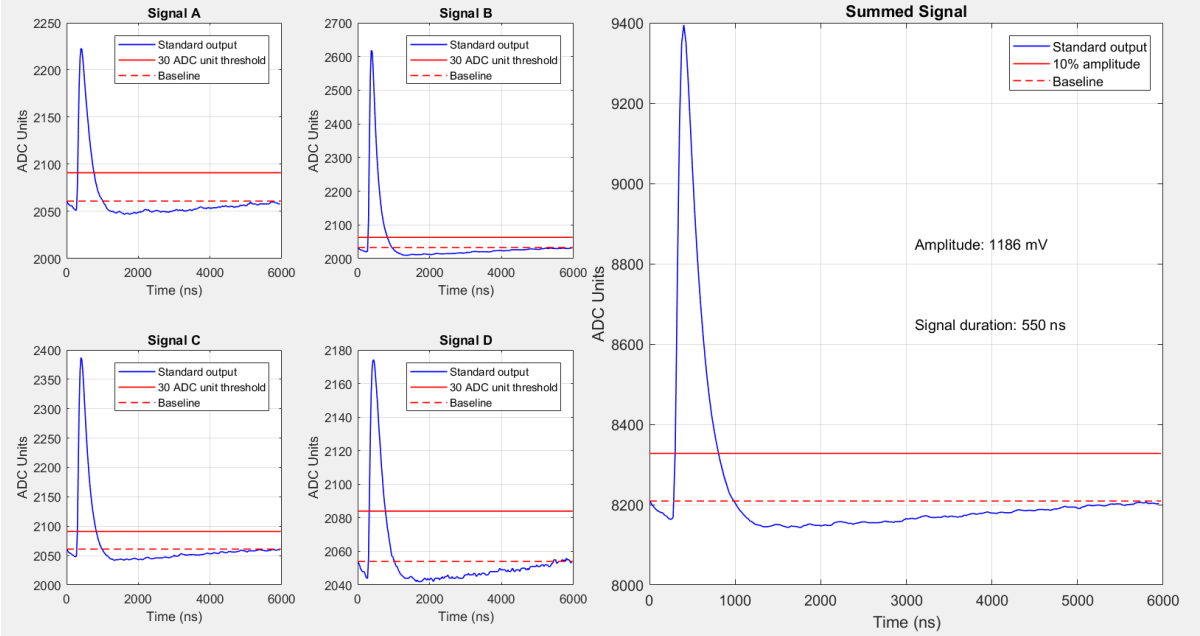

Figure 6.2.2: Waveform capture of an event that is affected by a previous event using the SiPM-C detector and OpenPET acquisition system. At the beginning of this signal, it appears that some microcell discharge is still occurring from a previous event. The baseline is set too high as a result, and the peak-minus-baseline signal amplitude is calculated to be lower than its real value. The four left waveforms are the A-D multiplexed standard outputs while the right plot is the summed signal.

cession but with enough time between such that they are recorded as two different events, then the second event will be compromised due to a baseline shift. An example of this is shown in Figure 6.2.2. The baseline (by default) is chosen as the ADC value 12 bins before the trigger occurred. Since this event occurred while the previous event was still undergoing microcell discharge, the baseline of the second event is set artificially high. Signal amplitude is therefore artificially low since the OpenPET system calculates amplitude as peak minus baseline. These events are more likely to occur as count rate increases, so it is expected that photopeak amplitude decreases as count rate increases. This effect may be minimized by taking an average of several pre-trigger ADC values for baseline calculation, however this increases the number of samples required for event digitization which extends the system processing time (i.e. non-paralyzable dead time). Of course, at very high count rates, it becomes increasingly probable that pileup events occur so close in time that multiple events are recorded as a single event, increasing the signal amplitude and the detector recovery

time.

6.2.5 Conclusion

Signal duration of the detector module was reduced by making enhancements to the detector readout board and by using MPPCs which have a relatively low terminal capacitance. This implies that the second-generation detector module will have less pileup effects and improved paralyzable dead time.

6.3 Count Rate Measurements

6.3.1 Introduction

In Section 3.3.5, it was stated that the first-generation PET insert had a paralyzable dead time of $\sim$1.3 μs. The paralyzable component of dead time should be reduced significantly by using the SiPM-C/MPPC arrays with the second-generation readout board because they have a shorter signal duration compared to the SiPM-B with the first-generation readout board. This section focuses on the overall count rate performance of the detector modules. To further minimize count rate losses due to dead time, the non-paralyzable dead time was reduced by adjusting the OpenPET acquisition system firmware. As described in Section 3.3.5, the FPGA ADC takes 32 output pulse samples per event (s/e) by default, which was changed to 22 s/e in order to shorten event processing time. Therefore, the non-paralyzable componenent of the detector module dead time was minimized in order to facilitate higher event rates.

6.3.2 Materials

Three photodetectors were used in this section: the SiPM-B (SPMArray4B), SiPM-C (ArrayC-30035-PCB-16P), and MPPC (S13361-3050AE-04). Details on these detectors were given in Table 2.4.2. Two arrays were attached for each detector type (i.e. 8×4 pixel arrays). Each array was coupled with a Midas LYSO:Ce array (single crystal layer, air-gapped, ESR outer-wrapped) using 1.016 mm GPA tape. SiPM-C arrays were coupled to 4×4 LYSO:Ce arrays while SiPM-B and MPPC arrays were coupled to 3×3 LYSO:Ce arrays. SiPM-B arrays were read out with the first-generation detector readout board while the SiPM-C and MPPC arrays were read out with the second-generation readout boards. MPPC readout required the use of the PCB adapter boards and 100V-rated capacitors.

6.3.3 Methods

All three detectors were secured to the base of a light-tight box with GPA tape. Detectors were covered with a thick black curtain to minimize light leakage. Power was supplied with an Aligent Technologies (Santa Carla, CA) N6700B Low-Profile Modular Power System Mainframe (400 W). SiPM-B, SiPM-C, and MPPC bias was 28.0 V, 28.0 V, and 53.5 V, respectively. These detector biases were chosen because the photopeak was positioned near the centre of the ADC range, which minimizes clipping of pileup events. Detector readout board HDMI outputs were each connected to their own detector interface board and OpenPET detector board. Upon startup, the OpenPET detector boards were calibrated with an event trigger of 30 mV on the standard output. No fast output data were collected.

Three 'decaying source' count rate measurements were obtained, two using 32 s/e and one using 22 s/e ADC capture. The 32 s/e measurement was repeated in order to test reproducibility of the data. For each measurement, an [^{18}F]-FDG sample was secured to

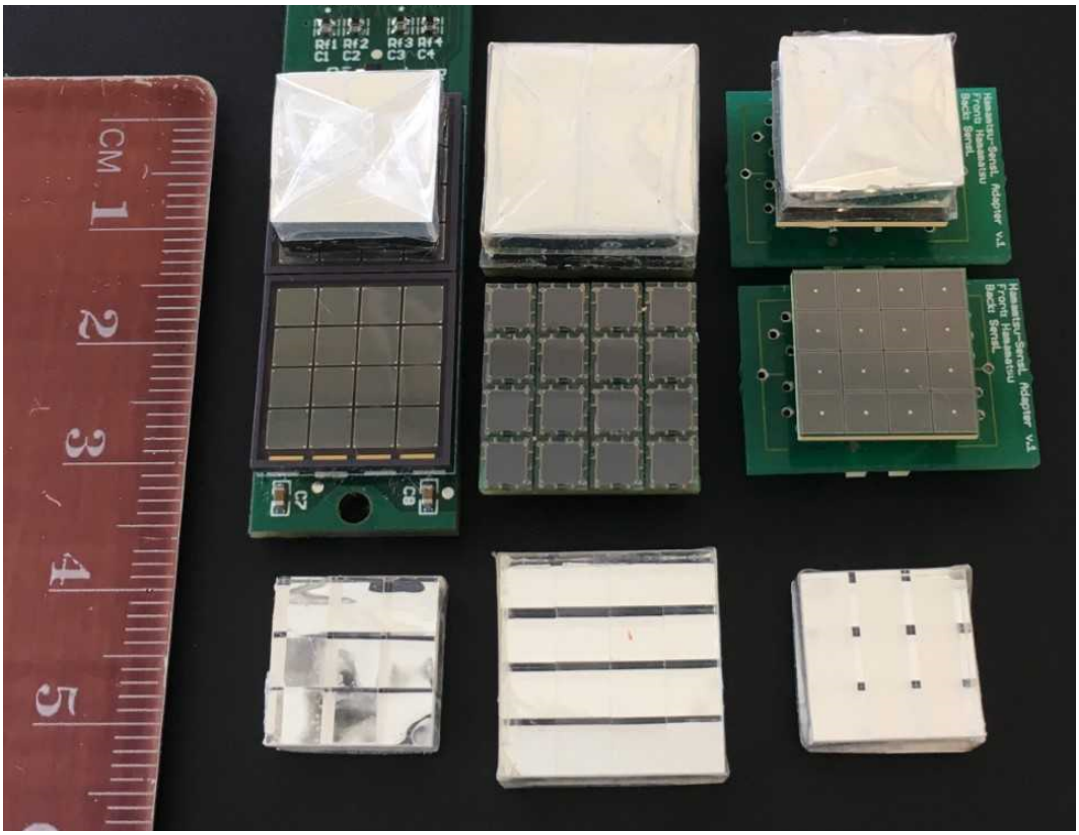

Figure 6.3.1: Detectors and scintillators used for count rate measurements. Left: SiPM-B arrays coupled with 3×3 LYSO:Ce. Centre: SiPM-B arrays coupled with 4×4 LYSO:Ce. Right: MPPC arrays coupled with 3×3 LYSO:Ce.

(a) (b)

Figure 6.3.2: Apparatus of decaying source count rate measurements. (a) Detector readout boards were taped to the wooden base and the [^{18}F]-FDG sample was secured to the 3D printed support with GPA tape. Black curtains were placed over the detectors before the box was closed and the acquisitions were started. (b) The OpenPET chassis. Detector readout board HDMI outputs were input into separate detector interface boards and OpenPET detector boards. The chassis also houses the PC with MATLAB software for calibration and acquisition.

Table 6.3.1: Breakdown of the three acquisition sets for decaying source count rate measurements. A total of 60 acquisitions were obtained over the duration of 21 hours (∼11.5 ^{18}F half-lives). Acquisition duration and delay were increased over time since count rate is reduced as the ^{18}F source decays.

Set #	Acquisition duration (min)	Delay after acquisition (min)	# acquisitions in set	Total time (h)
1	1	9	18	3
2	2	13	12	3
3	5	25	30	15

the 3D-printed support such that it was suspended ∼8 cm above the SiPM-B detectors (Figure 6.3.2a). Data were acquired at set durations and delays, as summarized in Table 6.3.1. Acquisition durations and delays were selected in order to obtain a sufficient number of events for statistical results, yet not an excessive number of events in order to avoid unnecessarily large output files. The support/stepper motor system and the detector readout boards were not moved inside the box throughout all data acquisitions. However, the box itself was transported between measurements, so minute geometrical differences between measurements is possible.

Calibration, data acquisition, and data list-mode conversion were performed using in-house developed MATLAB software. The output list-mode data were then analyzed using the 'PETDetectorAnalysis.m' MATLAB software. Flood histograms and per-crystal energy spectra were obtained for each data set. Energy spectra were fit with a Gaussian-plus-line function, and photopeak amplitude and energy resolution were obtained from the fitting parameters.

Additional MATLAB scripts were used to analyze and fit the count rate data. Observed count rate (m) versus activity plots were generated. 'True event rate' (n) was calculated as a linear extension of the 25 lowest activity acquisitions. Count rate curves were then generated with the true event rate on the abscissa and observed count rate on the ordinate. The data were fit with a paralyzable and a non-paralyzable model which were described in Section 3.3.5.

6.3.4 Results

Figure 6.3.3a and 6.3.3b plot the count rate versus activity and the pixel-averaged energy resolution versus count rate for the repeat 32 s/e ADC capture measurements. No significant difference in count rate and energy resolution was observed. This suggests that a fair comparison between 22 s/e and 32 s/e ADC capture can be made as long as each apparatus is geometrically equivalent.

Count rate versus activity for each detector and ADC capture is plotted in Figure 6.3.4a. There is clear separation in measured count rate between 22 s/e and 32 s/e ADC capture as activity increases. For all detectors, the count rate measured near 500 MBq activity was at least 100 kcps higher for 22 s/e than 32 s/e ADC capture. The SiPM-C detectors reach a higher count rate than the other detectors since it had a higher sensitive volume (i.e. each SiPM-C array was coupled with a 4×4 LYSO:Ce array versus a 3×3 LYSO:Ce array). Figure 6.3.4b shows the same count rate curves, except that SiPM-C activity is multiplied by a factor of 16/9 to account for the relative increase in scintillation volume.

Figures 6.3.4c and 6.3.4d shows the relative change in photopeak amplitude and the energy resolution versus count rate, respectively. Photopeak amplitude decreased as count rate increased, however photopeak amplitude tended to spike at very high count rates. Energy resolution was not significantly different between ADC capture settings for the SiPM-B and MPPC, but was more stable for SiPM-C towards high count rates.

Fitted count rate curves using the non-paralyzable dead time model given in Equation 3.18 are shown in Figure 6.3.5. The non-paralyzable dead time was determined to be 1.3 - 1.4 μs for 22 s/e ADC capture and 1.7 - 1.8 μs for 32 s/e ADC capture.

Several flood histograms are shown in Figure 6.3.6. Pileup effects manifest as crystal 'smearing' in flood histograms. At ∼500 kcps, extensive pileup effects are observed for

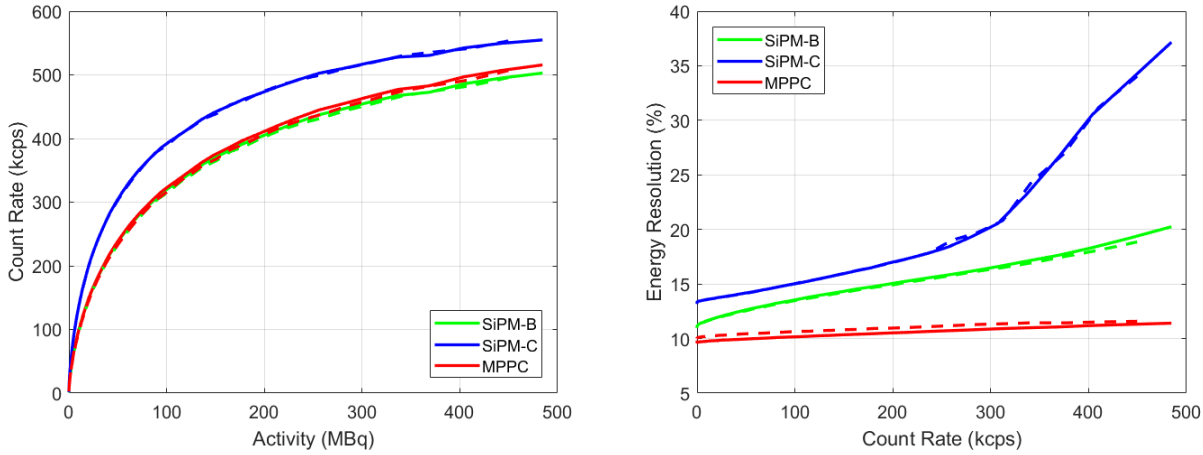

(a) (b)

Figure 6.3.3: (a) Count rate versus activity, and (b) energy resolution versus count rate for two decaying source measurements using 32 s/e ADC capture. Solid and dotted lines represent the first and second measurement set. Very little difference in count rate and energy resolution between repeat measurements is observed.

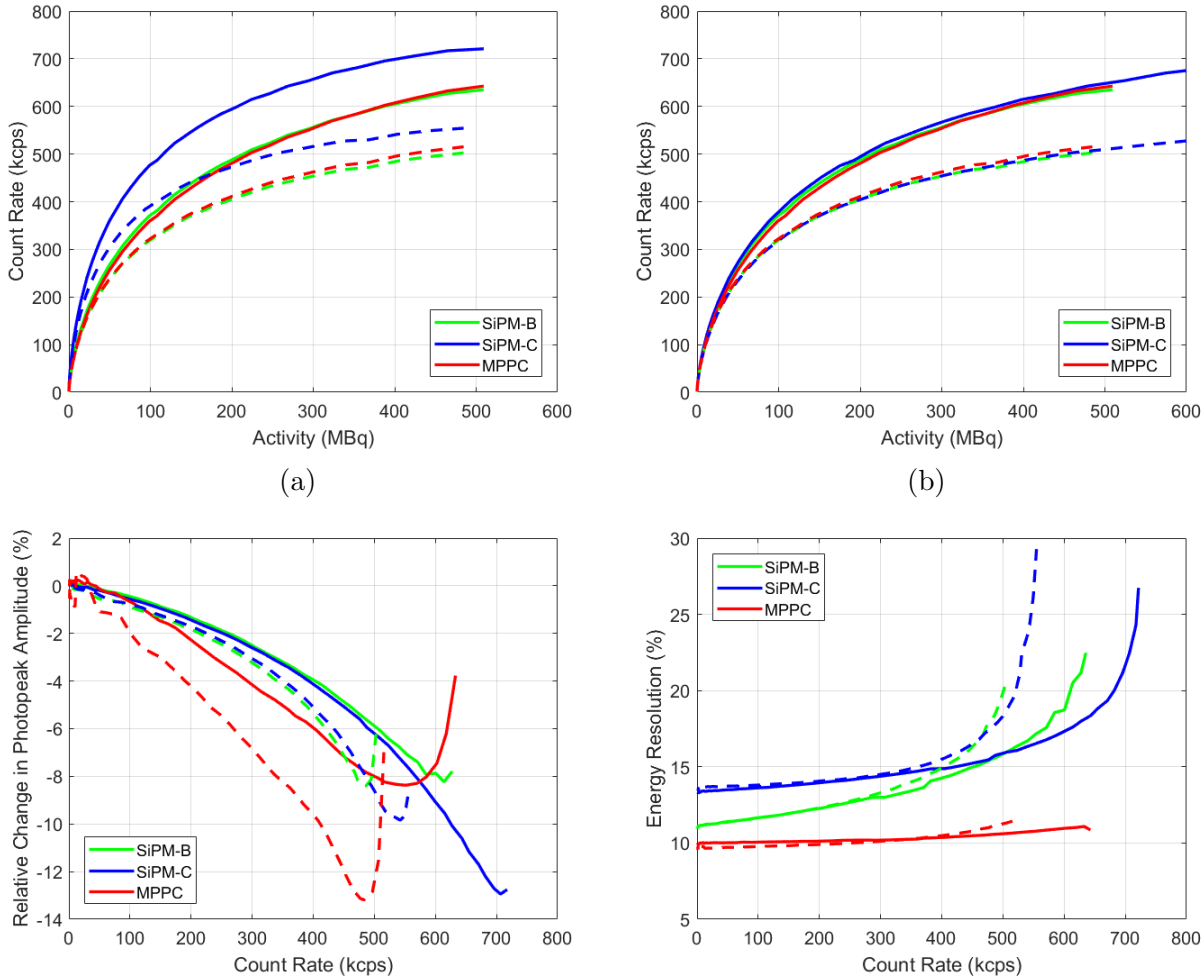

(a) (b) (c) (d)

Figure 6.3.4: Decaying source count rate measurement results for 22 s/e (solid lines) and 32 s/e (dashed lines) ADC capture. (a) Count rate vs [^{18}F]-FDG activity, (b) Count rate vs [^{18}F]-FDG activity with SiPM-C activity scaled by a factor of 16/9, (c) photopeak amplitude vs count rate, and (d) energy resolution vs count rate.

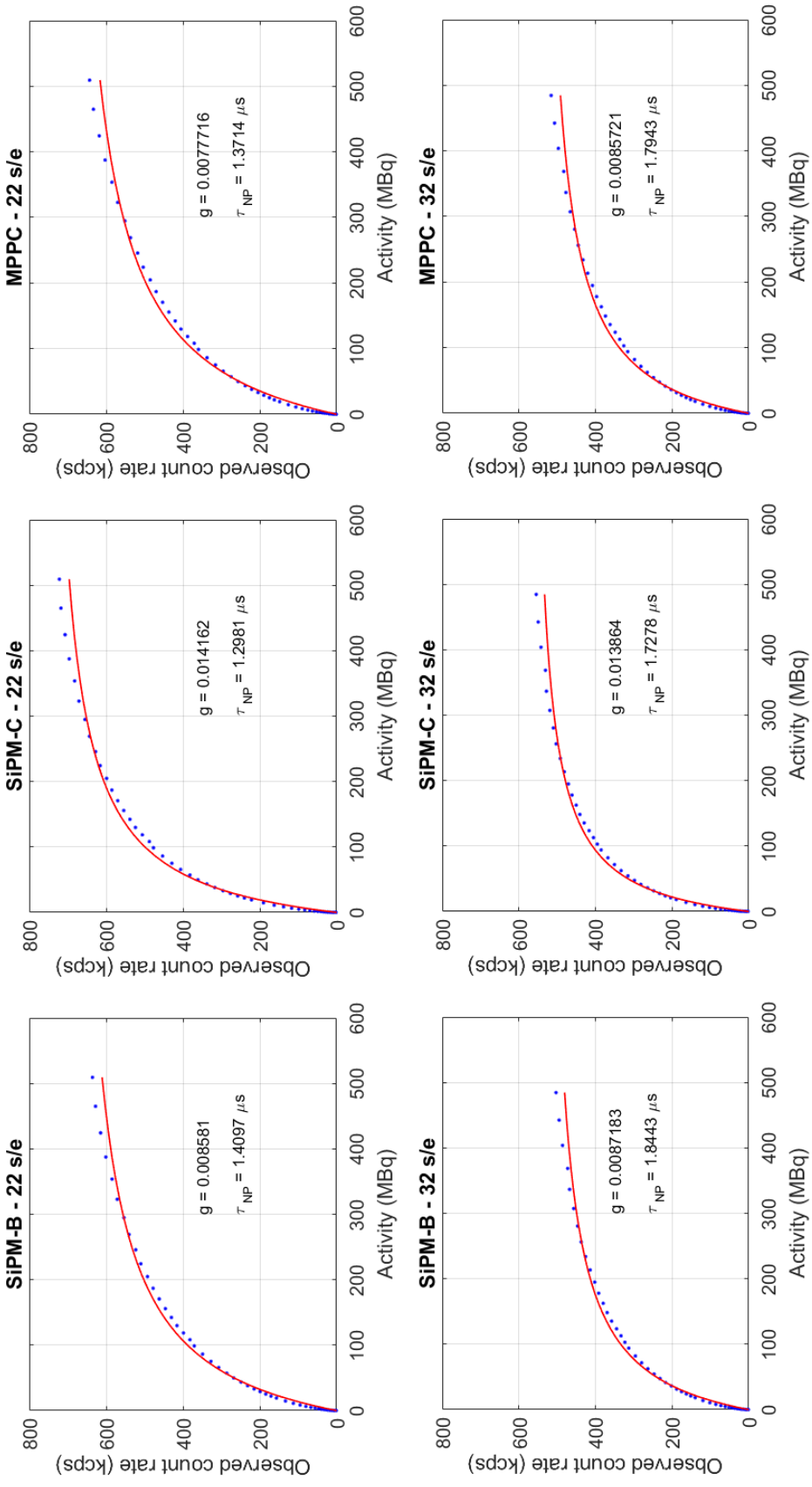

Figure 6.3.5: Non-paralyzable dead time models fit to the SiPM-B (left), SiPM-C (centre), and MPPC (right) count rate curves. In general, the non-paralyzable dead time was 1.3 - 1.4 μs and 1.7 - 1.8 μs for 22 s/e (top row) and 32 s/e ADC capture (bottom row), respectively.

(a) SiPM-B (b) SiPM-C (c) MPPC

Figure 6.3.6: Flood histograms from the decaying source measurements for (a) SiPM-B, (b) SiPM-C, and (c) MPPC arrays. For each subfigure, the left column images were generated using 22 s/e and the right column images were generated using 32 s/e. Flood histograms shown are acquisitions with detector count rates of ∼500 kcps, ∼300 kcps, and ∼25 kcps. Only one of the two 4×4 detector arrays are shown for each flood image. Energy histograms of crystals circled in blue are generated in Figure 6.3.7.

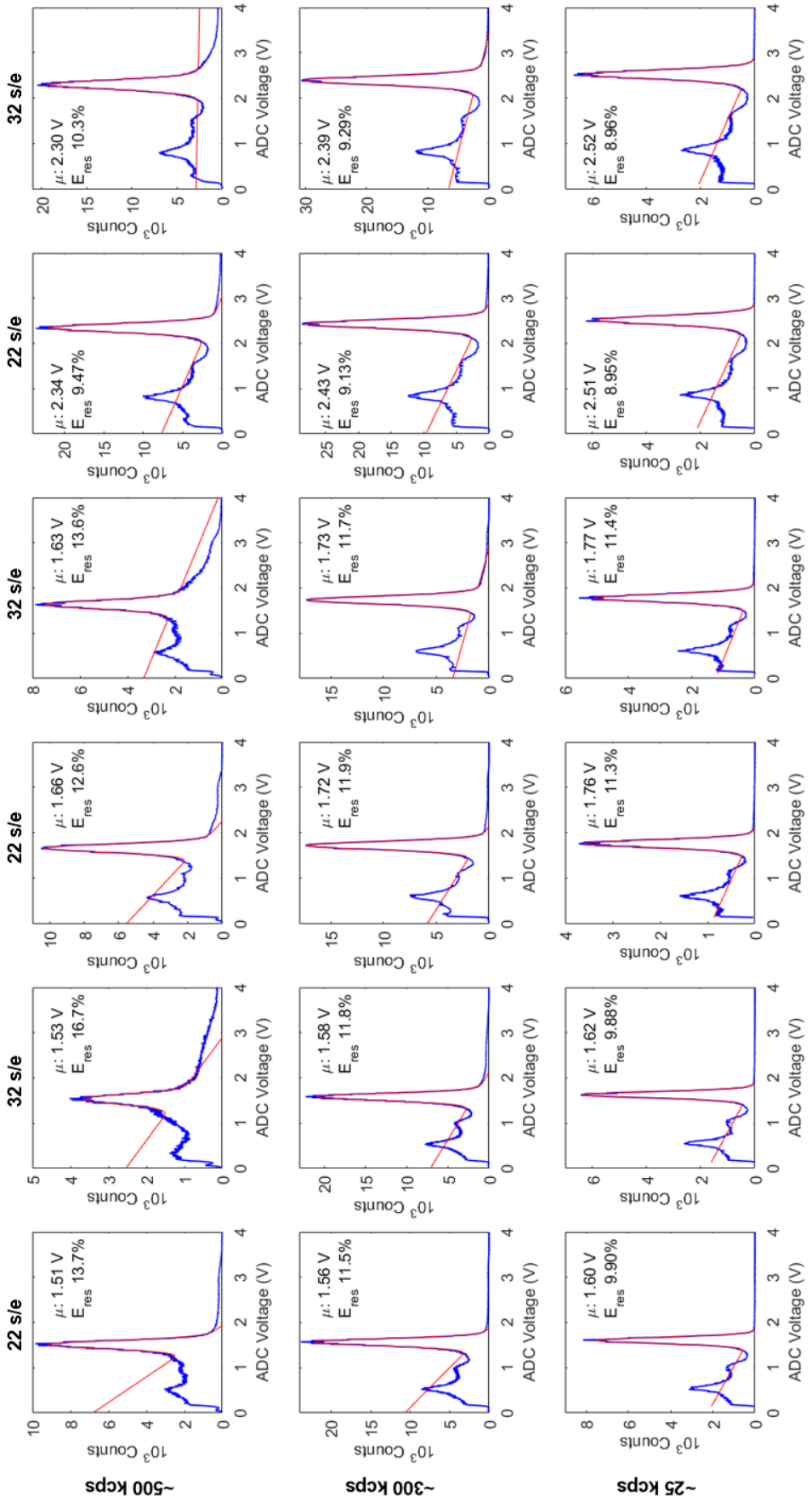

(a) SiPM-B (b) SiPM-C (c) MPPC

Figure 6.3.7: Energy histograms of the crystals circled in Figure 6.3.6. For each subfigure (a) SiPM-B, (b), SiPM-C, and (c) MPPC, the left column corresponds to 22 s/e and the right column corresponds to 32 s/e ADC capture. Each histogram is fit with a Gaussian-plus-line fit (red lines). Photopeak amplitude (μ) and energy resolution (E_{res}) are given on each plot.

SiPM-B and SiPM-C detectors, especially for 32 s/e ADC capture. At ∼300 kcps, moderate pileup effects are observed for SiPM-B while no pileup is observed for SiPM-C. There are no signs of pileup for any of the MPPC flood images at ∼500 kcps.

Energy histograms of the crystals circled in blue are generated in Figure 6.3.7. Pileup events manifest as 'tails' of events to the right of the photopeak. The most severe pileup occurs for 32 s/e SiPM-B and SiPM-C arrays at ∼500 kcps. In general, pileup tails were larger for 32 s/e ADC capture than 22 s/e ADC capture for all detectors at both ∼300 kcps and ∼500 kcps. No pileup tails are observed at ∼25 kcps.

6.3.5 Discussion

Given the same detector setup, higher count rates were reached when using 22 s/e ADC capture versus the default setting of 32 s/e ADC capture. This is strictly an improvement in the non-paralyzable component of the system dead time. Consider the flood histograms in Figure 6.3.6. The 22 s/e and 32 s/e SiPM-B flood histograms at ∼500 kcps look very different from each other, as well as SiPM-C. For both detectors, there is significantly more pileup when using 32 s/e ADC capture, despite having the same measured count rate as the 22 s/e ADC capture. Both setups are experiencing approximately the same source activity and ideally the same signal pileup. However, it takes ∼250 ns longer to process events with 32 s/e than 22 s/e, and therefore it is more probable that a second event occurs while the first is still being processed. This is further demonstrated in the energy histograms generated in Figure 6.3.4d, where pileup tails are more prominent for 32 s/e ADC capture.

Several differences in detector performance were observed as well. The SiPM-C arrays achieved a higher count rate than both the SiPM-B and MPPC arrays. This was expected because the the scintillator volume was larger for the SiPM-C arrays since they were coupled to 4×4 LYSO:Ce arrays. The SiPM-B and MPPC arrays were coupled with the same

scintillators, and therefore they achieved nearly the same count rates. When scaling the SiPM-C count rate curves to account for the larger scintillator arrays (Figure 6.3.4b), the 22 s/e and 32 s/e ADC sample curves are very similar for all three detectors. This implies that the current limiting factor in detector count rate is the acquisition system rather than the detector modules themselves. The data fit a non-paralyzable model reasonably well as shown in Figure 6.3.5. Reducing the sampling number from 32 to 22 reduced the system dead time by ∼400 ns for all three detectors.

In general, photopeak amplitude decreased as count rate increased. This can also be explained as a pileup effect. Recall in Section 6.2.4 that the standard output has signal undershoot. At high count rates, the undershoot of a previous event overlaps with the peak of the next event which reduces the signal amplitude. At very high count rates (∼400 kcps and above), pileup of the microcell discharge portion of the output signal became more prevalent which caused the photopeak amplitude to rise for all detectors. Interestingly, this photopeak amplitude rise was more drastic for MPPC than the SiPM-B and SiPM-C arrays, despite the fact that the MPPC energy resolution was much more stable than the other detectors.

Count rate curve fitting with a paralyzable and non-paralyzable model was attempted, however no good fit was achieved. The real dead time model of this system is likely a complex combination of the two models. The prevalence of both paralyzable and non-paralyzable dead time components have been demonstrated and discussed, and therefore neither model on their own adequately describes the nature of the system dead time.

There were considerable differences in pileup effects between detectors when observing flood histograms. There were no significant pileup effects observed for the MPPC array flood histograms, while the SiPM-B and SiPM-C flood histograms showed significant crystal smearing at high count rates. Differences in energy resolution stability can also be explained by differences in crystal separation between detector flood images. There was much greater

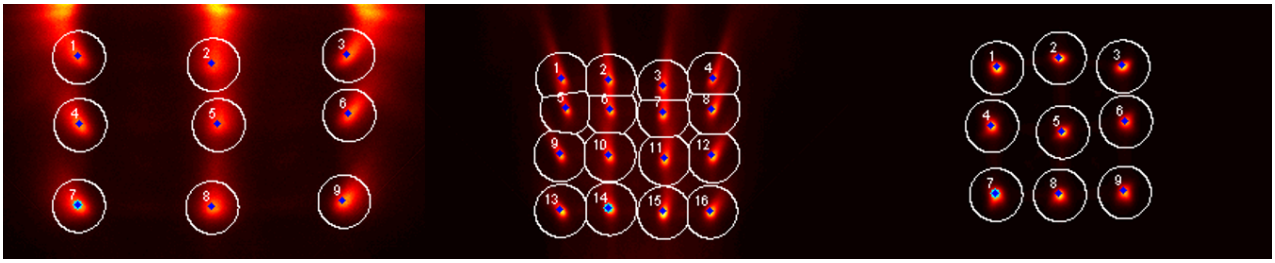

(a) (b) (c)

Figure 6.3.8: Segmented flood histograms from Set 1 Run 8 from the 22 s/e decaying source count rate measurements. The [^{18}F]-FDG source activity was ~269 MBq at the start of this acquisition. Significant pileup effects are observed for the (a) SiPM-B and (b) SiPM-C flood histograms, and consequently the pileup tails from some crystals penetrate the CLUT borders of neighbouring crystals. Little pileup effects are seen in the (c) MPPC array flood histograms. Count rates of these acquisitions were 540 kcps, 643 kcps, and 536 kcps for SiPM-B, SiPM-C, and MPPC, respectively.

separation between SiPM-B crystals than SiPM-C and MPPC crystals, although the SiPM-B crystals were larger. Difference in crystal size and separation is likely due to the difference in detector readout board multiplexing circuits. Crystal segmentation became problematic at high count rates for detectors with significant pileup. Figure 6.3.8 showed the segmented crystals of flood histograms of Set 1 Run 8 of the 22 s/e measurement. Since little/no pileup was observed for the MPPC flood histogram, crystals were clearly separated. However, crystal pileup 'smears' often penetrated neighbouring borders for the SiPM-B and SiPM-C flood images. Smeared events that cross segmented borders are binned in the wrong crystal when generating energy histograms. Since there tends to be inter-crystal differences in performance such as gain, segmentation errors cause photopeak broadening.

6.3.6 Conclusion

The decaying source count rate results clearly demonstrate a reduction in system dead time. The paralyzable component was reduced by using the enhanced detector readout board along with detectors with reduced time constants, leading to improved flood histograms and energy resolution stability towards high count rates for MPPCs. Additionally, the non-paralyzable component was reduced by ~400 ns by decreasing the signal sampling number

of the OpenPET acquisition firmware from 32 s/e to 22 s/e ADC capture.

Chapter 7

Conclusion

In conclusion, the timing and count rate performance of several PET insert detector modules has been characterized and optimized. Improvements in coincidence time resolution and signal duration were made through enhancements of the resistor-based charge division multiplexing circuit of the detector readout board. In fact, CTR was similar for SensL's C-series and J-series SiPM arrays (using their decoupled fast outputs) and Hamamatsu's MPPC arrays when using the second-generation detector readout board, all of which were improved over the CTR of the SensL B-series SiPMs with the first-generation detector readout board. Signal duration improved when using photodetectors with a lower time constant. The count rate performance of the detector module and acquisition system was optimized by changing the waveform sampling number of the OpenPET system from 32 samples/event to 22 samples/event.

Implementation of the second-generation readout board is not so simple, however. The board itself is much larger than the first-generation design. Size modifications are required before it can be used in a ring geometry made to fit within the bore of the 7T Bruker 70/20 MRI system. Additionally, modifications to the photodetectors and second-generation readout board are required in order to accommodate the DLO scintillator array footprint

used by the first-generation design.

The PET insert uses the OpenPET system for full-system data acquisition. Firmware updates to the OpenPET system are required if TOF-PET using SensL's C-Series or J-Series SiPM fast outputs is to be realized. The MPPC readout does not have fast outputs, and therefore the OpenPET system could support TOF-PET using MPPC standard outputs. However, the second-generation readout board must be modified to support MPPC readout (i.e. output pin rerouting and replacement of 50V-rated capacitors). Another complication with MPPC readout is bias voltage. The current PET insert uses SiPM-B arrays biased at 27.0 V, while a second-generation PET insert with MPPC readout would have considerably higher power consumption since MPPCs require >50 V bias.

The work done in this thesis suggests that a PET insert utilizing MPPC arrays read out with the second-generation detector readout boards would have ∼570 ps coincidence time resolution and ∼350 ns signal duration. The paralyzable dead time would be decreased due to the reduction of signal duration compared to the first-generation PET insert. Finally, the non-paralyzable dead time would be reduced by ∼250 ns when using the OpenPET acquisition system with 22 samples/event ADC capture.

Bibliography

[1] T. Sekine, G. Delso, K. G. Zeimpekis, F. de Galiza Barbosa, E. E.G.W. Ter Voert, M. Huellner, and P. Veit-Haibach. Reduction of F-FDG dose in clinical PET/MR imaging by using silicon photomultiplier detectors. *Radiology*, 286(1):249–259, 2018.

[2] G. Bonanno, D. Marano, G. Romeo, S. Garozzo, A. Grillo, M.C. Timpanaro, O. Catalano, S. Giarrusso, D. Impiombato, G. La Rosa, and G. Sottile. Advances in Multi-Pixel Photon Counter technology: First characterization results. *Nuclear Instruments and Methods in Physics Research, Section A: Accelerators, Spectrometers, Detectors and Associated Equipment*, 806:383–394, 2016.

[3] M. Grodzicka-Kobylka, T. Szczesniak, and M. Moszyski. Comparison of SensL and Hamamatsu 44 channel SiPM arrays in gamma spectrometry with scintillators. *Nuclear Instruments and Methods in Physics Research, Section A: Accelerators, Spectrometers, Detectors and Associated Equipment*, 856:53–64, 2017.

[4] B. Dolgoshein, R. Mirzoyan, E. Popova, P. Buzhan, A. Ilyin, V. Kaplin, A. Stifutkin, M. Teshima, and A. Zhukov. Large area UV SiPMs with extremely low cross-talk. *Nuclear Instruments and Methods in Physics Research, Section A: Accelerators, Spectrometers, Detectors and Associated Equipment*, 695:40–43, 2012.

[5] C. Jendrysik, L. Andriek, G. Liemann, H.G. Moser, J. Ninkovi, R. Richter, and F. Schopper. Characterization of the first prototypes of silicon photomultipliers with bulk-integrated quench resistor fabricated at MPI semiconductor laboratory. *Nuclear*

Instruments and Methods in Physics Research, Section A: Accelerators, Spectrometers, Detectors and Associated Equipment, 718:262–265, 2013.

[6] K. Doroud, M.C.S. Williams, and K. Yamamoto. The Strip Silicon Photo-Multiplier: An innovation for enhanced time and position measurement. *Nuclear Instruments and Methods in Physics Research, Section A: Accelerators, Spectrometers, Detectors and Associated Equipment*, 853:1–8, 2017.

[7] J. Du, X. Bai, A. Gola, F. Acerbi, A. Ferri, C. Piemonte, Y. Yang, and S. R. Cherry. Performance of a high-resolution depth-encoding PET detector module using linearly-graded SiPM arrays. *Physics in Medicine and Biology*, 63(3):035035, 2018. doi: 10.1088/1361-6560/aaa707.

[8] E. C. Ehman, G. B. Johnson, J. E. VillanuevaMeyer, S. Cha, A. P. Leynes, P. E.Z. Larson, and T. A. Hope. PET/MRI: Where might it replace PET/CT? *Journal of Magnetic Resonance Imaging*, 46(5):1247–1262, 2017.

[9] R. Raylman, A. Stolin, B. Hou, and P. Ledden. Evaluation of an SiPM-based PET/MRI insert. *Journal Of Nuclear Medicine*, 56(3), 2015.

[10] D. Schug, J. Wehner, P. M. Dueppenbecker, B. Weissler, P. Gebhardt, B. Goldschmidt, A. Salomon, F. Kiessling, and V. Schulz. PET performance and MRI compatibility evaluation of a digital, ToF-capable PET/MRI insert equipped with clinical scintillators. *Physics in Medicine and Biology*, 60(18):7045–7067, 2015.

[11] N. Omidvari, J. Cabello, G. Topping, F. R. Schneider, S. Paul, M. Schwaiger, and S. I. Ziegler. PET performance evaluation of MADPET4: A small animal PET insert for a 7 T MRI scanner. *Physics in Medicine and Biology*, 62(22):8671–8692, 2017.

[12] G. Stortz, J. D. Thiessen, D. Bishop, M. S. Khan, P. Kozlowski, F. Retire, G. Schellenberg, E. Shams, X. Zhang, C. J. Thompson, A. L. Goertzen, and V. Sossi. Performance

of a PET Insert for High-Resolution Small-Animal PET/MRI at 7 Tesla. *Journal Of Nuclear Medicine*, 59(3), 2018.

[13] C. J. Thompson, A. L. Goertzen, J. Thiessen, D. Bishop, G. Stortz, P. Kozlowski, F. Retière, X. Zhang, and V. Sossi. Development of a PET scanner for simultaneously imaging small animals with MRI and PET. *Sensors*, 14(8):14654–14671, 2014.

[14] G. Stortz, M. D. Walker, C. J. Thompson, A. L. Goertzen, F. Retiere, X. Zhang, J. D. Thiessen, P. Kozlowski, and V. Sossi. Characterization of a new MR compatible small animal PET scanner using Monte-Carlo simulations. *IEEE Transactions on Nuclear Science*, 60(3):1637–1644, 2013.

[15] F. H. Attix. *Introduction to Radiological Physics and Radiation Dosimetry*. New York: John Wiley & Sons, Inc, 1986.

[16] M. Partridge, A. Spinelli, W. Ryder, and C. Hindorf. The effect of $\beta+$ energy on performance of a small animal PET camera. *Nuclear Instruments and Methods in Physics Research, Section A: Accelerators, Spectrometers, Detectors and Associated Equipment*, 568(2):933–936, 2006.

[17] W. W. Moses. Fundamental limits of spatial resolution in PET. *Nuclear Instruments and Methods in Physics Research, Section A: Accelerators, Spectrometers, Detectors and Associated Equipment*, 648(S1):S236–S240, 2011.

[18] NIST. XCOM: Photon Cross Sections Database, 2018. URL https://physics.nist.gov/PhysRefData/Xcom/html/xcom1.html. [Online; accessed 09-February-2018].

[19] C. Wanarak, W. Chewpraditkul, and A. Phunpueok. Light yield non-proportionality and energy resolution of $Lu_{1.95}Y_{0.05}SiO_5$:Ce and Lu_2SiO_5:Ce scintillation crystals. *Procedia Engineering*, 32:765–771, 2012.

[20] A. M.L. MacLeod, P. J. Boyle, D. S. Hanna, P. R.B. Saull, L. E. Sinclair, and H. C.J. Seywerd. Development of a Compton imager based on bars of scintillator. *Nuclear*

Instruments and Methods in Physics Research, Section A: Accelerators, Spectrometers, Detectors and Associated Equipment, 767:397–406, 2014.

[21] M. Kuramoto, T. Nakamori, S. Kimura, S. Gunji, M. Takakura, and J. Kataoka. Development of TOF-PET using Compton scattering by plastic scintillators. *Nuclear Instruments and Methods in Physics Research, Section A: Accelerators, Spectrometers, Detectors and Associated Equipment*, 845:668–672, 2017.

[22] A. Kishimoto, J. Kataoka, A. Koide, K. Sueoka, Y. Iwamoto, T. Taya, and S. Ohsuka. Development of a compact scintillator-based high-resolution Compton camera for molecular imaging. *Nuclear Instruments and Methods in Physics Research, Section A: Accelerators, Spectrometers, Detectors and Associated Equipment*, 845:656 – 659, 2017. Proceedings of the Vienna Conference on Instrumentation 2016.

[23] W. R. Leo. *Techniques for Nuclear and Particle Physics Experiments: A How-To Approach*. Berlin; New York: Springer, 2nd edition, 1994.

[24] S. David, M. Georgiou, E. Fysikopoulos, and G. Loudos. Evaluation of a SiPM array coupled to a $Gd_3Al_2Ga_3O_{12}$:Ce (GAGG:Ce) discrete scintillator. *Physica Medica*, 31 (7):763–766, 2015.

[25] G. F. Knoll. *Radiation Detection and Measurement*. New York: Wiley, 4th edition, 2010.

[26] T. Kato, J. Kataoka, T. Nakamori, T. Miura, H. Matsuda, K. Sato, Y. Ishikawa, K. Yamamura, N. Kawabata, H. Ikeda, G. Sato, and K. Kamada. Development of a large-area monolithic 44 MPPC array for a future PET scanner employing pixelized Ce:LYSO and Pr:LuAG crystals. *Nuclear Instruments and Methods in Physics Research, Section A: Accelerators, Spectrometers, Detectors and Associated Equipment*, 638(1):83–91, 2011.

[27] Saint-Gobein. Physical Properties of Common Inorganic Scintillators, 2017.

URL https://www.crystals.saint-gobain.com/sites/imdf.crystals.com/files/documents/physical-properties-of-inorganic-scintillators_0.pdf. [Online; accessed 04-April-2018].

[28] K. Kamada, Y. Shoji, V. V. Kochurikhin, S. Okumura, S. Yamamoto, A. Nagura, J. Y. Yeom, S. Kurosawa, Y. Yokota, Y. Ohashi, M. Nikl, and A. Yoshikawa. Growth and scintillation properties of 3 in. diameter Ce doped $Gd_3Ga_3Al_2O_{12}$ scintillation single crystal. *Journal of Crystal Growth*, 452:81–84, 2016.

[29] G. Jellison, E. Specht, L. Boatner, D. Singh, and C. Melcher. Spectroscopic refractive indices of monoclinic single crystal and ceramic lutetium oxyorthosilicate from 200 to 850 nm. *Journal Of Applied Physics*, 112(6), 2012. doi: 10.1063/1.4752421.

[30] M. Kobayashi, S. Aogaki, F. Takeutchi, Y. Tamagawa, and Y. Usuki. Performance of thin long scintillator strips of GSO:Ce, LGSO:Ce and LuAG:Pr for low energy γ-rays. *Nuclear Instruments and Methods in Physics Research, Section A: Accelerators, Spectrometers, Detectors and Associated Equipment*, 693:226–235, 2012.

[31] J. Du, Y. Yang, X. Bai, M. S. Judenhofer, E. Berg, K. Di, S. Buckley, C. Jackson, and S. R. Cherry. Characterization of large-area SiPM array for PET applications. *IEEE Transactions on Nuclear Science*, 63(1):8–16, 2016.

[32] J. P. Schmall, R. I. Wiener, S. Surti, A. Ferri, A. Gola, A. Tarolli, C. Piemonte, and J. S. Karp. Timing and energy resolution of new near-UV SiPMs coupled to $LaBr_3$:Ce for TOF-PET. *IEEE Transactions on Nuclear Science*, 61(5):2426–2432, 2014.

[33] SensL. C-series: Low noise, fast, blue-sensitive silicon photomultipliers, 2014. URL http://sensl.com/downloads/ds/UM-MicroC.pdf. [Online; accessed 29-March-2018].

[34] A. Del Guerra, N. Belcari, and M. Bisogni. Positron emission tomography: Its' 65 years. *Rivista del Nuovo Cimento*, 39(4):155–223, 2016.

[35] J. S. Karp, S. Surti, M. E. Daube-Witherspoon, and G. Muehllehner. Benefit of time-

of-flight in PET: Experimental and clinical results. *Journal of Nuclear Medicine*, 49(3): 462–470, 2008.

[36] T. Tomitani. Image reconstruction and noise evaluation in photon time-of-flight assisted positron emission tomography. *IEEE Transactions on Nuclear Science*, 28(6):4581–4589, 1981.

[37] A. L. Goertzen, G. Stortz, J. D. Thiessen, D. Bishop, M. S. Khan, P. Kozlowski, F. Retiere, G. Schellenberg, E. Shams, V. Sossi, and C. J. Thompson. First results from a high-resolution small animal SiPM PET insert for PET/MR imaging at 7T. *IEEE Transactions on Nuclear Science*, 63(5):2424–2433, 2016.

[38] A. L. Goertzen, X. Zhang, M. M. McClarty, E. J. Berg, C. Y. Liu, P. Kozlowski, F. Retiere, L. Ryner, V. Sossi, G. Stortz, and C. J. Thompson. Design and performance of a resistor multiplexing readout circuit for a SiPM detector. *IEEE Transactions on Nuclear Science*, 60(3):1541–1549, 2013.

[39] Stefan R.: Paul Scherrer Institut. DRS4 Evaluation Board User's Manual, 2016. URL https://www.psi.ch/drs/DocumentationEN/manual_rev50.pdf. [Online; accessed 09-May-2018].

[40] A. L. Goertzen, R. Shrestha, M. S. Khan, G. Stortz, D. Bishop, P. Kozlowski, F. Retiere, J. D. Thiessen, C. J. Thompson, and V. Sossi. Data acquisition for a preclinical MR compatible PET insert using the OpenPET platform. *IEEE Transactions on Radiation and Plasma Medical Sciences*, 1(6):495–504, 2017.

[41] W. S. Choong, F. Abu-Nimeh, W. W. Moses, Q. Peng, C. Q. Vu, and J. Y. Wu. A front-end readout Detector Board for the OpenPET electronics system. *Journal Of Instrumentation*, 10(8), 2015. doi: 10.1088/1748-0221/10/08/T08002.

[42] Y. Wu, C. Catana, R. Farrell, P. A. Dokhale, K. S. Shah, J. Qi, and S. R. Cherry.

PET performance evaluation of an MR-compatible PET insert. *IEEE Transactions on Nuclear Science*, 56(3), 2009.

[43] SensL. Introduction to SiPM, 2017. URL https://www.sensl.com/downloads/ds/TN%20-%20Intro%20to%20SPM%20Tech.pdf. [Online; accessed 29-March-2018].

[44] C. Moisan, J. G. Rogers, and J .L. Douglas. A count rate model for PET and its application to an LSO HR PLUS scanner. 44(3):1219–1224, 1997.

[45] J. Y. Yeom, R. Vinke, and C. S. Levin. Optimizing timing performance of silicon photomultiplier-based scintillation detectors. *Physics in Medicine and Biology*, 58(4): 1207–1220, 2013. doi: 10.1088/0031-9155/58/4/1207.

[46] M. Pizzichemi, G. Stringhini, T. Niknejad, Z. Liu, P. Lecoq, S. Tavernier, J. Varela, M. Paganoni, and E. Auffray. A new method for depth of interaction determination in PET detectors. *Physics in Medicine and Biology*, 61(12):4679–4698, 2016.

[47] H. Park, G. B. Ko, and J. S. Lee. Hybrid charge division multiplexing method for silicon photomultiplier based PET detectors. *Physics in Medicine and Biology*, 62(11): 4390–4405, 2017.

[48] M. V. Nemallapudi, S. Gundacker, P. Lecoq, E. Auffray, A. Ferri, A. Gola, and C. Piemonte. Sub-100 ps coincidence time resolution for positron emission tomography with LSO:Ce codoped with Ca. *Physics in Medicine and Biology*, 60(12):4635–4649, 2015.

[49] J. P. Schmall, S. Surti, and J. S. Karp. Characterization of stacked-crystal PET detector designs for measurement of both TOF and DOI. *Physics in Medicine and Biology*, 60 (9):3549–3565, 2015.

[50] A. Ferri, F. Acerbi, A. Gola, G. Paternoster, C. Piemonte, and N. Zorzi. Performance of FBK low-afterpulse NUV silicon photomultipliers for PET application. *Journal of Instrumentation*, 11(3):P03023–P03023, 2016. doi: 10.1088/1748-0221/11/03/P03023.

[51] S. Gundacker, E. Auffray, K. Pauwels, and P. Lecoq. Measurement of intrinsic rise times for various L(Y)SO and LuAG scintillators with a general study of prompt photons to achieve 10 ps in TOF-PET. *Physics in Medicine and Biology*, 61(7):2802–2837, 2016.

[52] M. Morrocchi, W. C.J. Hunter, A. Del Guerra, T. K. Lewellen, P. E. Kinahan, L. R. MacDonald, M. G. Bisogni, and R. S. Miyaoka. Evaluation of event position reconstruction in monolithic crystals that are optically coupled. *Physics in Medicine and Biology*, 61(23):8298–8320, 2016.

[53] F. R. Schneider, K. Shimazoe, I. Somlai-Schweiger, and S. I. Zeigler. A PET detector prototype based on digital SiPMs and GAGG scintillators. *Physics in Medicine and Biology*, 60(4):1667–1679, 2015.

[54] Z. Liu, M. Pizzichemi, E. Auffray, P. Lecoq, and M. Paganoni. Performance study of Philips digital silicon photomultiplier coupled to scintillating crystals. *Journal of Instrumentation*, 11(1):P01017–P01017, 2016. doi: 10.1088/1748-0221/11/01/P01017.

[55] N. Omidvari, R. Sharma, T.R. Ganka, F.R. Schneider, S. Paul, and S.I. Ziegler. Characterization of 1.2×1.2 mm^2 silicon photomultipliers with Ce:LYSO, Ce:GAGG, and Pr:LuAG scintillation crystals as detector modules for positron emission tomography. *Journal of Instrumentation*, 12(4):P04012–P04012, 2017. doi: 10.1088/1748-0221/12/04/P04012.

[56] A. J. González, A. Peiró, P. Conde, L. Hernández, L. Moliner, A. Orero, M. J. Rodríguez-Álvarez, F. Sánchez, A. Soriano, L. F. Vidal, and J. M. Benlloch. Monolithic crystals for PET devices: Optical coupling optimization. *Nuclear Instruments and Methods in Physics Research, Section A: Accelerators, Spectrometers, Detectors and Associated Equipment*, 731:288–294, 2013.

[57] J. W. Cates and C. S. Levin. Advances in coincidence time resolution for PET. *Physics in Medicine and Biology*, 61(6):2255–2264, 2016.